Spectrally resolved optical study of transient spin dynamics in semiconductors

by

Zhigang Chen

B.S., Nanjing University, 1998

M.S., University of Colorado, 2005

A thesis submitted to the

Faculty of the Graduate School of the

University of Colorado in partial fulfillment

of the requirements for the degree of

Doctor of Philosophy

Department of Physics

2006

This thesis entitled:
Spectrally resolved optical study of transient spin dynamics in semiconductors
written by Zhigang Chen
has been approved for the Department of Physics

Prof. Steven T. Cundiff

Prof. Daniel S. Dessau

Date

The final copy of this thesis has been examined by the signatories, and we find that both the content and the form meet acceptable presentation standards of scholarly work in the above mentioned discipline.

Chen, Zhigang (Ph.D., Physics)

Spectrally resolved optical study of transient spin dynamics in semiconductors

Thesis directed by Prof. Steven T. Cundiff

Using the spin of the electron to carry information, instead of or in addition to its charge, could provide advances in the capabilities of microelectronics. Successful implementation of spin-based electronics requires preservation of the electron spin coherence. Long spin coherence times have been observed in lightly n-doped semiconductors, with a maximum at a “magic” electron density. We systematically study the spin dynamics of the electron in a GaAs quantum well, where the electron density in the well can be varied through optical excitation. We show that spin coherence is lost due to the interplay between localization by disorder and dynamical scattering. The disorder potential is characterized by measuring the electron Landé g factor dependence on density. Our results show that the longest spin coherence is obtained for weakly localized spins, which may dictate a compromise in the design of devices between increasing the spin coherence time and improving transport properties.

We also explore the intimate connection between electron spin and optical excitation that initiates and controls the spin states. We study the interplay of spin dynamics between excitons, negatively charged excitons and the two-dimensional electron gas in a lightly n-doped semiconductor quantum well. The spin of the electron gas can be polarized through interband transitions, and the electron spin can persist long after the recombination of optically excited carriers. We find that the excitation of spin polarization of the resident electrons depends on the recombination times and spin relaxation times of the optically excited carriers and the energy chosen for the light pulses.

Dedication

To my wife, Yingqi.

Acknowledgements

First, I would like to thank my advisor, Professor Steve Cundiff. I am grateful for his constant support and encouragement throughout my graduate career. His enthusiasm for research has been a great inspiration and his brilliant scientific insight has always helped me and kept me motivated. I especially thank him for giving me opportunities to try many exciting projects, and providing good advices whenever needed. I would also like to thank Professor Dan Dessau for his advices and encouragement, and other committee members, Professor Charles Rogers, Professor Victor Gurarie and Professor Rafael Piestun, for their support and helpful comments.

Finally, my thanks to my colleagues, family and friends for their support. I would like to thank my fellow Cundiff group members, past and present, for their friendship and aid. Sam Cater, who contributed so much to my graduate research, gave me countless ideas and advices. My wife, Yingqi, sacrificed so much to give me support throughout my career. Many thanks my friends, Wenjian Cai, Wengang Zheng and Ying-ju Wang for their great friendship.

Contents

Chapter

Appendix

Figures

Figure

Chapter 1

Introduction

1.1 A perspective on spintronics

Spintronics, or spin-based electronics, involves the study of active control and manipulation of spin degrees of freedom in solid-state systems [1, 2, 3]. Using the spin of the electron to carry information, instead of or in addition to its charge, could provide advances in the capabilities of microelectronics [4]. In a broad sense, there are already commercial spintronic devices. One example is the read heads for magnetic hard discs that use the giant magnetoresistance effect. Those devices normally consist of magnetic and non-magnetic metals rather than semiconductors, and are more appropriately described as magnetoelectronics [4, 5]. Traditional electronics, on the other hand, is dominated by semiconductors for obvious reasons. Combining the advantages of semiconductors with the concept of spins and thereby introducing spin into semiconductor devices is therefore a logical step and opens a new pathway for spintronics.

The current goal of spintronics is to understand the interaction between the particle spin and its solid-state (especially semiconductor) environments and to make useful devices using the acquired knowledge. Fundamental studies in spintronics include the generation of spin polarization, spin transport, spin dynamics and relaxation, and spin detection. We illustrate the above aspects by showing a prototypical spintronic device, a spin field-effect transistor [6], which is

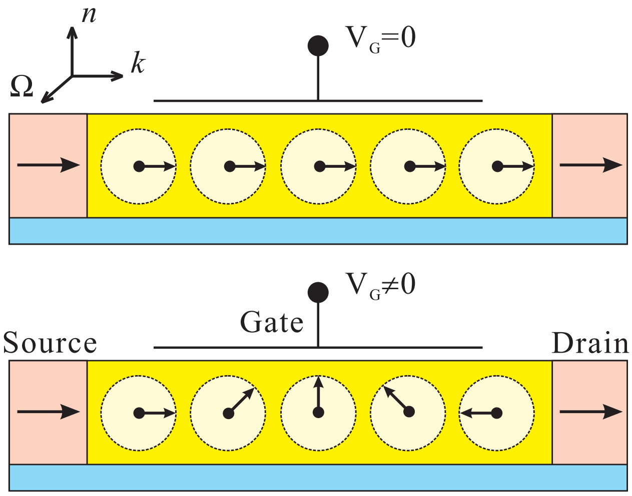

Figure 1.1: Scheme of a spin field-effect transistor. The current is controlled by the gate voltage, being large if the electron spin at the drain is parallel to its initial direction (top), and small if antiparallel (bottom).

depicted in Figure 1.1. The spin field-effect transistor consists of a source, a drain, a narrow channel, and a gate for controlling the current. The source and drain are ferromagnets acting as the injector and detector of electron spins. Specifically, the source injects electrons with spins parallel to the electron transport direction, and the drain detects electron spins near the drain after the electrons transport through the channel. An effective magnetic field (in the direction of Ω in Figure 1.1), arising from the spin-orbit coupling due to the confinement of the channel and the applied electrostatic potential of the gate [7], will cause electron spins to precess as the electrons travel through the channel. The magnitude of this effective magnetic field is tunable by the gate voltage. By modifying the gate voltage, we can have either parallel or antiparallel electron spins at the drain, and therefore effectively control the current. Key issues of the device include how long the electron can preserve its spin coherence as it propagate through the channel and how fast the electron spin will precess under the magnetic field.

A quantum-coherent approach to electronics offers the advantage of ultrafast device operation resulting from the interference between two coherently occupied quantum states. This requires the quantum coherence being able to evolve coherently long enough to be manipulated. In semiconductors, the optical coherence (the electric dipoles between the electron-hole pairs after optical pulse excitation) time is usually tens of picoseconds or less. The electron spin states, on the other hand, show a more robust resistance to the environmental sources of decoherence. Long spin coherence times exceeding hundreds of nanoseconds has been observed in lightly n-doped semiconductors [8, 9]. Spin coherence is also preserved for transport over distances exceeding 100 micrometers [10]. Spin therefore offers opportunities to store and manipulate phase coherence over length and time scales much larger than is typically possible in charge-based devices, and shows promise for constructing quantum bits in quantum information processing [11]. Time-resolved optical experiments have been proven to be a good candidate for generating, manipulating and detecting the spin coherence in semiconductor systems [12, 13]. Optical pulses are used to create a superposition of the basis spin states defined by an applied magnetic field, and follow the phase, amplitude and location of the resulting electronic spin precession (coherence). The work presented in this thesis will focus on the coherent optical generation and manipulation of electron spins.

1.2 General background

1.2.1 Spin coherence

The term “coherence” refers to a well-defined phase, or phase memory in a system. In a quantum system, the evolution of the wavefunction follows its Hamiltonian in a predictable way, which we call the quantum-coherent evolution of the state. Consider an electron spin in a basis defined by a transverse applied magnetic field (Voigt geometry), i.e. the electron is in a pure spin state initially whose direction is perpendicular to the magnetic field (Figure 1.2). The electron Hamiltonian under the magnetic field is

$$H = g\mu_B \mathbf{S} \cdot \mathbf{B}/\hbar = \omega_L S_z, \tag{1.1}$$

with $\omega_L \equiv g\mu_B B/\hbar$ the electron Larmor precession frequency. Here g is the electron Landé g factor, and μ_B is the Bohr magneton. The eigenstates in the system are $|S_z;+\rangle$ and $|S_z;-\rangle$, simply denoted as $|+\rangle$ and $|-\rangle$, which are split in the magnetic field by the Zeeman energy $\Delta E = g\mu_B B = \hbar\omega_L$. The initial electron spin wavefunction is in the $+x$ direction,

$$|\Psi(0)\rangle = |S_x;+\rangle = \frac{1}{\sqrt{2}}|+\rangle + \frac{1}{\sqrt{2}}|-\rangle. \tag{1.2}$$

It is a coherent superposition of the spin-up ($|+\rangle$) and spin-down ($|-\rangle$) eigenstates, defined by the applied magnetic field. The electron spin will evolve with time under the spin Hamiltonian, resulting in oscillation between the two spin eigenstates. Specifically, the electron spin wavefunction $|\Psi(t)\rangle$ at a later time t follows

$$|\Psi(t)\rangle = \exp(\frac{-iHt}{\hbar})|\Psi(0)\rangle = \frac{1}{\sqrt{2}}\exp(-\frac{i\omega_L t}{2})|+\rangle + \frac{1}{\sqrt{2}}\exp(\frac{i\omega_L t}{2})|-\rangle. \tag{1.3}$$

If the projection of electron spin in the x direction is measured, the measured quantity (averaged over an ensemble) is the expectation value:

$$\langle S_x(t)\rangle = \langle\Psi(t)|S_x|\Psi(t)\rangle = \frac{\hbar}{2}\cos(\omega_L t). \tag{1.4}$$

This is obtained by expressing the operator S_x in the z-basis,

$$S_x = \frac{\hbar}{2}\left[(|+\rangle\langle-|) + (|-\rangle\langle+|)\right]. \tag{1.5}$$

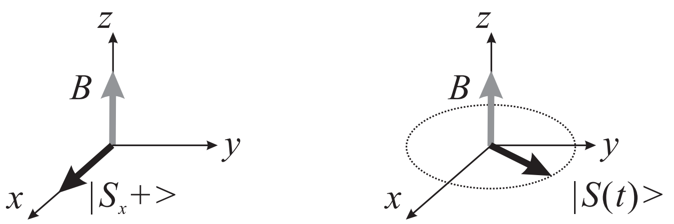

Figure 1.2: An initial spin vector in the $+x$ direction precesses under an applied magnetic field.

Classically, the oscillation in Equation 1.4 corresponds to Larmor precession of the spin vector at a frequency ω_L in a plane normal to the applied field, with the projection of the spin vector along its initial direction oscillating as a cosine.

An electron can lose its spin coherence through spin scattering off another type of spin, spin-orbit scattering off a lattice vibration or impurity, or particle annihilation through optical recombination with a hole. Spin decoherence can be represented by adding a phenomenological damping term in the Hamiltonian shown in Equation 1.1,

$$H = g\mu_B \mathbf{S}\cdot\mathbf{B}/\hbar - i\hbar\Gamma. \tag{1.6}$$

Equation 1.3 and 1.4 can then be rewritten as

$$|\Psi(t)\rangle = \exp(\frac{-iHt}{\hbar})|\Psi(0)\rangle = \frac{\exp(-\Gamma t)}{\sqrt{2}}\left[\exp(-\frac{i\omega_L t}{2})|+\rangle + \exp(\frac{i\omega_L t}{2})|-\rangle\right], \tag{1.7}$$

and

$$\langle S_x(t)\rangle = \langle\Psi(t)|S_x|\Psi(t)\rangle = \frac{\hbar}{2}\exp(-2\Gamma t)\cos(\omega_L t). \tag{1.8}$$

The characteristic time $1/2\Gamma$ is usually termed the transverse spin relaxation time, or spin coherence time, T_2. For an ensemble of electron spins, inhomogeneous factors such as variations in the electron g factor or in the local magnetic field can cause different spins to precess at slightly different frequencies. This will produce a spreading in the relative phase of spins within the electron distribution, even when all spins are evolving coherently. This additional decay of spin polarization due to inhomogeneities is termed spin dephasing, T_2^*. T_2^* gives the lower bound on T_2,

$$\frac{1}{T_2^*} \approx \frac{1}{T_2} + \frac{1}{T_{inh}}, \tag{1.9}$$

unless inhomogeneous effects can be eliminated.

1.2.2 Spin relaxation mechanisms

In this portion of the chapter, some of the most relevant spin relaxation mechanisms for conduction electrons in semiconductors are discussed. A detailed review of spin relaxation mechanisms in semiconductors and metals can be found in Reference [2].

1.2.2.1 Elliott-Yafet mechanism

In the Elliott-Yafet mechanism, the conduction electron spins relax through ordinary momentum scattering (spin-independent processes). In semiconductors, the electron wavefunction experiences spin-orbit coupling induced by the lattice ions, due to the spin-orbit Hamiltonian

$$H_{so} = \frac{\hbar}{4m^2c^2} \nabla V(\mathbf{r}) \times \hat{\mathbf{p}} \cdot \hat{\sigma}, \tag{1.10}$$

where $V(\mathbf{r})$ is the crystal potential, $\hat{\mathbf{p}}$ is the momentum operator and $\hat{\sigma}$ are the Pauli spin matrices. Due to the spin-orbit coupling, the energy eigenstates are no longer the spin eigenstates (Pauli spin-up $|\uparrow\rangle$ and spin-down $|\downarrow\rangle$ states), i.e. the spin magnetic quantum number m_s is no longer a good quantum number. Instead, the energy eigenstates are a mixture of $|\uparrow\rangle$ and $|\downarrow\rangle$ states, and are labeled as pseudospin eigenstates. The spin quantization axis for those pseudospin states varies with momentum $\mathbf{k}$. One of the consequences of this is that the spin quantum state of the electrons is not preserved for an elastic scattering event (even for spin-independent scattering). The spin decoherence can then be understood as an effective $\mathbf{k}$-dependent rotation of the pseudospin resulting from the momentum scattering. In the Elliott-Yafet mechanism, the spin relaxation time τ_s is proportional to momentum scattering time τ_p, meaning the more orbital scattering present in the material the more rapid the spin decoherence.

1.2.2.2 D'yakonov-Perel' mechanism

Another efficient spin relaxation mechanism for conduction electrons is the D'yakonov-Perel' mechanism, resulting from the spin-orbit coupling in systems lacking inversion symmetry. The zinc-blende semiconductors, such as GaAs and CdTe, are crystals without inversion symmetry. The inversion symmetry is also broken by the presence of asymmetric confining potentials in heterostructures, or by applying an electric field. In this category of crystals, even with the absence of an applied magnetic field, the pseudospin states are not degenerate. This spin splitting can be described by introducing an intrinsic $\mathbf{k}$-dependent effective magnetic field $\mathbf{B}(\mathbf{k})$, and $\boldsymbol{\Omega}(\mathbf{k}) = (e/m)\mathbf{B}(\mathbf{k})$ is the resulting Larmor precession vector. The spin-orbit coupling for conduction electrons now has the form

$$H_{so} = \frac{\hbar}{4m^2c^2}\nabla V(\mathbf{r}) \times \hat{\mathbf{p}} \cdot \hat{\sigma} = \hbar\boldsymbol{\Omega} \cdot \hat{\sigma}/2. \tag{1.11}$$

The presence of this $\mathbf{k}$-dependent internal magnetic field implies that spins of individual electrons will precess at different rate according to their momenta, and the ensemble electron spins will dephase inhomogeneously in momentum space.

Now consider the case when the momentum scattering time τ_p is shorter than the spin precession time due to internal magnetic fields ($\tau_p\Omega(\mathbf{k}) \leq 1$). Spins of individual electrons will precess about fluctuating magnetic fields, whose magnitude and direction change randomly. The faster the momentum scattering, the more random the electron spin precession and the slower the electron spin dephasing. This is the case for D'yakonov-Perel' mechanism, which is in the motional narrowing regime. The spin relaxation time τ_s is therefore inversely proportional to the momentum scattering time τ_p. The most important difference between the Elliott-Yafet and the D'yakonov-Perel' mechanisms is their opposite dependence on momentum scattering time τ_p.

1.2.2.3 Hyperfine interaction mechanism

The hyperfine interaction, which is the magnetic interaction between the magnetic moments of electrons and nuclei, provides an important mechanism for ensemble spin dephasing or single spin decoherence of localized electrons. The spatial variation in the nuclear spins, experienced by localized electrons via the hyperfine interaction, leads to electron spin dephasing. In the limit of small orbital and spin correlation between separated electron states and nuclear spin states, the spins of the ensemble electron dephase inhomogeneously. In a system where a strong orbital correlation (electron hopping) or spin correlation (electron-electron exchange interaction) between neighboring electron states is present, the inhomogeneous spin dephasing is motionally narrowed, as in the case of D'yakonov-Perel' mechanism. The spin dephasing due to the hyperfine interaction is shown to be important in low-dimensional semiconductors but rather weak in bulk semiconductors.

1.2.3 Electron Landé g factor

The electron Landé g factor is one of the basic parameters that describe the magnitude of the Zeeman splitting of electronic states in magnetic fields. The

Landé g factor for an atomic electron is given by

$$g_J = \frac{3}{2} + \frac{S(S+1) - L(L+1)}{2J(J+1)}, \tag{1.12}$$

with an energy splitting under a magnetic field $\mathbf{B}$

$$\Delta E = g_J \mu_B \mathbf{J} \cdot \mathbf{B}. \tag{1.13}$$

Here, J is the total electronic angular momentum, L is the orbital angular momentum, and S is the spin angular momentum. In the special case of free electrons ($L = 0$), $g \approx 2.0$.

An effective Landé g factor (g^*) is commonly used in solid state physics, with its definition shown in the Zeeman splitting $\Delta E = g^* \mu_B B$. g^* of conduction band electrons in semiconductors differs from the free electron value, 2.0, due to the spin-orbit interaction. Specifically, the g^* values at the conduction-band edge are smaller than the free-electron value, due to the spin-orbit interaction between the s-like (the lowest conduction band) and p-like (both the valence bands and the next higher conduction bands) states. The $k \cdot p$ perturbation theory predicts electronic properties such as the effective mass m^* and the Landé g factor g^* in the vicinity of a semiconductor band extremum. A five-band $k \cdot p$ model [14] was developed to calculate the g^*, where the spin-orbit interaction of the valence bands and higher conduction bands were taken into account:

$$g^* \approx g_0 \left[1 - \frac{E_P}{3} \left(\frac{1}{E} - \frac{1}{E + \Delta_0} \right) - \frac{E_P'}{3} \left(\frac{1}{E(\Gamma_7^c) - E} - \frac{1}{E(\Gamma_8^c) - E} \right) + C' \right]. \tag{1.14}$$

Here E is the electron energy measured from the valence band maximum, E_P, E_P', $E(\Gamma_7^c)$, $E(\Gamma_8^c)$ and Δ_0 are energy parameters of the bands. As shown in Equation 1.14, the g^* dependence on the energies of fundamental gaps in semiconductors is established.

1.3 Outline of thesis

This thesis is focused on optical studies of spin dynamics in semiconductor materials, especially that in quantum well systems. Chapter 2 gives an explanation of the optical techniques used to measure the spin dynamics of the carriers. Preliminary results on the spin dynamics in bulk GaAs samples are also presented. In Chapter 3 we present a spectral study of the spin dynamics in semiconductor quantum wells, where spin dependent nonlinearities of the materials are discussed. Chapter 4 explores the intimate connection between electron spin and optical excitation that initiates and controls the spin states. This involves studies of spin interplay between resident electrons and interband transitions. In Chapter 5 we systematically study the spin dynamics of the electron in a GaAs quantum well. The focus is on extending spin coherence time through optimum doping. We study the effects of disorder and dynamical scattering on electron spin decoherence. A conclusion is presented in Chapter 6. An appendix is included that discusses calibration and compensation of the birefringence of the cryostat windows, which is important in polarization-sensitive measurements such as the transient Faraday/Kerr rotation experiments.

Publications

[1] Z. Chen, S. G. Carter, R. Bratschitsch, P. Dawson and S. T. Cundiff, "Effects of Disorder on Electron Spin Dynamics in a Semiconductor Quantum Well," Nature Physics (in press).

[2] Z. Chen, R. Bratschitsch, S. G. Carter, S. T. Cundiff, D. R. Yakovlev, G. Karczewski, T. Wojtowicz, and J. Kossut, "Electron Spin Polarization through Interactions between Excitons, Trions and the Two-Dimensional Electron Gas,"

Phys. Rev. B. (in press).

[3] S. G. Carter, Z. Chen and S. T. Cundiff, "Optical Measurement and Control of Spin Diffusion in n-Doped GaAs Quantum Wells," Phys. Rev. Lett. **97**, 136602 (2006).

[4] R. Bratschitsch, Z. Chen, S. T. Cundiff, E. A. Zhukov, D. R. Yakovlev, and M. Bayer, G. Karczewski, T. Wojtowicz, and J. Kossut, "Electron Spin Coherence in n-Doped CdTe/CdMgTe Quantum Wells," Appl. Phys. Lett. **89**, 221113 (2006).

[5] R. Bratschitsch, Z. Chen, S. T. Cundiff, D. R. Yakovlev, G. Karczewski, T. Wojtowicz and J. Kossut, "Electron Spin Dephasing in n-Doped CdTe/(Cd, Mg)Te Quantum Wells," Phys. Status Solidi B **243**, 2290-2292 (2006).

[6] Z. Chen, R. Bratschitsch and S. T. Cundiff, "Interference Effects in Transient Kerr Spectra of a Semiconductor Multilayer Structure," Opt. Lett. **30**, 2320-2322 (2005).

[7] R. Bratschitsch, Z. Chen and S. T. Cundiff, "Ultrafast Spin Phenomena in Highly Excited n-Doped GaAs," Phys. Status Solidi C **0**, 1506-1508 (2003).

Chapter 2

Experimental Techniques

For the study of carrier dynamics in semiconductors, ultrafast pump-probe spectroscopy techniques are widely used [15]. A pump pulse excites carriers in semiconductors, and a delayed probe pulse monitors the time evolution of optically excited carriers. The work presented in this thesis is focused on the study of spin dynamics in semiconductor materials. For such study, optical spin orientation is implemented into the pump-probe experiment, to enable optical generation and detection of carrier spins in semiconductors. The transient Faraday/Kerr rotation technique, which are essential for most of the experiments presented in this thesis, uses Faraday/Kerr effects induced by spin magnetization in the medium to extract dynamical information of carrier spins. With the addition of an applied magnetic field, the time evolution of the spin coherence, defined by the applied field, can be followed by optical pulses (refer to Section 1.2.1). We start this chapter by presenting general aspects of the pump-probe experiments. The selection rules in semiconductors are then discussed to illustrate carrier spin polarization through optical orientation. The transient Faraday/Kerr rotation technique is introduced, with the experimental setup discussed. We conclude the chapter by presenting preliminary results measured on bulk GaAs samples, which illustrate information regarding spin dynamics that can be obtained from Faraday/Kerr rotation measurements.

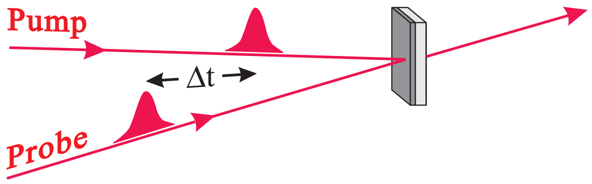

Figure 2.1: Schematic for a pump-probe measurement. The temporal dynamics is monitored by varying the relative time delay between the pump and probe pulses.

2.1 Pump-probe spectroscopy

Pump-probe experiments using ultrafast lasers enable direct measurements of carrier dynamics, with a temporal resolution limited only by the duration of the laser pulse. Carrier dynamics initiated by a pump pulse can be monitored by varying the relative time delay of a probe pulse (Figure 2.1). This is done in practice by using a translation stage that varies the optical path length of one beam relative to the other. A pump-probe experiment measures the differential transmission by the probe pulse, with and without the pump excitation. With a pump excitation, the photoexcited electrons fill states in the conduction band, which would otherwise be available for excitation of valence electrons by probe photons, therefore induce a change in the transmitted probe intensity. The direct application of pump-probe experiments is to track the carrier population decay as a function of time, giving information of the optically created carrier lifetime. To monitor spin dynamics of the carrier, circularly polarized pump and probe pulses are used. Pump pulse preferentially excite carrier spins in one of the spin subband, and a co-circular probe pulse measure the spin dynamics in the same spin subband. In Section 2.3, we will introduce the transient Faraday/Kerr rotation technique, which is a special version of the pump-probe experiment. The principal advantage of Faraday/Kerr rotation over traditional pump-probe is the sensitivity of the measurement. Before proceeding to the Faraday/Kerr rotation technique, we first discuss the selection rules through which spin polarized carriers can be generated with light.

2.2 Generation of spin polarized carriers

The carrier spins in semiconductors can be oriented using optical techniques in which circularly polarized photons transfer their angular momenta to electrons (optical orientation). Specifically, a photon of right or left circularly polarized light has a projection of its angular momentum in the light direction equal to +1 or -1, respectively. As a consequence of angular momentum conservation, the photoexcited electron and hole are spin-polarized following the absorption of the photon, and the angular momentum is distributed between the electron and hole according to the selection rules.

We illustrate basic principles of optical orientation by the example of GaAs, which is representative of a large class of zinc-blende semiconductors. A schematic band structure of GaAs is depicted in Figure 2.2(a). GaAs is a direct bandbap material, i.e. both the minimum of the conduction band and maximum of the valence band lie at $k = 0$ in momentum space. The bandgap is $E_g = 1.52$ eV at low temperature, and energy of the spin split-off band is lower than the heavy and light hole bands by $\Delta_{so} = 0.34$ eV (we ignore optical orientation due to the split-off band, because of its much higher interband energy).

For the lowest-lying bands in the semiconductors of interest here, the character of the conduction band is "*s*-like" while that of the valence bands is "*p*-like". This reflects the relative contributions to the density of states in each band from atomic *s* and *p* orbitals of the atoms that form the solid. An electron state in the

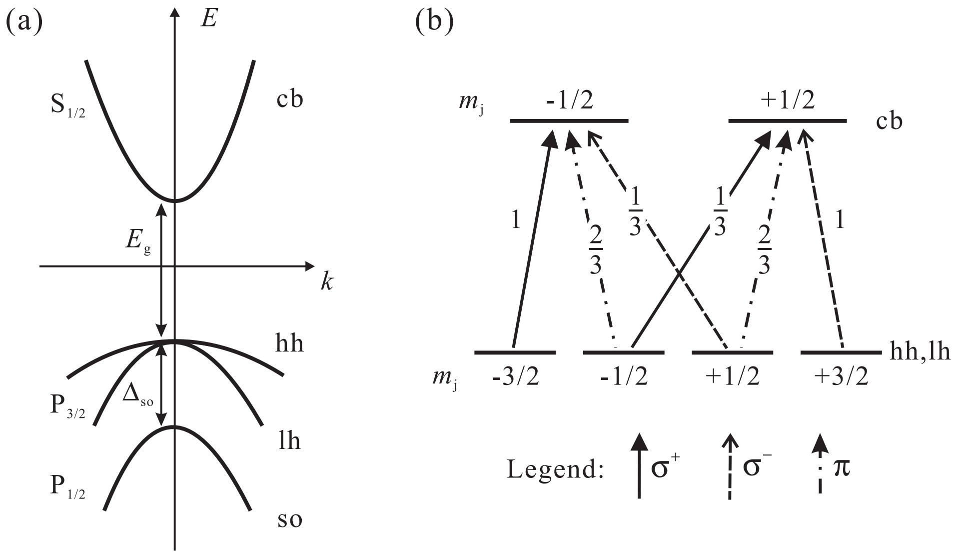

Figure 2.2: (a) Schematic band structure of GaAs near the interband gap. E_g is the bandgap and Δ_{so} is the energy splitting of split-off band; cb, conduction band; hh (lh), heavy (light) hole valence band; so, split-off valence band. (b) Selection rules for interband transitions between the heavy and light hole valence bands and conduction band for σ^+, σ^- and π polarized light. The numbers denote the relative transition intensities.

conduction band is described by the Bloch wavefunction

$$\psi^c_{\vec{k}m} = u_m(\vec{r}) \exp(i\vec{k} \cdot \vec{r}). \tag{2.1}$$

Here m represents the electron spin direction ($m = \pm 1/2$), $\vec{k}$ is the crystal momentum and u_m is the Bloch amplitude, i.e. an invariant under symmetry transformations of the crystal. For the conduction band states, the Bloch amplitudes can be approximately separated into orbital and spin parts [16]:

$$u_{1/2}(\vec{r}) = S\uparrow, u_{-1/2}(\vec{r}) = S\downarrow, \tag{2.2}$$

with S denoting the coordinate part, and ↑ (↓) the spin part of the s-like Bloch amplitude. Unlike the "s-like" conduction band, the valence band is "p-like" (L=1), so that the spin-orbit coupling is sizable. This means that the Bloch amplitudes for the valence band electrons should be expressed as eigenstates of the total angular momentum, $\mathbf{J} = \mathbf{L} + \mathbf{S}$, and its z-component, J_z. We denote the Bloch amplitudes according to the total angular momentum J and its projection onto the positive z axis m_j as $|J, m_j\rangle$. Specifically, the eigenstates for the heavy hole valence band are written as $|3/2, \pm 3/2\rangle$, $|3/2, \pm 1/2\rangle$ for light holes, and $|1/2, \pm 1/2\rangle$ for split-off holes. The spin-orbit coupling removes the degeneracy between $J = 3/2$ and $J = 1/2$, so that the split-off hole band is Δ_{so} below the heavy and light hole valence band.

In analogy to atoms, interband optical excitation excites electrons from the valence to conduction band in semiconductors following selection rules. The transition probability for an electron excited from the valence to conduction band under an incident electromagnetic field $\vec{E}$ is given by the Fermi's golden rule

$$R_{vb \to cb} = \frac{2\pi}{\hbar} \left| \langle cb| - e\vec{r} \cdot \vec{E} |vb\rangle \right|^2 \delta(E_g - \hbar\omega), \tag{2.3}$$

with E_g the energy of the bandgap. The interband selection rules are then represented by the dipole moments, $\langle cb|\hat{D}|vb\rangle$, with $\hat{D} \equiv -e\vec{r}$, corresponding to transitions between the conduction band and different sub-bands of the valence band. The matrix elements of the dipole moment between the heavy hole valence band and the conduction band follows [16]

$$\begin{aligned} &\langle S \uparrow \left| \hat{D} \right| 3/2, 3/2\rangle = -\sqrt{1/2}(\hat{\lambda} + i\hat{\mu}), && \langle S \downarrow \left| \hat{D} \right| 3/2, 3/2\rangle = 0, \\ &\langle S \uparrow \left| \hat{D} \right| 3/2, -3/2\rangle = 0, && \langle S \downarrow \left| \hat{D} \right| 3/2, -3/2\rangle = \sqrt{1/2}(\hat{\lambda} - i\hat{\mu}), \end{aligned} \tag{2.4}$$

and the matrix elements of the dipole moment between the light hole valence band and the conduction band follows

$$\begin{aligned} &\langle S \uparrow \left| \hat{D} \right| 3/2, 1/2\rangle = \sqrt{2/3}\hat{\nu}, && \langle S \downarrow \left| \hat{D} \right| 3/2, 1/2\rangle = -\sqrt{1/6}(\hat{\lambda} + i\hat{\mu}), \\ &\langle S \uparrow \left| \hat{D} \right| 3/2, -1/2\rangle = \sqrt{1/6}(\hat{\lambda} - i\hat{\mu}), && \langle S \downarrow \left| \hat{D} \right| 3/2, -1/2\rangle = \sqrt{2/3}\hat{\nu}. \end{aligned} \tag{2.5}$$

Here $\hat{\lambda}$ and $\hat{\mu}$ are unit vectors in a plane perpendicular to the momentum, and $\hat{\nu}$ is a unit vector along the momentum. The same constant has been removed from the dipole moments in Equation 2.4 and 2.5 for simplicity. The electric field will couple to different interband transitions depending on the dot-product between the field vector and different dipoles (transition probability $R \propto \left|\langle cb|\vec{D} \cdot \vec{E}|vb\rangle\right|^2$). A $\sigma^{\pm}$ circularly polarized photon, with the electric field in $\sqrt{1/2}(\hat{\lambda} \pm i\hat{\mu})$ direction, will couple to both the heavy and light hole transitions, while a π polarized photon (with field in $\hat{\nu}$ direction) can also couple to the light hole transition. The complete selection rules for interband transitions between the heavy and light hole valence bands and the conduction band are depicted in Figure 2.2(b). The relative transition intensities for the different transitions are also denoted in the figure.

The spin polarization of the photoexcited conduction band electrons depends on the photon energy. For a photon energy tuned to the interband transition below the split-off energy, only the heavy and light hole subbands contribute. We define the electron spin polarization as

$$P = (n_+ - n_-)/(n_+ + n_-), \tag{2.6}$$

with n_+ and n_- the densities of electrons polarized parallel ($m_s = 1/2$) and antiparallel ($m_s = -1/2$) to the light propagation direction. For a zinc-blende structure (such as that of GaAs and CdTe), the spin polarization is equal to -50% ($+50\%$) at the moment of a σ^+ (σ^-) photoexcitation. This is due to the different transition probabilities between the heavy hole and light hole subbands, as depicted in Figure 2.2(b). Figure 2.2(b) also suggests a 100% spin polarization in the conduction band in semiconductors where the degeneracy of the heavy and light hole states is lifted. This is achieved in strained bulk zinc-blende crystals or in quantum well heterostructures.

2.3 Transient Faraday and Kerr rotation

2.3.1 Faraday effect

The Faraday effect is the rotation of linearly polarized light as it passes through a material with a circular birefringence induced by an applied magnetic field. The medium equation (electric displacement) for materials exhibiting the Faraday effect is [17]

$$\vec{D} = \epsilon\vec{E} + i\epsilon_0\gamma\vec{B} \times \vec{E}, \tag{2.7}$$

where γ is the magnetogyration coefficient that determines the rotatory power. With a magnetic field in the light propagating direction $\vec{B} = B\hat{z}$, the invariant states to the above equation are $\vec{E} = E_0(\hat{x} \pm i\hat{y})$ for $\sigma^{\pm}$ circular polarization. The corresponding index of refraction can be written as

$$n'_{\pm} = \sqrt{n \pm \gamma B} \tag{2.8}$$

for σ^+ and σ^- helicities, respectively. The induced circular birefringence corresponds to the different indices of refraction for σ^+ and σ^- light. Because linearly polarized light can be viewed as a superposition of σ^+ and σ^- light, the circular birefringence will add a phase difference between the two components while the light travels through the medium. This phase difference corresponds to an angle of rotation of the linear polarization, hence the name Faraday rotation, with the rotation angle

$$\theta_F = \frac{\pi(n'_+ - n'_-)L}{\lambda_0} \approx \frac{\pi\gamma BL}{n\lambda_0}, \tag{2.9}$$

with L the medium thickness and λ_0 the free space wavelength of the light.

The spin dynamics in semiconductors is measured by implementing Faraday effect into pump-probe experiments. The Faraday effect is now induced by carrier spins, which can be generalized as a pump-excited spin magnetization in the light propagation direction (the origin of Faraday rotation resulting from optical

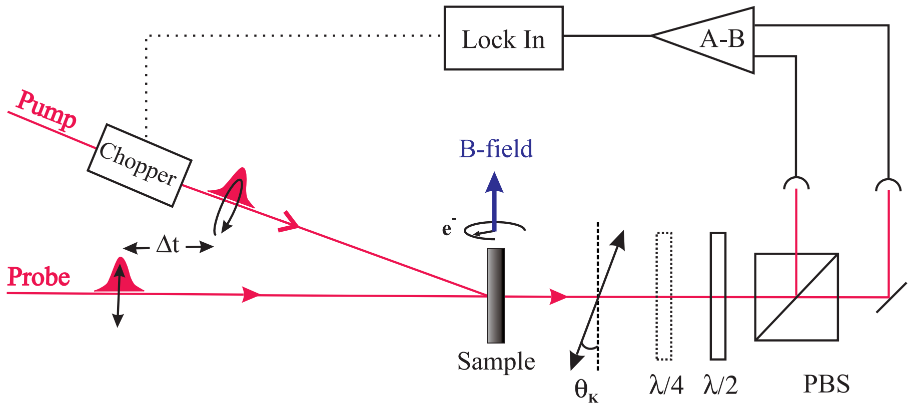

Figure 2.3: Schematic setup for transient Faraday rotation measurements. PBS, polarizing beam splitter; $\lambda/2$, half-wave plate; $\lambda/4$, quarter-wave plate. An optional quarter-wave plate is inserted for the Faraday ellipticity measurement.

orientation will be discussed in Chapter 3). By monitoring the rotation angle of the probe linear polarization as a function of the time delay, the dynamics of spin polarization in the beam direction is directly measured. A schematic of transient Faraday rotation setup is shown in Figure 2.3.

2.3.2 Experimental details

The pump and probe pulses are provided by a mode-locked Ti:Sapphire laser system (Coherent Mira 900), pumped by a 5 W CW Diode-Pumped Laser at 532 nm (Coherent Verdi V5). It provides optical pulses in the near-infrared wavelength range, with a repetition rate of 76 MHz and a duration less than 200 fs (due to spatial chirp caused by optical components in the setup, the pulse duration is about 300 fs before it arrives at the samples, based on autocorrelation measurements). The normal spectral linewidth of the laser output is about several nm, with the center wavelength tuned near the interband transition of the semiconductor samples. The laser output is split into pump and probe pulses, with the probe pulse time-delayed by a 60 cm translation stage (Newport IMS600PP), up to a delay of 4 ns. A retroreflecting mirror is mounted on the stage to minimize beam misalignment due to stage movement. The pump beam is chopped either by an optical chopper (Stanford Research SR540) that goes up to 3.7 kHz, or an acousto optical modulator (Isomet 1250C), so that a lock-in amplifier can be used for phase-sensitive detection.

The pump and probe beams are focused to a ~ 100 μm and ~ 50 μm spot on the sample, respectively. This is to ensure that the probe beam will only measure a part of the area within that excited by the pump beam and hence probe uniform excitation. The sample is mounted on a sample mount within a magneto-optical cryostat (Janis split-coil superconducting magnet cryostat, model 12-CNDT) capable of temperatures from $2-300$ K and magnetic fields from 0-6.5 Tesla.

As shown in Figure 2.3, a circularly polarized pump pulse excites spin polarized carries in the semiconductor samples, with the spin polarization oriented in the pump beam direction. They start to Larmor-precess in an in-plane applied magnetic field (Voigt geometry, with the magnetic field perpendicular to the beam direction). A linear probe pulse at a later time is used to detect the spin through the Faraday effect. The circular birefringence created by the spin magnetization will produce a rotation of the linear polarization of the transmitted probe, which is detected by a polarization bridge. By varying the time delay between pump and probe pulse, one can monitor the spin precession of the carriers in the time domain. A balance detection scheme is employed in order to sensitively detect small rotation signals. At negative time delays (when the pump has no effect), the probe linear polarization is rotated by a half-wave plate to be at 45° with respect to a polarizing beam splitter (a Glan Laser prism polarizer in our experiments). This ensures equal intensities for the orthogonal polarizations that exit the beam splitter, which are directed to two photodiodes. When balanced, the difference current between the two photodiodes is zero. At positive delays after pump excitation, however, the Faraday rotation of the probe is detected as a slight imbalance of the difference current between the two photodiodes. The nonzero difference current is amplified by an op-amp (with several amplification settings from 0.1 MΩ to 10 MΩ), and passed on to a lock-in amplifier (Stanford Research SR830). The main advantage of the balance detection scheme is that fluctuations of the laser intensity are manifested simultaneously in both arms of the bridge and are thus canceled. This is, however, not the case for differential transmission pump-probe measurements.

Similar to Faraday rotation, a difference in absorption coefficients of the medium for the two circularly polarized components will induce ellipticity in the transmitted light, which is called Faraday ellipticity. We will study the Faraday ellipticity spectrum in Chapter 3. Experimentally, the Faraday ellipticity is measured by inserting an additional quarter-wave plate before the polarization bridge, as shown in Figure 2.3. The purpose of the quarter-wave plate is to convert the left and right circular polarizations into orthogonal linear polarizations, so that the two photodiodes essentially measure the difference intensity of the left and right circular polarization components in a linear probe beam. The difference current from the balanced detector is then proportional to the Faraday ellipticity.

For the study of thick, opaque samples, a transient Kerr rotation technique is used, which is similar to a transient Faraday rotation measurement, except that it is the polarization of the reflected probe beam that is measured. A transient Kerr rotation setup is shown in Figure 2.4. A typical transient Kerr rotation signal is plotted in Figure 2.5, which is measured in a lightly n-doped CdTe quantum well sample. The data for delay times over 100 ps can be well described by an

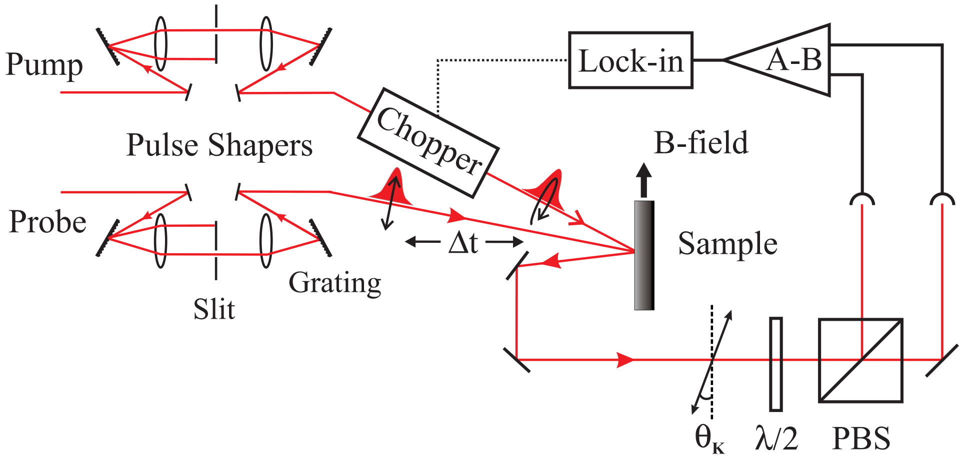

Figure 2.4: Schematic setup for transient Kerr rotation measurements. Both pump and probe pulses are spectrally filtered through pulse shaping technique, to enable independent tuning of their photon energies. The spectral linewidths of the pulses are also narrowed for spectrally resolved measurements.

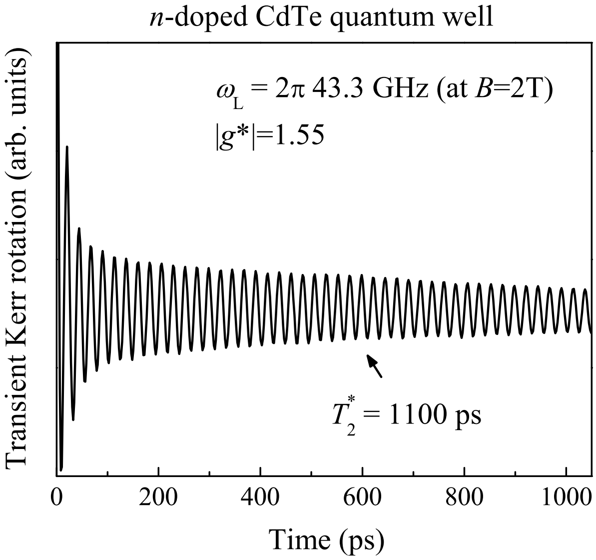

Figure 2.5: Kerr rotation data from a lightly n-doped CdTe quantum well. Pump and probe photon energies are tuned near the exciton resonance of the quantum well. The long-delay signal can be well fitted by an exponential oscillation decay, giving information of the electron spin dephasing time (T_2^*), Larmor precession frequency (ω_L) and the effective g factor (g^*).

exponential oscillation decay in the form of

$$\theta_K = A\exp(-t/T_2^*)\cos(\omega_L t), \tag{2.10}$$

with T_2^* the spin dephasing time and $\omega_L = g^*\mu_B B/\hbar$ the Larmor precession frequency. From a nonlinear fit of the data with Equation 2.10, we can obtain the spin dephasing time, Larmor precession frequency under the magnetic field, and the effective Landé g factor. A Larmor precession frequency of $\omega_L = 2\pi$ 43.3 GHz is measured at $B = 2$ T, corresponding to $|g^*| = 1.55$. A T_2^* over 1 ns is retrieved from the data. As this time constant exceeds lifetimes of optically created carriers ($\sim$ 100 ps), it is the spin dephasing time of the resident electrons. A fast exponential decay at short time delay is related to exciton spin dephasing, which will be detailed in Chapter 4.

2.3.3 Two-color measurements

In a typical transient Faraday/Kerr rotation measurement, both the pump and probe photon energies (degenerate) are tuned near the vicinity of some absorption resonances for resonant excitation and detection sensitivity. A two-color measurement, where the pump and probe photon energies can be independently tuned, is preferred when multiple resonances in the samples are present. A two-color measurement is useful for selective excitation and detection through different resonances (carrier species). It is especially helpful for spectral studies of the Faraday/Kerr rotation, where the pump photon energy is varied with the probe energy fixed near a resonance, and vice versa, so that different effects from excitation and detection can be well separated. We perform a two-color transient Faraday/Kerr rotation measurement by using a pulse shaping technique [18]. Both pump and probe pulses are spectrally filtered through a 4-f pulse shaper with a movable slit, to enable independent tuning of their photon energies, which is shown in

Figure 2.4.

Figure 2.4 shows the basic pulse shaping apparatus, which consists of a pair of diffraction gratings and lenses and a movable slit. The lenses are 2-inch bi-convex lenses with $f = 15$ cm. The diffraction gratings are of 1200 grooves/mm with a blaze angle at 750 nm. The width of the slit is adjustable with width ranging from 0 to 4 mm (Melles Griot SLT 201). The frequency components contained within the incident laser pulse are angularly dispersed by the first diffraction grating, and are focused at the back focal plane of the first lens, where different frequency components are spatially separated. The second lens and grating recombine all frequency components into a collimated beam. The adjustable slit, placed in the back focal plane of the first lens, narrows the pulse spectrum depending on its width. The center wavelength is controlled by translating the slit in the focal plane. The 4-f pulse shaper used has a spectral resolution of $\sim$ 0.1 nm. The spectral linewidths of the pulses are normally adjusted to be $\sim$0.2 nm for spectrally resolved measurements. By using separate pulse shapers for pump and probe beams, their photon energies can be independently tuned, hence a two-color measurement.

2.4 Preliminary measurements on bulk GaAs

A preliminary study is performed by measuring spin dynamics in bulk GaAs. The importance of GaAs for spintronics and quantum computing applications has been recently underlined by the observation of rather long spin relaxation times (on the order of 100 ns) in n-doped samples [19]. We study nominally undoped and n-doped bulk GaAs (doping densities of $2.4 - 5.3 \times 10^{16}$, $2 - 3 \times 10^{17}$, and $2 - 3.3 \times 10^{18}$ cm^{-3}) by performing transient Faraday rotation experiments in the Voigt geometry, under a magnetic field of 4 Tesla. The GaAs samples are thinned down to 30 μm and mounted on a sapphire disk, for transmission measurements.

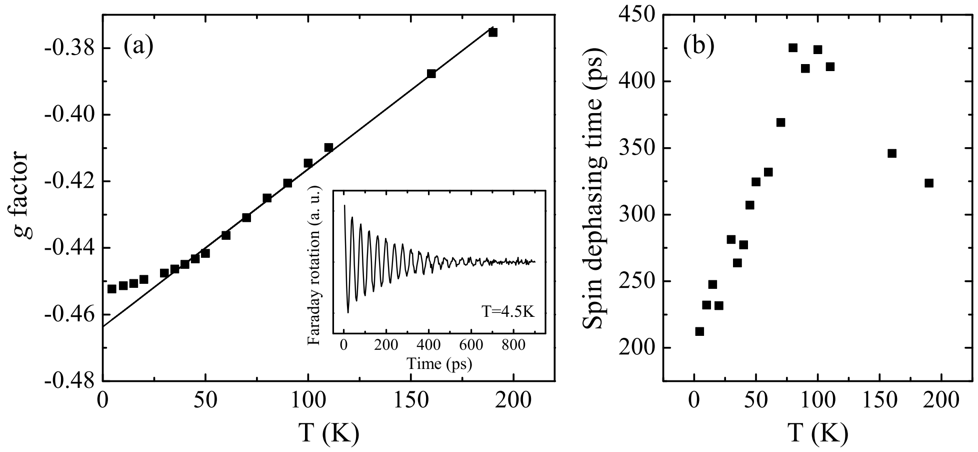

Figure 2.6: (a) g factor and (b) spin dephasing time (T_2^*) as a function of temperature in undoped bulk GaAs. Solid line in (a) is a linear fit for data above 40 K. $B = 4$ T. Inset: Transient Faraday rotation signal at $T = 4.5$ K.

The pump and probe pulses are degenerate in photon energy and are tuned near the bandgap of GaAs.

2.4.1 Undoped GaAs

We start with the nominally undoped GaAs sample. The transient Faraday rotation signal at $T = 4.5$ K and $B = 4$ T is shown in the inset of Figure 2.6. A spin dephasing time of $T_2^* \sim 200$ ps and g factor of $g^* = -0.452$ are retrieved from a nonlinear fit using Equation 2.10. We measure the g-factor as a function of temperature, which is shown in Figure 2.6(a). For temperature above 40 K, a rather good linear dependence on temperature is observed, with a linear dependence of $g^*(T) = -0.46 + 5 \times 10^{-4}$T. This is in agreement with the linear temperature dependence reported in Reference [20]. Below 40 K, the g factor substantially deviates from the linear dependence. The donor binding energy for GaAs is $\sim$ 4 meV, or 40 K [21, 22]. Below 40 K, electrons are largely localized by binding with the donors or impurities, and above 40 K, are largely free. We believe the deviation of g factor at low temperature is related to electron localization at donor sites. A theory including effects from donors is however unavailable. In Section 1.2.3, a g^* dependence on the energies of fundamental gaps in semiconductors is established. The g^* dependence on temperature can therefore be represented by the temperature variation of the energy gaps, which are well known with high accuracies [23]. A calculation of g^* dependence on temperature was carried out [23] by using the five-band $k \cdot p$ model discussed in Section 1.2.3 [14]. The theoretical prediction by $k \cdot p$ theory is in the opposite direction than the experimental results, manifesting the need for appreciable, temperature dependent corrections of this band model.

The temperature dependence of the spin dephasing time is plotted in Figure 2.6(b). The spin dephasing time T_2^* at first increases with temperature, and then starts to decrease at temperature over 80 K. The decrease of T_2^* with temperature above 80 K has been found to be consistent with the D'yakonov-Perel' mechanism [24], which is the dominant spin dephasing mechanism for delocalized electrons. At low temperature, the increase of T_2^* with temperature is rather counter-intuitive, because momentum scattering rate is usually increased with increasing temperature. It can be qualitatively explained with a motional narrowing picture, in which the correlation time decreases with increasing temperature much faster than the dispersion of local Larmor frequencies.

2.4.2 n-doped GaAs

We study spin dynamics in the four bulk GaAs samples with different doping concentrations [25]. A comprehensive study of the electron spin decoherence time over a large range of doping levels in bulk n-GaAs has already been presented elsewhere [8], with spin coherence time reaching its maximum near the metal-

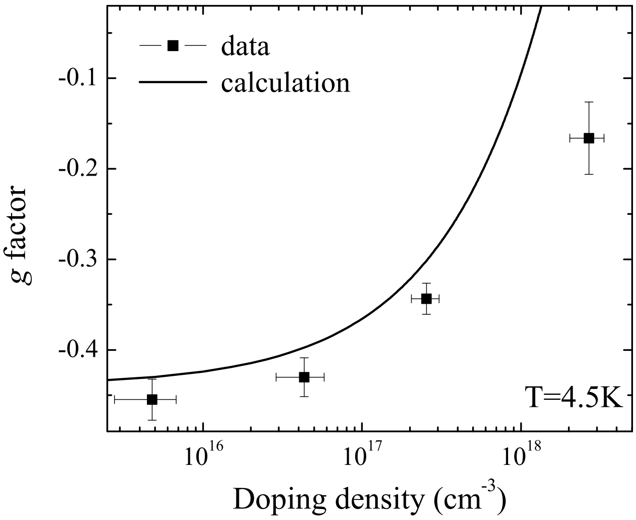

Figure 2.7: Measured g factors of the four GaAs samples are plotted as a function of their doping density. The solid line is the calculated g^* as described in the text.

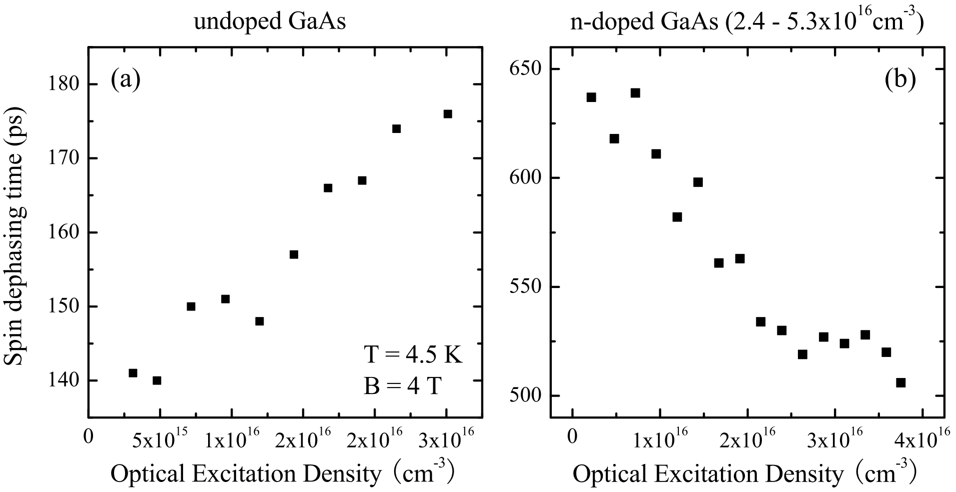

Figure 2.8: Electron spin dephasing time T_2^* in (a) undoped GaAs and (b) n-doped GaAs ($2.4 - 5.3 \times 10^{16}$ cm^{-3}) as a function of optical excitation density. $T = 4.5$ K and $B = 4$ T.

insulator transition. We focus our study on the doping concentration dependence of the electron Landé g factor. In Figure 2.7, g factors for the four GaAs samples measured at 4.5 K are plotted with their doping concentration. The g factor increases monotonically with increasing doping density. In Section 1.2.3, g^* of the conduction electron is shown to depend on its energy. This energy dependence can be further simplified as a linear dependence $g^*(E) = -0.44 + 6.3 \times E$ (eV), within a small energy range near the conduction band edge [26]. The variation of g factor with carrier concentration can then be understood as its dependence on the Fermi energy, with the electron energy at the Fermi edge increased with increasing doping density due to filling of conduction band from dopant electrons. The g factor measured through Faraday rotation should be that of electrons at the Fermi energy. With the assumption of a linear energy dependence of g^*, a Fermi-Dirac distribution with $T = 0$ K, and a parabolic conduction band near the band edge, we are able to calculate the g factor dependence on electron density, which is shown as a solid line in Figure 2.7. At low densities, the calculated g^* is higher than the experimental values due to the set value ($g_0 = -0.44$) at conduction band edge. The discrepancy at high electron concentration is probably because of the assumption of linear energy dependence, which is not valid for energies far away from the conduction band edge [27].

Figures 2.8(a) and (b) show the electron spin dephasing time T_2^* in n-doped GaAs ($2.4 - 5.3 \times 10^{16}$ cm^{-3}) and nominally undoped GaAs as a function of optical excitation density. While T_2^* increases almost linearly with increasing optical excitation density for the undoped sample, it shows an opposite behavior for the n-doped sample. By increasing the optical excitation density, we also increase the carrier temperature of the electrons. The results in Figure 2.8 indicate dramatic difference in spin dephasing mechanisms under different doping concentration.

Chapter 3

Spectral study of transient Faraday and Kerr effects

For the study of carrier spins in semiconductors, the magneto-optical Faraday and Kerr effects, which are measured in transmission and reflection geometry, respectively, are extensively used [28, 29]. The transient versions of these techniques are especially powerful for extracting spin dynamics in semiconductors [13, 30]. Spectral studies of the transient Faraday and Kerr effects reveal the underlying spin-dependent optical nonlinearities [31, 32], improve understanding of the techniques themselves, and, as shown in Chapter 4, distinguish the spin relaxation from different species. In this chapter, we experimentally study the spectra of the transient Faraday and Kerr effects near exciton resonances of an undoped GaAs multiple quantum well. A multilayer calculation using a characteristic matrix method is performed to account quantitatively for the linear transmission (reflectivity) spectra and the Faraday (Kerr) spectra. We found that the Faraday and Kerr spectra do not obey a Kramers–Kronig relation, which should be valid for a simple slab of nonlinear material. This anomalous behavior is found to be due to interference with multiple reflections within the sample structure on the Kerr spectra [33].

3.1 Introduction

When a linearly polarized light is incident on a sample, a difference in the index of refraction for the two circularly polarized components causes a rotation of the polarization axis of the transmitted light, which is referred to as Faraday rotation. Likewise, a difference in the absorption coefficients induces ellipticity in the transmitted light, which is called Faraday ellipticity. A difference in optical coefficients can be created by an external magnetic field or, as in the case of the photo-induced Faraday effect, by optical orientation due to photoexcitation. In a transient Faraday measurement, a circularly polarized pump pulse preferentially excites carriers into one of the two spin subbands and creates an imbalance of spin population. This population imbalance will cause a change of the index of refraction and/or absorption coefficient, which is detected by the Faraday effect. The resultant nonlinearities in the optical response can arise from:

(1) saturation of the resonance owing to phase-space filling (arising from the Pauli exclusion principle);

(2) shift of the resonance energy due to band-gap renormalization and/or Coulomb screening of the exciton binding energy;

(3) enhancement of scattering due to excitation induced dephasing.

To distinguish the contribution of the above mechanisms to the Faraday spectra, we start with the index of refraction and absorption spectra for the exciton resonance in a quantum well. A good approximation to represent the exciton resonance is to use the oscillator model [34]. The complex dielectric constant for a single resonance from the oscillator model follows

$$\epsilon(\omega) = \epsilon_b + \frac{f}{\omega_0^2 - \omega^2 - i\gamma\omega}, \tag{3.1}$$

where ϵ_b is the background dielectric constant, f is the oscillator strength, ω_0 is the resonance frequency and γ is the damping rate for the exciton. The complex dielectric constant is equal to the square of the complex index of refraction $\tilde{n} = n + i\kappa$. The index of refraction $n(\omega)$ and the absorption coefficient $\kappa(\omega)$ therefore is equal to $\mathrm{Re}(\epsilon(\omega))^{1/2}$ and $\mathrm{Im}(\epsilon(\omega))^{1/2}$, respectively. A dispersive refractive index and a peak absorption are obtained around the resonance, as shown in Figure 3.1.

In Figure 3.1, schematic of the Faraday rotation and ellipticity near a resonance is shown for a shift of resonance energy and saturation. The Faraday spectra are obtained based on the linear spectra for opposite helicities of circular polarization, with the nonlinearity described by a small change of resonant energy or a decrease of the oscillator strength for one helicity, and the linear spectra for the other helicity unchanged. Figure 3.2(a) shows the spectral behaviors of Faraday rotation and ellipticity induced by an energy shift, calculated by using an energy shift of 0.1 γ, with γ the full width half maximum linewidth of the resonance. The rotation and ellipticity spectra are related by the Kramers–Kronig relation. This is expected because the rotation and ellipticity spectra are due to the differences of the linear spectra, each of which obeys the Kramers–Kronig relation.

The Kerr effect can be described as the Faraday effect in reflection, which is preferred for the study of thick, opaque samples. For a single interface, one expects the Kerr spectrum to be related to the Faraday spectrum through the Kramers–Kronig relation, as is the case for linear reflectivity and transmission spectra. This is shown in Figure 3.2(b) for energy shift induced Faraday and Kerr rotation spectra.

3.2 Sample characteristics and experiments

Experiments are carried out on a GaAs/$\mathrm{Al_{0.3}Ga_{0.7}As}$ multiple quantum well, which consists of 10 periods of a 10-nm well and a 10-nm barrier. The sample

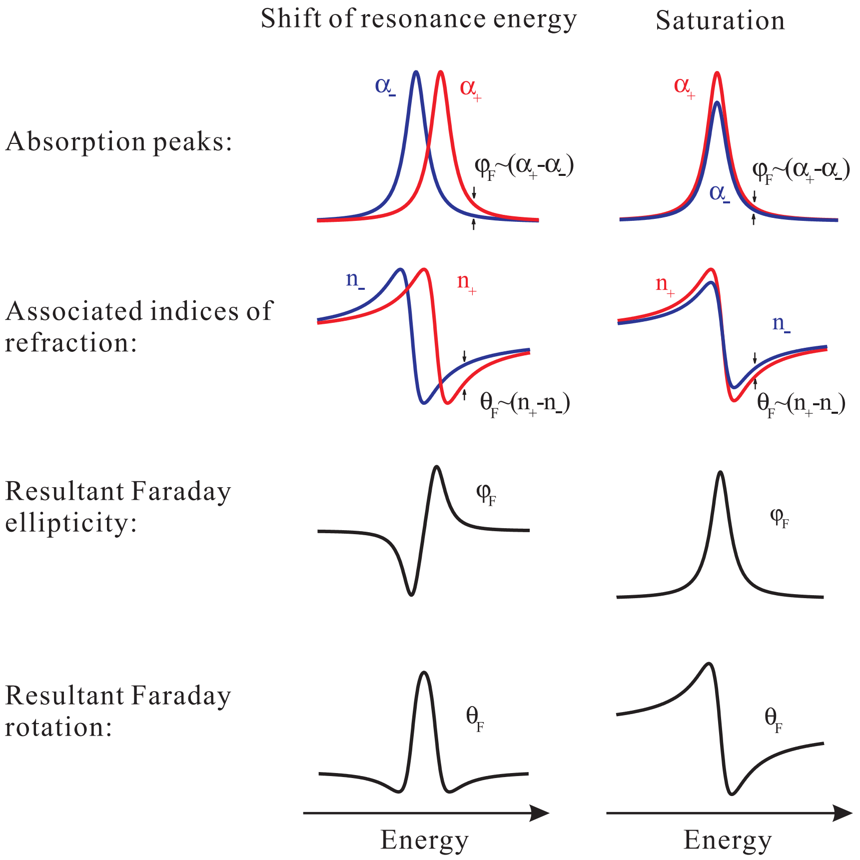

Figure 3.1: Schematic of the photo-induced Faraday rotation and ellipticity near a resonance due to shift of resonance energy and saturation.

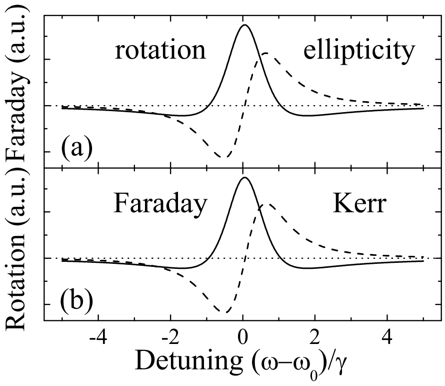

Figure 3.2: Faraday and Kerr effect spectra resulting from an energy shift, calculated for a slab of nonlinear medium. Reflection from the front interface alone is considered for the Kerr effect.

is grown by molecular beam epitaxy on a GaAs substrate. It consists of nominally a 0.5 μm GaAs buffer layer, a 0.3 μm $Al_{0.4}Ga_{0.6}As$ etch stop layer, 120 nm superlattice, 0.3 μm GaAs, 0.3 μm $Al_{0.3}Ga_{0.7}As$, the 10 periods quantum well, 0.2 μm $Al_{0.3}Ga_{0.7}As$ and a 100 Å GaAs cap layer. The sample is mounted on a sapphire plate (GaAs cap layer facing sapphire plate) with the opaque GaAs substrate removed by etching. The nominal sample structure after etching is shown in Figure 3.3(a).

The absorption spectrum of the sample is shown in Figure 3.3(b), where the features at 1.539 eV and 1.545 eV correspond to the heavy-hole and light-hole exciton resonances in the quantum well. We measure spectrally the transient Faraday and Kerr effects under a magnetic field of 4 T applied normal to the quantum well growth direction. The spectral width of the pump and probe pulses is about 1 nm, and the laser energy is scanned in the vicinity of the heavy-hole and light-hole exciton resonances of the quantum well. Average powers are 10 mW in the pump beam and 0.2 mW in the probe. The heavy-hole exciton density due to pump excitation is estimated to be 10^{11} cm^{-2} per quantum well. All experiments are performed at 4.5 K. Care is taken to compensate for strain-induced birefringence in the cryostat windows (refer to Appendix A).

3.3 Linear spectra

3.3.1 Reflection and transmission

Linear transmission and reflectivity spectra of the sample are measured by using a white light source and detected by a spectrometer. The reflectivity spectra are plotted in Figure 3.4. Both the transmission (not shown) and reflectivity spectra show fringe patterns, with a fringe periodicity of $\sim$ 60 meV near the exciton resonances. The fringes are caused by interference between reflections from

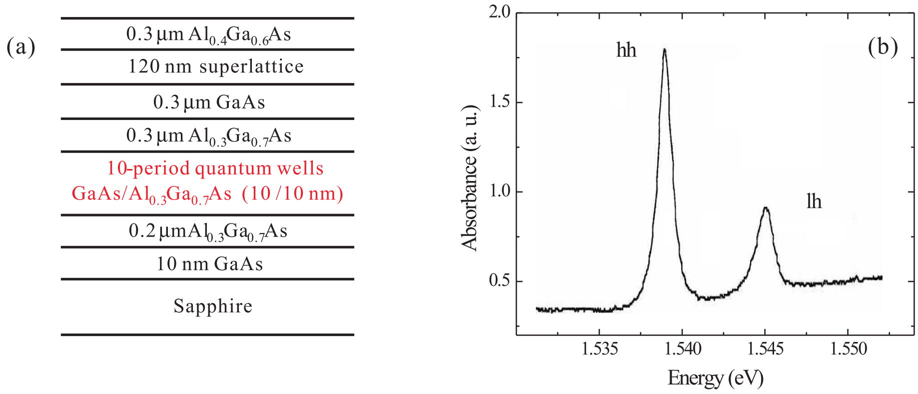

Figure 3.3: (a) Layer structure of the GaAs quantum well used. (b) Absorption spectrum near the heavy-hole (hh) and light-hole (lh) exciton resonances of the quantum well

the front and back surfaces of the sample. As the excitation spot moves across the sample surface, we observe a shift of the fringes, which is illustrated in Figure 3.4. This indicates that the sample is slightly wedged (4% across the sample). The heavy-hole exciton resonance may appear as an absorption dip lineshape, a dispersive lineshape or a peak line shape, depending on where the exciton resonance sits on the fringes. The exciton resonances in the transmission spectra (not shown) are always a dip regardless of the sample thickness. The variation of sample thickness, which is not preferred in most cases, does provide us opportunities to check the effect of linear optical effects (such as interference) on the Faraday and Kerr effect spectra, which in general depends on the nature of the optical nonlinearities. We will discuss it in detail in Section 3.4.

3.3.2 Characteristic matrix method

A calculation of the linear spectra for the specific sample used is a necessary prerequisite to account for the experimental Faraday and Kerr spectra. The

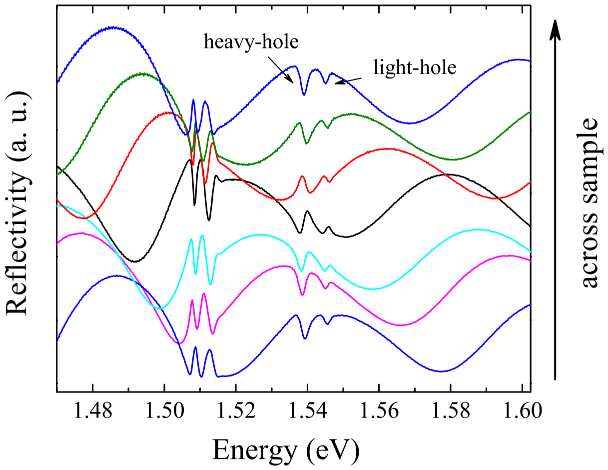

Figure 3.4: Measured reflectivity spectra across the sample surface. The heavy-hole and light-hole exciton resonances are denoted in the figure. Spectra are offset vertically for clarity.

multilayer structure of the sample requires considerations of the multiple interfaces and interference effects within the sample, as well as different absorptions associated with different layers. We use a matrix method to treat the problem by which the amplitudes and phases of the electromagnetic field to the left of the multilayer are transformed to those to the right [35, 36]. The characteristic matrix for each layer is obtained from the optical constants and layer thickness, and the characteristic matrix of the whole medium is the product of those for each layer. The reflectivity and transmission are then easily calculated.

For a homogeneous dielectric film situated between air and substrate, the incident electric field is related to the transmitted electric field by

$$\begin{pmatrix} E_{0t}^{b} \\ E_{0t}^{f} \end{pmatrix} = \frac{1}{2u_0} \begin{pmatrix} u_0 & -1 \\ u_0 & 1 \end{pmatrix} \mathbf{M} \begin{pmatrix} 1 \\ u_2 \end{pmatrix} E_{2t}^{f}, \tag{3.2}$$

with the characteristic matrix

$$\mathbf{M} \equiv \begin{pmatrix} m_{11} & m_{12} \\ m_{21} & m_{22} \end{pmatrix} = \begin{pmatrix} \cos\delta_1 & \frac{i}{u_1}\sin\delta_1 \\ iu_1\sin\delta_1 & \cos\delta_1 \end{pmatrix}. \tag{3.3}$$

Here the superscripts f and b refer to fields propagating forward and backward, respectively, the subscript t refers to the tangential field, and the subscripts 0, 1 and 2 refer to air, dielectric film and substrate, respectively. The change of phase after the field propagating one-way in the dielectric layer is

$$\delta_1 = \frac{2\pi}{\lambda} n_1 d_1 \cos\theta_1, \tag{3.4}$$

where λ is the wavelength, n_1, d_1 and θ_1 are the index of refraction, thickness and angle of refraction of the dielectric layer, respectively. The tangential admittance u_j follows

$$u_j = \sqrt{\frac{\epsilon_j}{\mu_j}} \cos\theta_j \tag{3.5}$$

for a TE wave, and

$$u_j = \sqrt{\frac{\epsilon_j}{\mu_j}} \frac{1}{\cos\theta_j} \tag{3.6}$$

for a TM wave. From Equation 3.2 and 3.3 we obtain the reflection and transmission coefficients of the film

$$r = \frac{E_{0t}^b}{E_{0t}^f} = \frac{u_0(m_{11} + m_{12}u_2) - (m_{21} + m_{22}u_2)}{u_0(m_{11} + m_{12}u_2) + (m_{21} + m_{22}u_2)}, \tag{3.7}$$

$$t = \frac{E_{2t}^f}{E_{0t}^f} = \frac{2u_0}{u_0(m_{11} + m_{12}u_2) + (m_{21} + m_{22}u_2)}. \tag{3.8}$$

The reflectivity and transmission in terms of r and t are

$$R = |r|^2, \qquad T = \frac{u_2}{u_0} |t|^2. \tag{3.9}$$

The above formula can be generalized to the case of a succession of stratified media by using a characteristic matrix

$$\mathbf{M} = \mathbf{M_1 M_2} \ldots \mathbf{M_N} \tag{3.10}$$

for an N–layer structure.

3.3.3 Linear spectra: calculation

We calculate numerically the linear spectra of the sample by using the above characteristic matrix method, based on the nominal sample structure and assuming Lorentzian lineshapes for both the heavy-hole and light-hole exciton resonances. There are some important aspects of this calculation that are worth mentioning:

(1) The sample is assumed homogeneous with interfaces parallel and optically flat.

(2) The absorption of the layers are included in the calculation by using complex indices of refraction ($\tilde{n}$) in Equation 3.4–3.6.

(3) Both the heavy-hole and light-hole exciton resonances are included in the calculation for the GaAs quantum wells, with the complex index of refraction of the quantum well layers following that of an oscillator model (Equation 3.1).

(4) The interband transition of bulk GaAs (whose bandgap energy is ∼30meV below that of the excitons in the quantum well) is also considered in the calculation for thick GaAs layers. The changes of the index of refraction and absorption associated with the transition is accounted for by using the Elliott formula [37].

(5) The background indices of refraction used in the calculation for different layers are obtained from Reference [38], with $n_b = 3.656$, 3.42, 3.36 and 1.77 for GaAs, $Al_{0.3}Ga_{0.7}As$, $Al_{0.4}Ga_{0.6}As$ and sapphire, respectively.

(6) Both the linear and Faraday (Kerr) spectra are experimentally measured under normal incident light. We therefore set $\theta = 0$ in Equation 3.4–3.6.

(7) The reflectivity and transmission coefficients obtained from Equation 3.7 and 3.8 not only give information of the amplitudes, but also the phases. The Faraday and Kerr rotation are related to the phase changes of the transmitted and reflected beams, respectively. We therefore calculate both the amplitudes and phases of the reflectivity and transmission spectra.

The calculated transmission (not shown) and reflectivity spectra (solid lines in Figure 3.5) are very similar to the measurements. The reflectivity spectrum shown in Figure 3.5(a) has an absorption dip lineshape for the heavy-hole exciton resonance. This is because the sample thickness allows for constructive interference at the heavy-hole exciton wavelength. As the thickness changes, the heavy-hole exciton resonance appears as a dispersive lineshape, as shown in Figure 3.5(b), which corresponds to a sample thickness roughly 1/8 of a wavelength different from that in Figure 3.5(a). We note that the multiple internal interfaces play a minor role in the spectra due to the similar indices of refraction of the GaAs and $\mathrm{Al_xGa_{1-x}As}$ layers. We extract the linear optical parameters such as resonance energies, linewidths and oscillator strengths of the heavy-hole and light-hole exciton transitions from comparison of the calculated and measured spectra, which will be used for the analysis of the Faraday (Kerr) spectra in the next section.

3.4 Faraday and Kerr spectra

We measure the Faraday (Kerr) rotation and ellipticity spectra by scanning the incident pump and probe pulse wavelength (degenerate) in 0.5 nm steps. The observed Faraday (Kerr) signal for each wavelength oscillates in time after excitation, due to the Larmor precession of carrier spins about the applied magnetic field. A Fourier transform of the transient reveals multiple precession frequen-

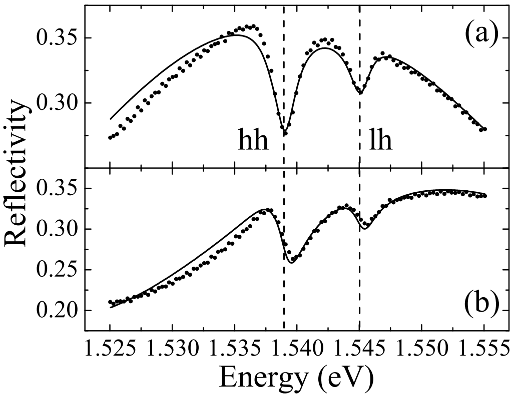

Figure 3.5: Measured (dots) and calculated (solid lines) linear reflectivity spectra near heavy-hole (hh) and light-hole (lh) exciton resonances (indicated by dashed lines). Spectra in (a) and (b) correspond to different sample thicknesses, which are described in the text.

cies, which originate from different Landé g factors for different carrier types. By selecting the single Fourier peak due to the electron spin precession in the quantum well, irrelevant contributions such as Faraday (Kerr) signals from the bulk GaAs layer, coherence effects from the cross-correlation between pump and probe pulses, and DC signals due to scattered pump light into the detecting system are all eliminated. The Faraday and Kerr spectra are then obtained by plotting the amplitude of the Fourier peak as a function of photon energy, as shown in Figure 3.6(a)–(d) (circles). The spectra are measured at the same sample thickness as that in Figure 3.5(a). One sees similar spectral shapes for the Faraday and Kerr rotation (ellipticity), in contrast to the prediction for a simple absorbing slab, i.e. a Kramers–Kronig relation, which is shown in Figure 3.2(b). The Faraday and Kerr spectra are also measured at a different sample thickness [same thickness as that in Figure 3.5(b)], which is plotted in Figure 3.6(e)–(h) as circles. While the Faraday effects show similar spectral profiles regardless of the sample thickness, there is a clear change of Kerr spectra as the sample thickness is changed by a fraction of a wavelength. Note that for this sample thickness, the Kerr and Faraday spectra do approximately obey a Kramers–Kronig relation.

We calculate Faraday (Kerr) spectra based on the calculated transmission (reflectivity) spectra in the last section. Without any loss of generality, we assume a σ^+ circular polarization of the incident pump pulse, which preferentially excites spin $-\frac{1}{2}$ electrons in the quantum well. The optical constants for σ^+ helicity are varied as a result of the nonlinearity created by spin $-\frac{1}{2}$ electrons, with the nonlinearity described by small changes of exciton resonance energies, linewidths and oscillator strengths. The change of the linear spectra for σ^+ helicity is then calculated following the method described in the last section. The optical constants and linear spectra for σ^- helicity are assumed to be unchanged after optical excitation, because of the absence of spin $+\frac{1}{2}$ electrons. The Faraday (Kerr) *ellipticity* spectra are calculated by subtracting the transmission (reflectivity) spectra for σ^- helicity from those for σ^+ helicity. The Faraday (Kerr) *rotation* spectra are obtained as the product of transmission (reflectivity) spectra with the difference of the phase of transmission (reflectivity) spectra between σ^+ and σ^- helicities. The nonlinear parameters are varied to obtain good agreement between the calculated and measured *Faraday ellipticity* spectra alone [Figure 3.6(b)]. We then use the same nonlinear parameters to calculate the rest of the spectra, and the results are shown in Figure 3.6 as solid lines. The only difference in the calculation between Figure 3.6(a)–(d) and (e)–(h) is the use of different sample thickness. To represent the experimental condition of finite bandwidths of both pump and probe pulses, averaging of the exciton excitation with the pump spectrum, and averaging of the Faraday (Kerr) signal with the probe spectrum are included in the calculation. Good agreement is found between theory and experiment. We note that the theoretical lineshapes reproduce the lack of a Kramers–Kronig relation found in the

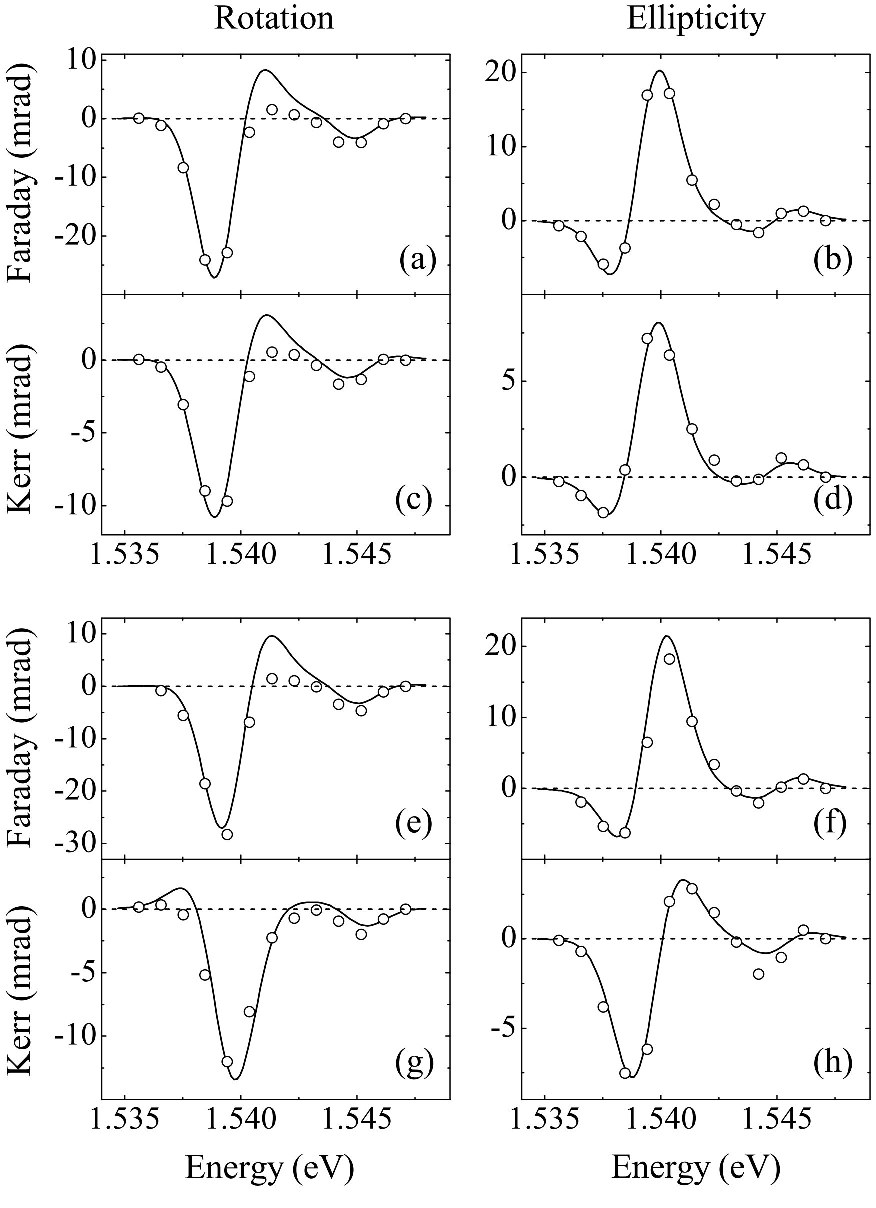

Figure 3.6: Measured (circles) and calculated (solid lines) Faraday and Kerr effect spectra. Spectra in (a)–(d) are obtained for a sample thickness the same as that in Figure 3.5(a), while spectra in (e)–(h) are for a slightly different sample thickness, same as that in Figure 3.5(b).

experiment.

Because of the different spectra for different nonlinear contributions [39], as illustrated in Figure 3.1, one can distinguish among them by the shape of the Faraday (Kerr) spectrum. We deduce from the comparison between calculations and measurements a reduction of the heavy-hole exciton transition strength of 1.7% and an increase of its damping by 5.3% after excitation. We also obtain a decrease (red shift) of the heavy-hole exciton resonance energy by 0.11 meV. The extraction of parameters is, however, not the goal of this work. Detailed extraction of the nonlinear parameters requires full knowledge of the sample structure, which is not available with sufficient precision. Rather, we want to show the ambiguities in interpreting the Kerr effect spectra, which have been ignored in most experiments that use Kerr effect.

For the quantum well sample we studied, the spectral profiles of the exciton resonances in the reflectivity spectra are dominated by the interference effect from the total sample thickness, which gives a dip (peak) lineshape for constructive (destructive) interference and a dispersive lineshape otherwise. The reflectivity spectrum for a multilayer structure is in general different from that for a single interface, which is a result of multiple interfaces within the sample and interference effect from finite sample thickness. As a consequence, the Kerr effect spectra should also differ from what is expected for a single interface. Kerr spectra of semiconductor heterostructures depend not only on the nature of the optical nonlinearities, but also on linear optical effects such as the interference from layer structures. Failure to take this into account may lead to ambiguities in the extracted nonlinearities from the Kerr effect and in distinguishing signals from different species. One therefore needs to have complete information of the sample structures and reflectivity spectra for a correct interpretation of the observed Kerr spectra.

The Faraday (Kerr) effect is measured by using degenerate pump and probe pulses with narrow linewidth. In Chapter 4, a two color experiment is performed with the pump and probe pulses spectrally filtered individually to enable independent tuning of their photon energies and spectral linewidths. By using non-degenerate pump and probe pulses, different effects from excitation and detection can be separated, which is not possible with the current degenerate setup.

Chapter 4

Interaction induced spin polarization in a 2DEG

In Section 2.4, the spin dynamics in bulk GaAs samples with different doping densities have been studied. For future spintronic devices and quantum information processing, certain applications perform better in quantum confinement systems, such as quantum wells and quantum dots. In this chapter and the next chapter, we will focus our study on the spin dynamics in quantum wells. The distinction of the spin dynamics in quantum wells from that of the bulk arises from several aspects due to the well structure: the subband electronic structures, the enhancement of excitonic interactions, and the high mobility of the carriers. An example is the slow-down of the valence band hole spin relaxation in the quantum well compared with the bulk, due to the lifting of the degeneracy between the heavy-hole and light-hole valence bands in quantum wells.

Long spin relaxation times of the carriers are essential to applications in spintronic devices and quantum information processing, and have been measured in lightly n-doped semiconductor quantum wells [9]. These spin relaxation times are measured by exciting and probing optical transitions. In those systems, the interband optical properties are dominated by excitons and negatively charged excitons (trions) at low temperatures, but the electron spin can persist long after recombination of optically excited carriers. Coherent optical generation and manipulation of the electron spins require an understanding of how optical excitation initiates and controls the electron spin polarization. The purpose of this work is to provide a full physical picture of how light pulses polarize the spin of the electron gas in weakly doped quantum wells.

We use a two-color transient Kerr rotation technique to study a lightly n-doped CdTe quantum well, through which different effects from excitation and detection can be well separated [40]. We show that the spin of the two-dimensional electron gas (2DEG) can be polarized instantaneously after resonant excitation of spin polarized trions. Under resonant generation of excitons, the 2DEG can also be spin-polarized through the formation of trions via exciton states. The exciton spin polarization is transferred to the electron gas coherently, with the spin coherence partially lost through exciton spin relaxation. To characterize the spin polarization process of the electron gas, the interplay between the exciton, trion and 2DEG spins and their individual spin relaxation need to be taken into account. The observed transient Kerr rotation signals are quantitatively explained with rate equations involving the spin populations of exciton, trion and the electron gas. Trion spin relaxation also reveals information on the hole spin flip process, giving the excitation energy dependence of the hole spin relaxation [41].

We also examine the spin coherence of a 2DEG at different density in a set of modulation-doped CdTe/$\mathrm{Cd_{0.85}Mg_{0.15}Te}$ quantum wells with different doping densities. The spin dephasing times T_2^* of the 2DEG are measured as a function of the applied magnetic field, and the dephasing times in the limit of zero magnetic field are obtained. The spin dephasing time as a function of the electron gas density from 5×10^9 to 2.4×10^{11} cm^{-2} shows a non-monotonic behavior with a maximum at 8×10^{10} cm^{-2} [42, 43].

4.1 Exciton and trion spin dynamics

4.1.1 Exciton spin dynamics

Exciton spin dynamics have been addressed mostly in undoped quantum wells. The exciton spin can relax via simultaneous spin flips of the electron and hole in an exciton, i.e. exciton spin flip as a whole [44, 45]. This mechanism has been recognized as the relevant depolarizing mechanism of excitons under zero applied magnetic fields. The hole in an exciton undergoes fast spin relaxation due to strong mixing of the heavy- and light-hole valence band. A combination of the exchange interaction between the electron and the hole and the hole spin flip itself is responsible for the spin flip of the exciton from +1 to -1 and vice versa.

The electron and hole in an exciton behave quite differently under an in-plane external magnetic field (Voigt geometry). In quantum wells, the heavy-hole spins are constrained to lie normal to the quantum well plane by the effects of quantum confinements, and are not observed to precess under moderate magnetic fields due to the vanishing Zeeman splitting in the transverse fields [30]. On the other hand, the electron spin does undergo Larmor precession about the magnetic field axis. Assuming a long hole spin flip time in the exciton, this results in an oscillation between the bright and dark exciton populations [46], and a modified spin precession frequency due to the electron-hole exchange interaction [47, 48]. The manifestation of exciton spin precession under the electron-hole exchange interaction relies on the stability of the hole-spin orientation within an exciton. Besides the individual spin relaxation of the electron and hole in an exciton, the exciton spin flip as a whole still plays a role in its spin dynamics under a magnetic field.

In lightly n-doped quantum wells, the interband optical properties are still dominated by excitonic transitions at low temperatures. Little work has been done on the interactions between the spin polarization of excitons and that of the electron gas in lightly *n*-doped quantum wells [49], despite the importance of exciton transition on optical orientation of the electron gas.

4.1.2 Trion spin dynamics

A negatively charged exciton, a trion, was first observed in a CdTe quantum well [50]. It is formed by two electrons bound to one hole, analogous to a negatively charged hydrogen ion (H^-) in vacuum. Trions play an important role in the optical spectra of moderately doped quantum wells [51, 52]. II-VI semiconductor quantum wells (such as the CdTe quantum wells used in this work) are an adequate choice for the study of trions, because the Coulomb interaction in II-VI semiconductors is typically twice that in III-V compounds, and because the trion binding energy is expected to be an order of magnitude larger than that in bulk materials due to the quantum confinement.

The unique signature of a trion in spin dynamics is that it can only contribute to the spin dynamics by its hole spin, because a trion in its singlet state consists of a hole and two electrons with opposite spins. However, upon optical excitation of spin-polarized trions, electrons of a certain spin polarization are removed from the 2DEG to form trions, polarizing the 2DEG with an opposite spin. The spin orientation of the electron gas from resonant trion excitation has been previously reported [53, 54], with the 2DEG instantaneously polarized during the trion excitation. Trion recombination at a later time will release a spin polarized electron to the 2DEG, with the coherent spin polarization of the electron gas modified depending on the trion recombination time, trion spin relaxation time and the magnetic field applied [55].

4.2 Sample characteristics and experiments

The samples are modulation doped CdTe/$Cd_{0.85}Mg_{0.15}Te$ heterostructure grown by molecular beam epitaxy on a (100) GaAs substrate with a 2 μm CdTe buffer layer. The samples contain two CdTe quantum wells with widths of 120 and 70 Å, separated by a 50 Å $Cd_{0.85}Mg_{0.15}Te$ barrier. The 120 Å well is one-side doped by an iodine impurity layer 100 Å from the well. By choosing different thicknesses of the iodine layer, four samples are grown with 2DEG densities of 5×10^9 (nominally undoped), 8×10^{10}, 1.6×10^{11} and 2.4×10^{11} cm^{-2} in the 120 Å well. The 70 Å quantum well remains undoped. All samples are grown on the same wafer by the wedge doping technique to guarantee a consistent sample set [56]. We study the 120 Å quantum well only. First we will focus on the lightly doped sample ($n_e = 8 \times 10^{10}$ cm^{-2}) for the study of spin interactions between excitons, trions and the 2DEG. In Section 4.6, the electron spin coherence for all four samples will be discussed.

The low temperature photoluminescence (PL) and photoluminescence excitation (PLE) spectra for the lightly doped quantum well ($n_e = 8 \times 10^{10}$ cm^{-2}) are shown in Figure 4.1. The spectra exhibit exciton and trion lines with an energy separation of 2.6 meV, which is the trion binding energy. There is a small Stokes shift (~0.5 meV) between the trion peaks in the PL and PLE spectra. The large trion binding energy (as compared with III-V semiconductors) and the relatively narrow linewidths of the resonances allow us to selectively generate excitons and trions by means of optical excitation. The PLE spectrum shows that the peak exciton absorption strength is about twice that of the trion. The PL spectrum, however, is dominated by trion recombination. This indicates that the majority of the optically created carriers relax to the trion states. Under resonant excitation of excitons, the conversion of excitons to trions is much faster than the exciton

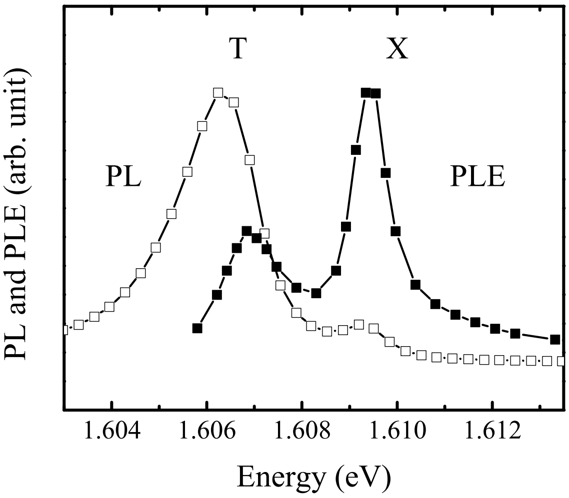

Figure 4.1: Low temperature PL and PLE spectra for the lightly n-doped CdTe quantum well ($n_e = 8 \times 10^{10}$ cm^{-2}), showing the exciton (X) and trion (T) lines.

recombination.

We measure the transient Kerr rotation with an applied magnetic field of 2 T applied normal to the quantum well growth direction (Voigt geometry) [30]. Pump and probe pulses are spectrally filtered (resulting in ~5 ps pulses) to enable independent tuning of their photon energies. The spectral linewidths of the pulses are adjusted to be ~0.2 nm for spectrally resolved measurements. By performing two-color measurements, not only can we selectively excite different populations, but we are also able to compare experimental results under different excitation energies with a fixed probe energy. The pump and probe photon energies are scanned near the vicinity of the exciton and trion resonances of the 120 Å quantum well. Average intensity in the pump is about 1 W/cm^2 (except as specified otherwise in the text) and 0.1 W/cm^2 in the probe beam. The pump (probe) beam is focused onto the sample with a spot diameter of ~ 100 μm (50 μm). All experiments are performed at 4 K.

4.3 Spin dynamics of excitons, trions and 2DEG: experiments

In this section, we spectrally study the spin dynamics in the lightly n-doped CdTe quantum well ($n_e = 8 \times 10^{10}$ cm^{-2}). Transient Kerr rotation signals under transverse magnetic field for resonant excitations of excitons and trions are shown in Figure 4.2(a). The probe photon energy is tuned at the exciton resonance (1.6093 eV) for both pump energies. The oscillation signals correspond to the Larmor precession of carrier spins in an external magnetic field. A precession frequency of 43.3 GHz is measured, corresponding to a Landé g factor of $|g| = 1.55$. The Kerr rotation signal under exciton generation exhibits two exponential decays of the oscillation with very different time constants. A non-oscillating decay component in addition to the double exponential is observed under trion excitation. We perform a least-square fit to the transient signals with the form $\theta_K(t) = (A_1 e^{-t/\tau_1} + A_2 e^{-t/\tau_2})\cos(\omega_L t)$, where ω_L is the Larmor precession frequency, τ_1 and τ_2 (A_1 and A_2) are the long and short spin dephasing times (precession amplitudes), respectively. A third term of $A_3 e^{-t/\tau_3}$ is included in the fit to account for the non-oscillating decay under trion excitation. The time constants retrieved from the fit are also displayed in Figure 4.2(a). Both signals show a long-lived oscillation component that lasts over 1 ns. As this time constant exceeds lifetimes of excitons and trions (measured to be < 100 ps by a streak camera [52]), we conclude that this is the spin Larmor precession of the 2DEG. The short time constants should be related to the exciton and trion spin dynamics, which will be discussed later.

To study how the probe photon energy affects the transient Kerr signal, we scan the probe energy with the pump photon energy fixed on either the exciton or trion resonance. The Kerr rotation amplitude of the 2DEG spin polarization (A_1) is plotted in Figure 4.2(b) as a function of probe energy. The similarity

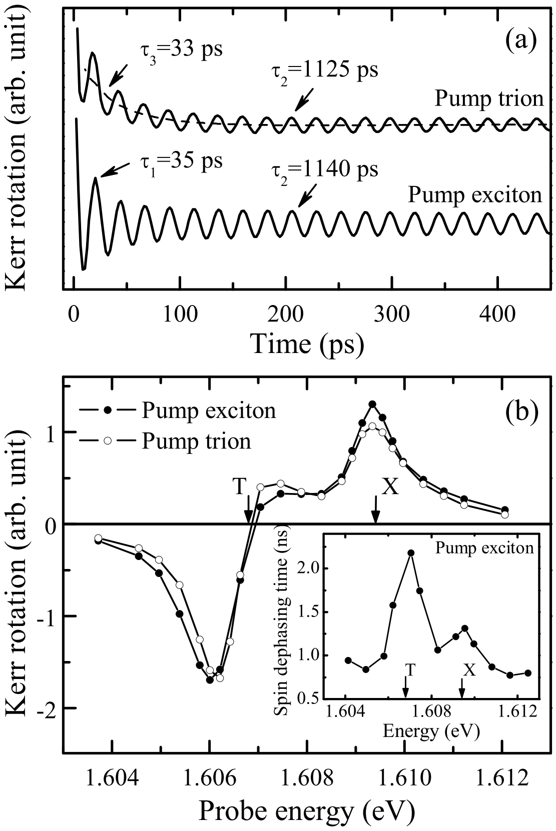

Figure 4.2: (a) Transient Kerr rotation signals under resonant excitations of excitons and trions, with probe photon energy at the exciton resonance. The time constants shown are obtained from nonlinear fitting. (b) The Kerr rotation amplitude of the 2DEG spin polarization (A_1) as a function of probe photon energy under resonant excitations of excitons (X) and trions (T). Inset: probe energy spectrum of the electron spin dephasing time (τ_1), under resonant exciton generation. $B = 2$ T and $T = 4$ K.

of the probe spectra obtained with exciton and trion excitation confirms spin polarization of the electron gas for both excitation conditions. The spectra also indicate a difference in response sensitivity between detection through exciton and trion resonances (given that the carrier density generated at exciton resonance is twice that at trion resonance). The remaining experiments in this chapter will be performed with the probe energy fixed, so that a comparison of amplitudes resulting from different excitation energy is possible. The spectra in Figure 4.2(b) show a peak shape for the exciton resonance and a mixture of dispersive and peak lineshape for the trion resonance. The different lineshapes of the resonances result from different nonlinear responses of excitons and trions from spin-polarized electrons [33]. This is supported by a recent work on CdTe-based quantum wells [57], where the spin-polarized electron gas is shown to effectively screen excitons, but not trions. In the inset of Figure 4.2(b), the electron spin dephasing time (τ_1) is measured as a function of the probe photon energy, with the pump energy on the exciton resonance (similar probe spectrum is observed for resonant trion generation, not shown). The electron spin dephasing time obtained by probing the trion resonance is almost two times longer than that by probing the exciton resonance. The observed results may be related to the inhomogeneous distribution of the electrons, while the trion resonance is more sensitive for detecting the localized electrons [58], and the exciton resonance for detecting weakly localized electrons. The weakly localized electrons may experience different spin relaxation mechanism than the localized ones, resulting in a shorter spin dephasing time. A similar behavior has been recently reported [40].

To further explore the short time behavior in the transient Kerr rotation signals and the origins of the electron gas spin polarization through optical excitation, we study the Kerr rotation spectrum with varying pump photon energy. Specifically, we selectively generate exciton and trion populations, while the probe photon energy remains fixed at the exciton resonance (1.6093 eV). The spectral data are again analyzed by least-square fit to a double exponential, and we plot the Kerr rotation amplitude for the slow (A_1) and fast decay components (A_2) as a function of pump energy, as shown in Figure 4.3(a). The amplitude of the fast decay component exhibits a sharp peak at the exciton energy, with a FWHM linewidth (0.7 meV) agrees well with the exciton linewidth in the PLE spectrum (0.8 meV). We assign the fast oscillation decay to exciton spin precession and dephasing. The decay time (τ_2) is a combination of the exciton spin dephasing time and trion formation time. The relatively weak signal of A_2 near the trion energy is probably related to the ionization of trions into excitons, as the trion itself cannot contribute to the oscillatory signal. The amplitude of the slow decay component, which is proportional to the 2DEG spin polarization, is enhanced at both exciton and trion resonances. This enhancement indicates spin polarization of the electron gas through optical excitation of excitons. We propose that excitons polarize the spin of the 2DEG through their conversion to trions, which preserves the spin orientation, and polarizes the 2DEG. The spin-flip scattering of excitons by single electrons, for instance, could also polarize the 2DEG. However, since the majority of the optically excited excitons relax to the trion states (evidenced in the PL spectrum), we believe the trion formation process dominates.

We obtain further information on the exciton and electron gas spin polarization by varying the pump excitation intensity. In Figure 4.3(b), the excitation intensity dependence of the Kerr rotation amplitudes is shown for resonant excitation at excitons and trions. The fast decay amplitude (A_2) for resonant excitation at the exciton, related to the exciton spin polarization, increases monotonically with intensity, and can be well fitted with a saturation function $P_1 I/(P_2+I)$, with P_1, P_2 constants and I the intensity. The electron gas spin polarization (A_1), on the other hand, actually decreases at high intensity for excitation at both exciton and trion resonances. The absorption strength at the trion energy is about one half of that at the exciton energy. With this correction [by using different scales of excitation intensity for the exciton and trion in Figure 4.3(b)], we observe very similar intensity dependence of the 2DEG spin polarization for resonant excitation of excitons and trions. By exciting trions directly, the electron spin polarization is

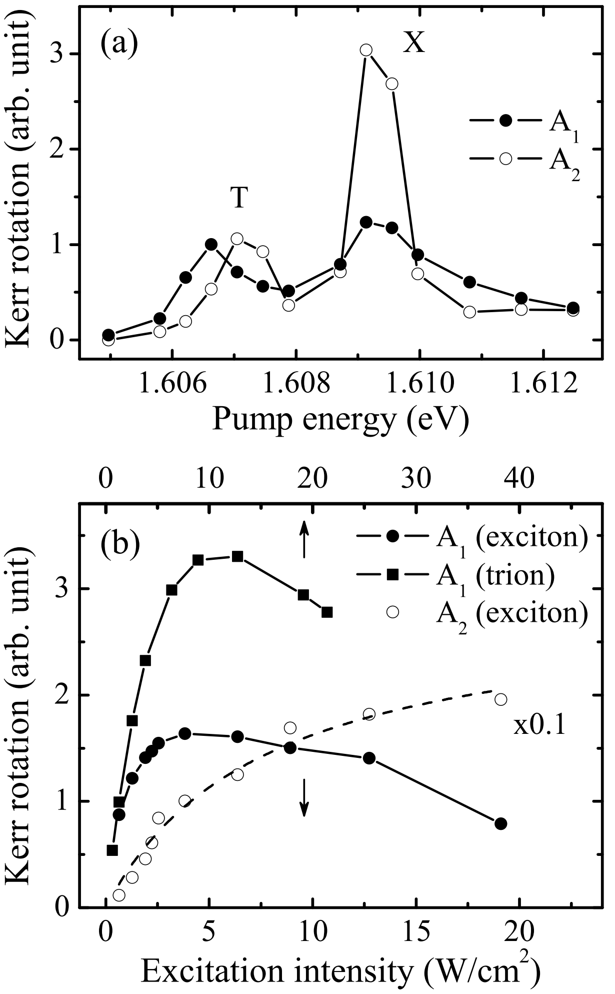

Figure 4.3: (a) Kerr rotation amplitudes as a function of pump photon energy for the slow (A_1) and fast decay components (A_2). (b) Excitation intensity dependence of the Kerr rotation amplitudes (A_1 and A_2) under resonant excitation at excitons and trions, with A_2 scaled by 0.1 for clarity. The amplitude A_2 for resonant exciton generation is fitted with a saturation function (dash line). $B = 2$ T and $T = 4$ K. Probe energy is tuned at exciton resonance.

about twice that from exciton generation [as indicated by the peak A_1 amplitudes in Figure 4.3(b) for the exciton and trion]. We will show later that this is due to a similar trion formation time and exciton spin dephasing time, and spin coherence is partially lost before an exciton forms a trion.

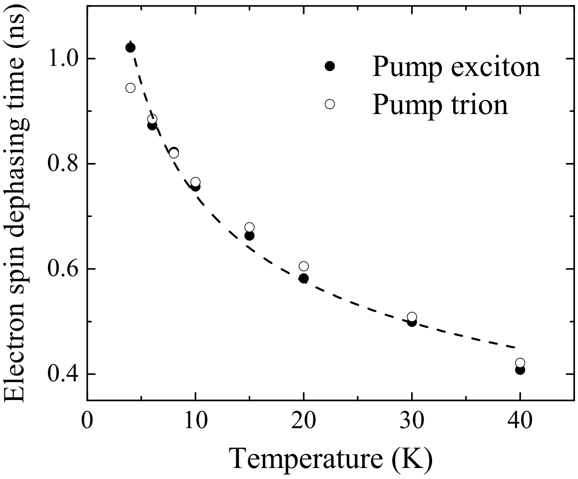

Figure 4.4: Electron spin dephasing time (τ_1) as a function of temperature, with τ_1 measured under resonant excitation of excitons and trions. The dash line ($\tau_1 \propto T^{-0.4}$) is a nonlinear fit to the data under exciton generation. $B = 2$ T.

We measure the temperature dependence of the Kerr rotation signal by pumping at the exciton and trion resonances (with probe energy fixed at the exciton resonance). We do not observe significant temperature dependence of the exciton dephasing time (τ_2) up to 40 K. The electron spin dephasing time (τ_1), however, decreases rapidly with increasing temperature, which is shown in Figure 4.4. The τ_1 measured under resonant excitation of both excitons and trions are plotted in Figure 4.4, and close values under both excitation conditions are obtained. A least-square fit of the data under exciton generation yields a temperature dependence $\tau_1 \propto T^{-0.4}$. It was suggested that both the D'yakonov-Perel' and Elliott-Yafet spin relaxation mechanisms (discussed in detail in the last chapter) are expected to give a decreased electron spin relaxation time with increasing temperature in quantum wells [59]. Due to a lack of a comprehensive theory on temperature dependent spin relaxation in quantum wells, we are unable to distinguish the two mechanisms in our sample.

In Figure 4.2(a), a non-oscillating component at short time delay is observed for trion excitation, with a decay time of $\tau_3 = 33$ ps. The trion only contributes to the spin dynamics through its hole spin, because of the two opposite electron spins in a trion. The non-oscillating component observed in the transient Kerr signal is therefore assigned to the hole spin flip in trions, with τ_3 the hole spin flip time [54]. We measure the hole spin flip time as a function of the pump photon energy. For this measurement, the probe photon energy is set near the trion resonance at 1.6066 eV, which gives the most sensitivity for measuring the hole spin flip. The pump energy is scanned, with its excitation intensity varied to ensure roughly equal optical carrier density (calibrated through the PLE spectrum). The resulting spectrum for the hole spin flip time is shown in Figure 4.5(a). The hole spin flip time is maximum around the trion resonance, and decreases rapidly with increasing excitation energy. Note that the hole spin flip time measured through transient Kerr rotation belongs to that in trions. For non-resonant excitation of trions, the measured time sets the upper limit of the hole spin flip time, and needs to be taken with caution. Hole states are, in general, an admixture of various spin states, and any energy or momentum relaxation process will lead to their spin relaxation [44, 49]. This explanation supports our experimental results, where a fast hole spin flip is observed for hot hole generation. We note that the hole spin flip under resonant excitation of excitons is much faster than that under excitation of trions [also illustrated in Figure 4.2(a) as a vanishing non-oscillation decay for exciton generation]. We believe the enhancement of the hole spin flip rate in excitons is due to exchange interactions between the electron-hole pairs in excitons, as detailed in Reference [45]. With the two electrons in a trion having opposite spins, the exchange interaction vanishes for the hole, giving a longer hole spin flip time for trions.

We also measure the hole spin flip time as a function of temperature and

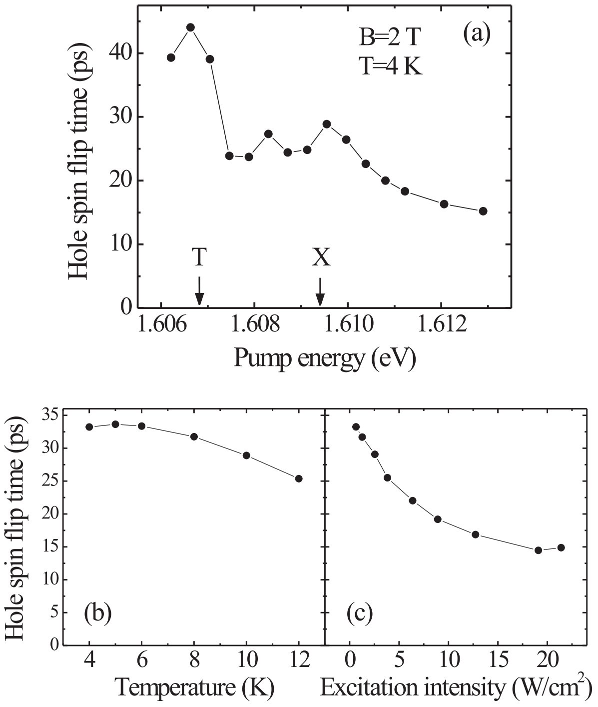

Figure 4.5: The hole spin flip time (in trions) as a function of (a) excitation energy, (b) temperature and (c) excitation intensity. $B = 2$ T.

excitation intensity, as shown in Figure 4.5(b) and (c). For those measurements, the pump photon energy is on resonance with trions, while the probe energy is set near the trion resonance (1.6066 eV). The amplitude of the non-oscillatory signal (A_3), that originated from the hole spin flip in trions, drops substantially with increasing temperature, and we are unable to retrieve information of hole spin relaxation above 12 K. The hole spin flip time does not change too much in the measured temperature range. It, however, decreases strongly with increasing excitation intensity, as shown in Figure 4.5(c). Increasing the optically injected carrier density will increase the momentum scattering rate of the carriers. We can therefore exclude the D'yakonov-Perel' spin relaxation mechanism for hole spins, which gives a spin relaxation rate that is inversely proportional to the momentum scattering rate. We believe the hole spin relaxation follows a Elliott-Yafet spin relaxation mechanism, which arises from momentum scattering during collisions with phonons or impurities.

4.4 Spin dynamics of excitons, trions and 2DEG: analysis

In this section, we theoretically study the spin dynamics in a lightly n-doped quantum well system. We derive rate equations involving the spin populations of exciton, trion and the 2DEG. The individual spin relaxation of excitons, trions and the 2DEG, as well as their spin interactions, is taken into account. The results concentrate on the spin polarization of the electron gas through optical transitions (exciton and trion states). A finite transverse magnetic field (Voigt geometry) is included to represent the experimental condition. We are able to quantitatively account for the experimental results in the last section by choosing the right parameters.

4.4.1 Trion spin dynamics

We start with the case of resonant trion excitation. We consider a system of trions and 2DEG after optical generation of trions (ionization of trions into excitons is not considered). In Figure 4.6(a), a schematic diagram reflects the interplay between trions and 2DEG. Without any loss of generality, we assume a σ^+ polarized pulse at $t = 0$ with a spin $+\frac{1}{2}$ electron will generate a spin $+\frac{3}{2}$ trion, and leave behind a spin $-\frac{1}{2}$ electron in the 2DEG:

$$h\nu_{\sigma^+} + e_{+\frac{1}{2}} \Longrightarrow T_{+\frac{3}{2}}. \tag{4.1}$$

The trion spin will not precess under the magnetic field, because of the two opposite spins of electrons inside a trion, and a negligible Zeeman splitting of the heavy-hole spins in the transverse direction. Instead, the trion spin will relax with its hole spin flip rate and decay exponentially. We write down the rate equations for the densities of spin $+\frac{3}{2}$ trion (N_+^T) and spin $-\frac{3}{2}$ trion (N_-^T):

$$\begin{aligned} \frac{dN_+^T}{dt} &= -\frac{N_+^T}{\tau_r^T} - \frac{N_+^T}{2\tau_s^T} + \frac{N_-^T}{2\tau_s^T}, \\ \frac{dN_-^T}{dt} &= -\frac{N_-^T}{\tau_r^T} - \frac{N_-^T}{2\tau_s^T} + \frac{N_+^T}{2\tau_s^T}, \end{aligned} \tag{4.2}$$

with τ_s^T the trion spin relaxation time and τ_r^T the trion recombination time. The total trion density then evolves with trion recombination as

$$N^T(t) = N_+^T(t) + N_-^T(t) = N_+^T(0)\exp(-t/\tau_r^T), \tag{4.3}$$

while the spin polarization of trions (the density difference between the spin $+\frac{3}{2}$ and $-\frac{3}{2}$ trions) evolves as

$$\Delta N^T(t) = N_+^T(t) - N_-^T(t) = N_+^T(0)\exp(-t/\tau^T). \tag{4.4}$$

Here $N_+^T(0)$ is the initial trion density after σ^+ pulse excitation. The decay rate $1/\tau^T = 1/\tau_s^T + 1/\tau_r^T$ combines the decay of ΔN^T through trion spin relaxation ($1/\tau_s^T$) and trion recombination ($1/\tau_r^T$). The non-oscillating decay component in Figure 4.2(a) corresponds to trion spin decay described in Equation 4.4, thus $\tau^T = 33$ ps.

The spin polarization of the 2DEG under trion excitation is generated through two different sources, initial polarization upon trion formation (instantaneously during pulse duration) and possible spin polarization through trion recombination (release of a spin polarized electron to the 2DEG after trion recombination). The former, as described in Equation 4.1, creates a spin $-\frac{1}{2}$ electron in the 2DEG after σ^+ pulse. The spin polarization of the 2DEG generated upon trion formation at $t = 0$ will precess around the magnetic field, with the projection in the quantum well growth direction

$$\Delta N_1^e(t) = -N_+^T(0)\cos(\omega_L t)\exp(-t/\tau_s^e). \tag{4.5}$$

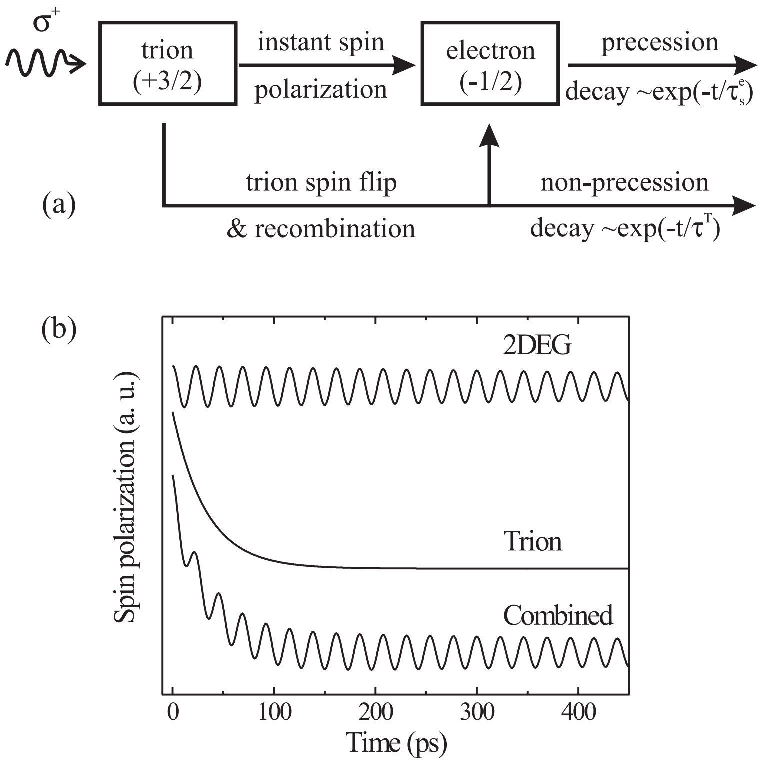

Figure 4.6: (a) A schematic diagram displaying the interplay between the spin populations of trions and 2DEG under resonant trion excitation. (b) Calculated transients of the spin polarization of the 2DEG, trions and the combination of the two.

Here τ_s^e is the electron spin dephasing time, and ω_L is the electron Larmor precession frequency. As described above, the trion recombination can also contribute to the electron gas spin polarization by returning spin polarized electrons back to the 2DEG after recombination. This is a reverse process of that shown in Equation 4.1:

$$T_{+\frac{3}{2}} \Longrightarrow h\nu_{\sigma^+} + e_{+\frac{1}{2}}. \tag{4.6}$$

This spin polarization, however, could be in phase or out of phase with that generated through trion formation, depending on whether the trion spins have relaxed and on the phase of the electron spins precessing under the magnetic field.

The 2DEG spin polarization generated by trion recombination during $[t', t' + dt']$ is

$$d\Delta N_2^e(t') = (\Delta N^T(t')/\tau_r^T)dt', \tag{4.7}$$

and the 2DEG spin polarization at t is

$$\Delta N_2^e(t) = \int_0^t (\Delta N^T(t')/\tau_r^T)\cos(\omega_L(t-t'))\exp(-(t-t')/\tau_s^e)dt'. \tag{4.8}$$

The total 2DEG spin polarization ΔN^e (including contributions from both trion formation and recombination) is

$$\Delta N^e(t) = \Delta N_1^e + \Delta N_2^e = B_1\cos(\omega_L t + \phi)\exp(-t/\tau_s^e) + B_2\exp(-t/\tau^T), \tag{4.9}$$

with

$$\begin{aligned} B_1 &= -N_+^T(0)\sqrt{1-(2-\frac{\tau^T}{\tau_r^T})\frac{\tau^T}{((\omega_L\tau^T)^2+1)\tau_r^T}}, \\ \phi &= \arctan\frac{\omega_L(\tau^T)^2}{((\omega_L\tau^T)^2+1)\tau_r^T-\tau^T}, \\ B_2 &= -N_+^T(0)\frac{\tau^T}{((\omega_L\tau^T)^2+1)\tau_r^T}. \end{aligned} \tag{4.10}$$

The results in Equations 4.9 and 4.10 are simplified by assuming a much longer electron spin dephasing time (τ_s^e) than the trion time constants (τ_s^T and τ_r^T), which is sufficient for a τ_s^e over 1 ns in our sample. The relative contribution of the trion recombination to the 2DEG spin is related to the term $\tau^T/(((\omega_L\tau^T)^2+1)\tau_r^T)$, which will only be significant when the trion spin orientation is partially maintained during its lifetime ($\tau_s^T > \tau_r^T$), and the trion time constants are much shorter than the electron precession period ($\omega_L\tau^T < 1$), so that the electron spin is not out of phase with that of the trions. In our sample, the oscillation period is 23 ps for a magnetic field of 2 T, which is comparable to the trion time constants (τ_s^T = 33 ps). The trion recombination therefore plays a negligible role in the spin dynamics of the electron gas in our sample ($\Delta N_2^e \approx 0$), and the 2DEG spin is generated mainly from trion formation ($\Delta N^e \approx \Delta N^e_1$). The total 2DEG spin polarization therefore follows that described in Equation 4.5. The spin dynamics of 2DEG, trions and the combination of the two (which corresponds to the transient Kerr rotation signal measured) are calculated and plotted in Figure 4.6(b), with $\tau^T = 33$ ps, $\tau^e_s = 1100$ ps and $\omega_L = 2\pi$ 43.3 GHz. The combined spin polarization represents well the measured transient Kerr rotation signal for trion excitation shown in Figure 4.2(a).

4.4.2 Exciton spin dynamics

The exciton spin precession and dephasing under a transverse magnetic field is illustrated in Figure 4.2(a) as the fast oscillating decay. In quantum wells, the heavy-hole spins are constrained to lie normal to the quantum well plane by effects of quantum confinements, and are not observed to precess under moderate magnetic fields [30]. The spin of the electron in an exciton does undergo Larmor precession. With a long hole spin flip time in the exciton, this results in an oscillation between the bright and dark exciton populations [46], and a modified spin precession frequency due to electron-hole exchange interaction.[1] To understand exciton spin relaxation, both the single-particle spin flips of the electrons and holes in excitons, and the exciton spin flip as a whole (simultaneous spin flip of electrons and holes) need to be taken into account. By solving the rate equations for the spin polarized electrons and holes in excitons (not shown), we obtain the density of the spin $\frac{1}{2}$ (N^X_{e+}) and spin $-\frac{1}{2}$ (N^X_{e-}) electrons in excitons as

$$\begin{aligned} N^X_{e+}(t) &= \frac{1}{2} N^X_+(0) e^{-t\left(\frac{1}{\tau^{XT}} + \frac{1}{\tau^X_r}\right)} \left(1 - \cos(\omega_L t) e^{-t\left(\frac{1}{\tau^X_{es}} + \frac{1}{\tau^X_s}\right)}\right), \\ N^X_{e-}(t) &= \frac{1}{2} N^X_+(0) e^{-t\left(\frac{1}{\tau^{XT}} + \frac{1}{\tau^X_r}\right)} \left(1 + \cos(\omega_L t) e^{-t\left(\frac{1}{\tau^X_{es}} + \frac{1}{\tau^X_s}\right)}\right), \end{aligned} \tag{4.11}$$

---

[1] We do not observe any difference of oscillation frequencies between the exciton and electron spin precession for magnetic fields ranging from 0.5 to 5.0 T. This supports the argument that the hole spin in the exciton relaxes very quickly in our sample.

and the density of the spin $\frac{3}{2}$ (N_{h+}^X) and spin $-\frac{3}{2}$ (N_{h-}^X) holes in excitons as

$$\begin{aligned} N_{h+}^X(t) &= \frac{1}{2}N_+^X(0)e^{-t\left(\frac{1}{\tau^{XT}}+\frac{1}{\tau_r^X}\right)}\left(1+e^{-t\left(\frac{1}{\tau_{hs}^X}+\frac{1}{\tau_s^X}\right)}\right), \\ N_{h-}^X(t) &= \frac{1}{2}N_+^X(0)e^{-t\left(\frac{1}{\tau^{XT}}+\frac{1}{\tau_r^X}\right)}\left(1-e^{-t\left(\frac{1}{\tau_{hs}^X}+\frac{1}{\tau_s^X}\right)}\right). \end{aligned} \tag{4.12}$$

Here $N_+^X(0)$ is the initial exciton density after σ^+ pulse excitation, τ_{es}^X (τ_{hs}^X) is the electron (hole) spin flip time in exciton, τ_s^X is the exciton spin flip time (as a whole), τ^{XT} is the trion formation time, and τ_r^X is the exciton recombination time. Both the electron and hole in an exciton lose their populations through exciton recombination and conversion of excitons into trions. They will lose their spins through exciton spin flip and their individual spin flips. The electron in an exciton will also precess in a magnetic field, but the hole will only undergo spin flip. We consider the difference between the bright and dark excitons, because the measured transient Kerr rotation signal of the exciton corresponds to the spin population of the bright excitons only. The density of the spin 1 bright excitons $N_{br+}^X \propto N_{h+}^X N_{e-}^X$ and that of the spin -1 bright excitons $N_{br-}^X \propto N_{h-}^X N_{e+}^X$. The spin polarization of the bright excitons is therefore

$$\Delta N_{br}^X(t) = \frac{1}{2}N_+^X(0)(\cos(\omega_L t)e^{-t/\tau_1^X} + e^{-t/\tau_2^X}), \tag{4.13}$$

with

$$\begin{aligned} \frac{1}{\tau_1^X} &= \frac{1}{\tau_{es}^X} + \frac{1}{\tau_s^X} + \frac{1}{\tau^{XT}} + \frac{1}{\tau_r^X}, \\ \frac{1}{\tau_2^X} &= \frac{1}{\tau_{hs}^X} + \frac{1}{\tau_s^X} + \frac{1}{\tau^{XT}} + \frac{1}{\tau_r^X}. \end{aligned} \tag{4.14}$$

We note that Equation 4.13 consists of an oscillating decay term and a non-oscillating decay term. From comparison with the experimental results [Figure 4.2(a)], we find $\tau_1^X = 35$ ps, and τ_2^X very small with no observable non-oscillation decay ($\tau_2^X < 10$ ps, half period of the oscillation). This indicates a very short hole spin flip time in our sample. Both the exciton spin flip as a whole (τ_s^X) and the electron spin flip in excitons (τ_{es}^X) are included in our model (Equations 4.14). However, they can not be separately determined based on the current experiments. We therefore treat their combined effects as an overall exciton spin dephasing time τ_s^X. Equations 4.14 may be rewritten as

$$\begin{aligned} \frac{1}{\tau_1^X} &= \frac{1}{\tau_s^X} + \frac{1}{\tau^{XT}} + \frac{1}{\tau_r^X}, \\ \frac{1}{\tau_2^X} &\sim \frac{1}{\tau_{hs}^X}. \end{aligned} \tag{4.15}$$

The calculated TKR from exciton spin dephasing is plotted in Figure 4.7(b), assuming $\tau_1^X = 35$ ps, $\tau_2^X = 0$ ps and $\omega_L = 2\pi$ 43.3 GHz.

The spin interactions between excitons and the 2DEG are proposed to be through trion formation via exciton states. The spin interplay between excitons, trions and electrons under resonant exciton excitation is displayed in Figure 4.7(a). Any time a trion is formed from an exciton that consists of a $-\frac{1}{2}$ electron, a spin polarization of $-\frac{1}{2}$ is added to the 2DEG. Both bright and dark excitons can form trions, and contribute to the 2DEG spin polarization. The hole spin orientation in the excitons does not matter in the spin polarization of the 2DEG, because it is the spin coherence of the electron in the exciton that is passed to the 2DEG. By considering the electron spin polarization in excitons, as described by Equation 4.11, the 2DEG spin polarization generated by trion formation during $[t', t' + dt']$ is determined to be

$$d\Delta N^e(t') = -(N_+^X(0)/\tau^{XT})\cos(\omega_L t')e^{-t'/\tau_1^X}dt'. \tag{4.16}$$

The $\cos(\omega_L t')$ term in Equation 4.16 indicates a coherent spin transfer from exciton to the 2DEG, i.e. the spin of the electron gas will precess in phase with the exciton spin under the magnetic field. The resulting 2DEG spin polarization at t under

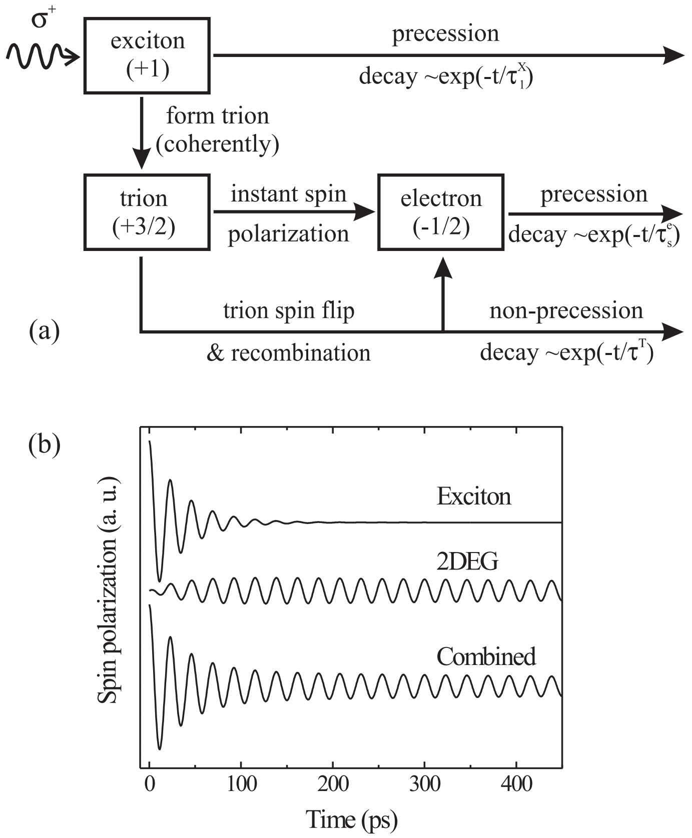

Figure 4.7: (a) A schematic diagram displaying the interplay between the spin populations of excitons, trions and 2DEG under resonant exciton excitation. (b) Calculated transients of the spin polarization of the excitons, 2DEG and the combination of the two.

resonant exciton generation is then

$$\Delta N^e(t) = (N_+^X(0)\tau_1^X/\tau^{XT})\cos(\omega_L t)(e^{-t/\tau_1^X} - e^{-t/\tau_s^e}). \tag{4.17}$$

Equation 4.17 is obtained by assuming long electron spin dephasing time (τ_s^e) and negligible electron spin polarization from trion recombination process. The 2DEG spin precession is shown to first rise due to trion formation, and then decay according to the electron spin dephasing. The calculated 2DEG spin dynamics, as well as the overall signal including the exciton spin polarization (corresponds to the experimental results) is plotted in Figure 4.7(b). The overall spin polarization agrees well the measured TKR signal shown in Figure 4.2(a).

4.4.3 Spin coherence loss via exciton spin relaxation

The 2DEG is spin-polarized through trion formation for resonant excitations of both excitons and trions. The degree of spin polarization, however, differs for the two excitation conditions. Under resonant trion excitation, a fast hole spin, or as in the case of our experiments, a high precession frequency of the electron gas, favors a complete transfer of the spin coherence to the 2DEG (discussed in detail in Section 4.4.1). An incomplete transfer of the spin coherence, however, occurs under resonant exciton generation, resulting from exciton spin dephasing. The 2DEG spin polarization under resonant excitation of trion and exciton are described in Equations 4.5 and (4.17), respectively, and the ratio between the two at long delay time is

$$\frac{N_+^T(0)}{N_+^X(0)}\frac{\tau^{XT}}{\tau_1^X} \approx \frac{N_+^T(0)}{N_+^X(0)}(1+\frac{\tau^{XT}}{\tau_s^X}), \tag{4.18}$$

under the assumption that the exciton recombination time is much longer than the trion formation time (evidenced from the small exciton recombination signal in PL spectrum). The ratio in Equation 4.18 compares the 2DEG spin polarization at a long delay time for exciton and trion excitations, which corresponds to amplitude A_1 retrieved from the experimental results. With an equal number of carriers generated initially ($N_+^T(0) = N_+^X(0)$), the 2DEG spin polarization under trion excitation is $(1 + \tau^{XT}/\tau_s^X)$ times that under the exciton generation. In Figure 4.3(b), the peak 2DEG polarization for trion generation is about 2 times that for exciton generation, which indicates similar time constants for the trion formation time and exciton spin dephasing time ($\tau^{XT} \approx \tau_s^X$). In our sample, excitons form trions at the same rate as they lose their spin coherence through exciton spin relaxation. Therefore, only half of the spin coherence is passed to the 2DEG.

4.5 Spin dynamics in highly doped sample

In the previous sections, we study the lightly doped CdTe sample ($n_e = 8 \times 10^{10}$ cm^{-2}), where the interband optical transitions are still dominated by the excitonic behaviors. In this section, we study the spin dynamics in a highly n-doped CdTe quantum well ($n_e = 2.4 \times 10^{11}$ cm^{-2}). The sample belongs to a set of samples grown on the same wafer, and its characteristics are described in Section 4.2. In Figure 4.8(a), the PL and PLE spectra of the sample is shown, with broad, asymmetric peaks replacing sharp excitonic peaks shown in the spectra for the lightly doped sample (Figure 4.1). The PLE intensity rises relatively quickly on the low energy side and falls off slowly on the high energy side, to merge into the continuum absorption. The enhancement of absorption at 1.6081 eV is identified as Fermi edge singularity, resulting from multiple scattering processes involving electrons near the Fermi energy [60]. The PL spectrum is also broadened as a result of large electron density existing in the quantum well, with the spectrum peaked near the bottom of the bandgap. In Figure 4.8(b), the Kerr rotation amplitude is measured as a function of probe photon energy under a pump excitation energy of 1.6081 eV. The amplitude is measured as the peak-to-dip amplitude of the oscillation for a pump-probe delay near 30 ps. The spectrum in Figure 4.8(b) shows a dispersive lineshape of a single resonance, centered near the energy of the peak in the PLE spectrum.

Transient Kerr rotation signal is measured by tuning the pump photon energy to 1.6075 eV and probe energy to 1.6062 eV, which is shown in Figure 4.9(a). The Kerr rotation signal again exhibits two exponential decays of the oscillation with different time constants, as measured with the lightly-doped sample. We fit transient data with a double exponential oscillation decay, $(A_1 e^{-t/\tau_1} + A_2 e^{-t/\tau_2}) \cos(\omega_L t)$, with τ_1 and τ_2 (A_1 and A_2) the long and short spin dephasing

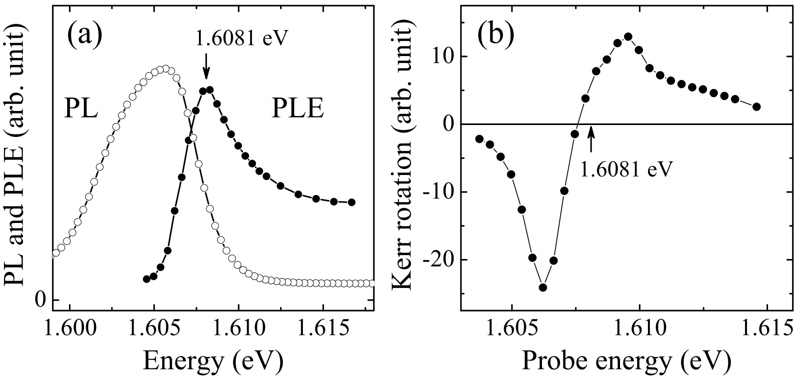

Figure 4.8: (a) Low temperature PL and PLE spectra for the highly doped CdTe quantum well ($n_e = 2.4 \times 10^{11}$ cm^{-2}). (b) The Kerr rotation amplitude as a function of probe photon energy under a pump excitation energy of 1.6081 eV. Arrows in both figures indicate the energy of the peak in the PLE spectrum.

times (precession amplitudes), respectively. The time constants retrieved from the fit are also displayed in Figure 4.9(a). It is a little surprising to observe a double exponential decay of the Kerr signal, since the excitonic transitions already disappear for this highly doped sample, and the optical properties of the sample are dominated by that of the 2DEG. A spectral study of the Kerr rotation is performed for the pump photon energy, and the amplitude spectra of A_1 and A_2 are plotted in Figure 4.9(b). The probe photon energy is fixed at 1.6062 eV for the various pump energies. Both the A_1 and A_2 spectra show a similar shape as that of the PLE spectra. This indicates that both Kerr rotation components probably originate from the 2DEG spin polarization. We propose that the observed Kerr rotation signals correspond to the spin relaxation of the 2DEG, with its spin relaxing with different rates at different stages. The short decay time (τ_2 = 71 ps) is very close to the hole lifetime measured by time-resolved PL experiments in a similar sample [52]. It is, however, well beyond the typical hole spin flip time in

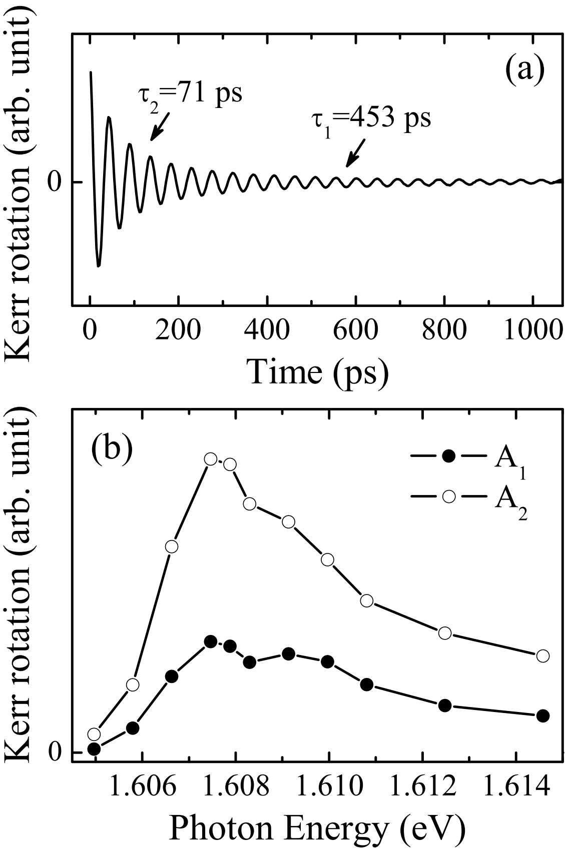

Figure 4.9: (a) Measured transient Kerr rotation signal with pump photon energy at 1.6075 eV and probe energy at 1.6062 eV. The time constants shown are obtained from nonlinear fitting. (b) The Kerr rotation amplitude of A_1 and A_2 (described in the text) as a function of pump photon energy, with probe energy at 1.6062 eV. $B = 1$ T and $T = 4$ K.

quantum wells (several ps). We therefore believe the hole recombination corresponds to the initial electronic spin relaxation observed in the Kerr rotation signal. With the presence of spin unpolarized holes, the electron-hole spin exchange interaction contributes to a faster electronic spin relaxation rate. The electron spin relaxation slows down after the recombination of the spin unpolarized holes, and a longer electronic spin relaxation time is observed ($\tau_1 = 453$ ps).

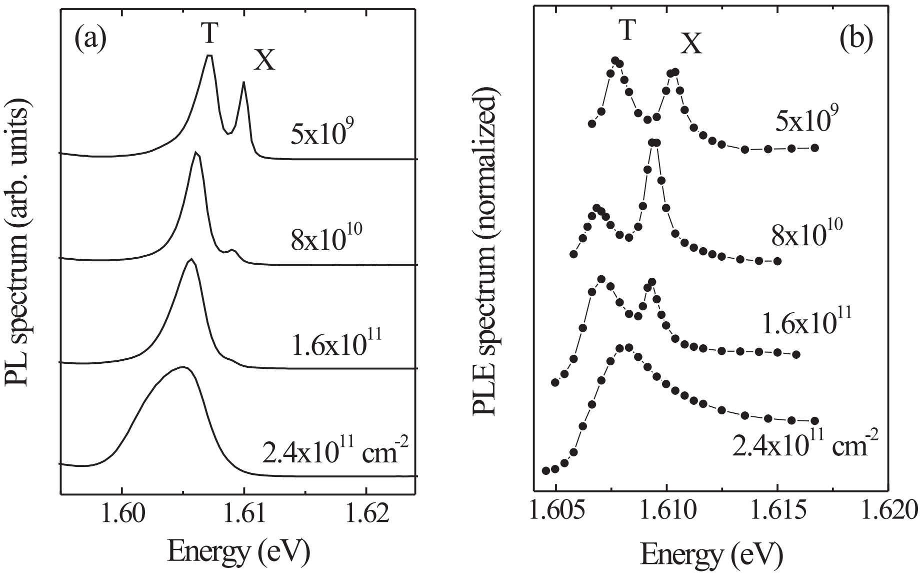

Figure 4.10: Low temperature (a) PL and (b) PLE spectra for the 120 Å CdTe quantum wells with 2DEG densities of 5×10^9, 8×10^{10}, 1.6×10^{11} and 2.4×10^{11} cm^{-2}. $T = 4$ K.

4.6 Electron spin coherence vs. 2DEG density

We study the electron spin coherence at different 2DEG density by using a set of modulation-doped CdTe/Cd$_{0.85}$Mg$_{0.15}$Te quantum wells with different doping densities (see Section 4.2 for sample characteristics). For this study, only the spin relaxation of the electron gas is concerned, with the short time spin relaxation (such as that of the excitons and trions) ignored. We measured the low temperature PL spectra [Figure 4.10(a)] of the quantum wells. For the nominally undoped sample with 5×10^9 cm^{-2} both the trion and exciton lines are clearly visible as the two peaks separated by ~ 3 meV, which is the trion binding energy. With increasing carrier density the exciton loses intensity, while the trion resonance broadens and evolves into a broad emission band with a linewidth approximately equal to the 2DEG Fermi energy [60]. Because all the quantum well samples are

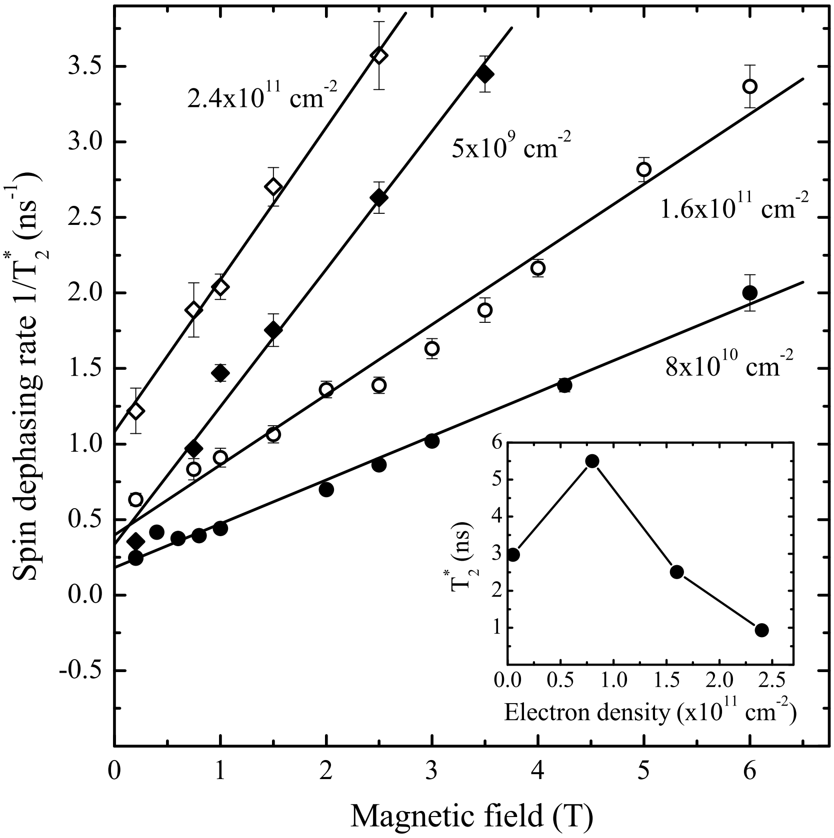

Figure 4.11: Spin dephasing rate $1/T_2^*$ as a function of the magnetic field of the 120 Å CdTe quantum wells with various electron densities. Lines are fits to Equation 4.19. Inset: Spin dephasing time T_2^* vs. 2DEG density at zero magnetic field. $T = 2$ K.

grown on thick, opaque GaAs substrate, direct absorption measurement is not possible. Instead, we measure the PLE spectra of the samples, which are shown in Figure 4.10(b). With increasing electron density, the excitonic absorption peaks (both exciton and trion) evolves into a broad, asymmetric peak, corresponding to the absorption of a 2DEG [60].

The transient Kerr rotation signals are measured by using degenerate pump and probe pulses with spectral width of 0.5 nm. The pump and probe photon energy is tuned near the bandgap of the quantum wells. A transverse magnetic field up to 6 T is applied. After the initial polarization, the spin of the 2DEG processes under the magnetic field, and decays on a nanosecond timescale. This decay time corresponds to the electron spin dephasing time, T_2^*, under a transverse magnetic field. For measuring reliable values of T_2^*, it is important to analyze the contribution to spin dephasing arising from a spread of the electron g factor, which results in an inhomogeneous dephasing of the electron spin under magnetic field. This is shown as a linear dependence of the spin relaxation rate on the magnetic field,

$$1/T_2^*(B) \approx 1/T_2^*(0) + \Delta g \mu_B B/2\hbar, \tag{4.19}$$

with μ_B the Bohr magneton, $\hbar$ the Planck's constant, and Δg a Gaussian variance of the g factor [24]. Our goal is to compare the electron spin dephasing times in the limit of zero magnetic field, $T_2^*(0)$. Figure 4.11 shows the magnetic field dependence of the electron spin dephasing rate for all four quantum wells. T_2^* values are derived by a single exponential fit to the Kerr rotation transients at delays longer than 1 ns to measure only 2DEG dynamics. The lines in Figure 4.11 are fits to Equation 4.19. These fits provide the zero field spin dephasing time, which is plotted as a function of the 2DEG density in the inset of Figure 4.11. A non-monotonic behavior with increasing electron density can clearly be seen. T_2^* first increases with electron density, then goes through a maximum of 5.5 ns at 8×10^{10} cm^{-2}, and finally decreases to 0.9 ns at high carrier densities.

Although a quantitative description of the non-monotonic behavior is not possible due to the limited numbers of the available samples (2DEG densities) (a systematic study on electron density will be presented in Chapter 5), the density dependence of the electron spin coherence can be nevertheless qualitatively understood: at low carrier densities most electrons in the quantum well are localized. In this regime the dominant spin dephasing mechanism is the hyperfine interaction with lattice nuclei spins, which generate an effective “hyperfine magnetic field” [61, 62]. The T_2^* increases as the electron becomes more delocalized. When the 2DEG density crosses the metal-insulator transition [63, 8], the spin dephasing time decreases drastically due to the D’yakonov-Perel’ mechanism [64]. Similar to bulk material [8], this overall behavior leads to an optimum doping concentration in quantum wells for achieving longest spin dephasing times.

Chapter 5

Effects of disorder on electron spin dynamics in semiconductor quantum wells

Successful implementation of spin-based electronics requires preservation of the electron spin coherence. Extending spin coherence times in semiconductors is therefore of great interest for future practical devices. In the previous chapters, a nonmonotonic dependence of the electron spin coherence time on the doping density in n-doped semiconductors has been established. A long spin coherence time is observed for either lightly n-doped bulk or lightly n-doped quantum well samples, which has also been observed in Reference [9] and [24]. It has been shown that the spin dephasing rate of the electrons is suppressed close to the metal-insulator transition [8, 63]. Below and above the critical electron density, different spin dephasing mechanisms dominate and are detrimental to spin preservation [22]. A systematic study of spin dephasing on the electron density is therefore very useful, not only for finding the maximum spin coherence time, but also for a better physical understanding of the various spin dephasing mechanisms at different carrier densities.

Samples with different doping levels can be used for this kind of study. However, particularly at low temperature, the dephasing of the carrier spin is found to vary widely between different samples [2]. One reason for this is that spin dephasing can be very sample dependent since it is strongly affected by impurities and defects. It is therefore desirable to use the *same* sample within a study. However, circumstances may prevent this, as in studies of the dependence of spin dephasing on background doping level (Section 2.4), where different wafers must be used. Even for samples grown on the same wafer (Section 4.6), complexity of spin dephasing could result from different donor concentrations. In this work, we avoid the use of multiple samples for varying carrier concentrations. Instead, a specially designed quantum well sample is used, in which the electron density in the quantum well can be optically controlled in a continuous way. We are therefore able to systematically study the spin dynamics as a function of two-dimensional electron gas (2DEG) density by using the transient Kerr rotation technique.

We vary the density in a 2DEG, and show that spin coherence is lost because of the interplay between localization by disorder and dynamical scattering. By measuring the electron Landé g factor dependence on density, we determine the density of states (DOS), which characterizes the disorder potential. Using our knowledge of the DOS, a simple model estimates the temperature and excitation intensity dependence of the g factor, qualitatively agreeing with experiments. This agreement confirms the importance of disorder and provides predictive power for designing spin-based electronic devices. We are able to compare the measured spin dephasing times to the degree of localization by concurrently probing the DOS from the electron g factor measurements. Our results show that the longest spin coherence time is obtained for weakly localized spins, which may dictate a compromise in the design of devices between increasing the spin coherence time and improving transport properties [65].

5.1 Electron Landé g factor

Electron spin dynamics probe fundamental physical processes in condensed matter systems. One example is the electron Landé g factor, which has been discussed briefly in Section 1.2.3. It is of importance in quantum transport [66] as well as being a useful test of band-theory calculations [67]. Gate-voltage-mediated control of electron coherent spin precession has also been demonstrated by utilizing materials with different g factors [68]. Under a magnetic field B, the electron spin will precess with frequency $\omega_L = g^* \mu_B B/\hbar$, where g^* is the effective Landé g factor, μ_B is the Bohr magneton and $\hbar$ is the Planck's constant. g^* in semiconductors differs from the free electron value, 2.0, due to the spin-orbit interaction, and varies with the energy in the band. The variations of the electron g factor in quantum wells from the bulk values are shown to arise mainly from the change of quantum confinement energy [69], with lesser contributions from anisotropy of the quantum well potential, carrier penetration into the barriers and strain [27]. This is confirmed by measurements of g^* for conduction electrons as a function of quantum well width [69, 27], where g^* is sampled at different energies determined by the electron confinement energy for each quantum well width. The energy dependence of the electron g factor for quantum wells has also been studied with electron spin resonance [70] and cyclotron resonance [26], and it has been found that within a small energy range the g factor can be approximated by

$$g^* = g_0 + \beta E, \tag{5.1}$$

with β a constant and E the energy. The measured g^* through transient Kerr rotation should correspond to that at the Fermi energy due to Fermi blocking.

Measurements of the electron g factor as a function of the electron density also provide information on the electron DOS. The electron DOS follows $D(E) = dn/dE$, with n the electron density. The g factor, on the other hand, satisfies $dg^*/dE = \beta$ within a small energy range (following Equation 5.1). Given a measurement of g^* as a function of electron density, the electron DOS at the

Fermi energy can therefore be determined by

$$D(n) = \beta(dg^*/dn)^{-1}, \tag{5.2}$$

with n the electron density up to the Fermi energy. In an unperturbed 2DEG, a linear dependence of g^* on the 2DEG density is expected, given that the DOS of the 2DEG is a constant as a function of energy. As will be shown later, this expectation does not agree with our experimental results, where a nonlinear dependence of g^* on the electron density is observed. We will show that the observed nonlinearity of g^* vs. density is due to the presence of the localized states, which modifies the electron gas DOS. We characterize the disorder potential by determining the DOS based on Equation 5.2. The localized states have important implications for the electron spin dynamics in quantum wells.

5.2 Sample characteristics and experiments

5.2.1 Mixed type I/type II quantum wells

The sample used for this study is an asymmetric GaAs/AlAs mixed type I/type II double-quantum-well system [71, 72]. The double quantum well structure is schematically shown in Figure 5.1(a). It consists of a wide and narrow GaAs quantum well, separated by a AlAs barrier layer. The thicknesses of these layers are specially chosen (in particular, the thickness of the narrow GaAs layer is less than 35 Å) to ensure that the lowest electronic subband in each layer forms a "staircase" [see Figure 5.1(b)]. The lowest electron state is localized at Γ in the wide GaAs quantum well, the second lowest at the X minimum in the AlAs barrier,[1] and the third at Γ in the narrow GaAs well. This arrangement necessitates the narrow quantum well being type II with respect to the barrier, while

---

[1] The bandgap of $\mathrm{Al}_x\mathrm{Ga}_{1-x}\mathrm{As}$ is indirect for $x > 0.4$, with the energy at X minimum lower than that at Γ for the conduction band.

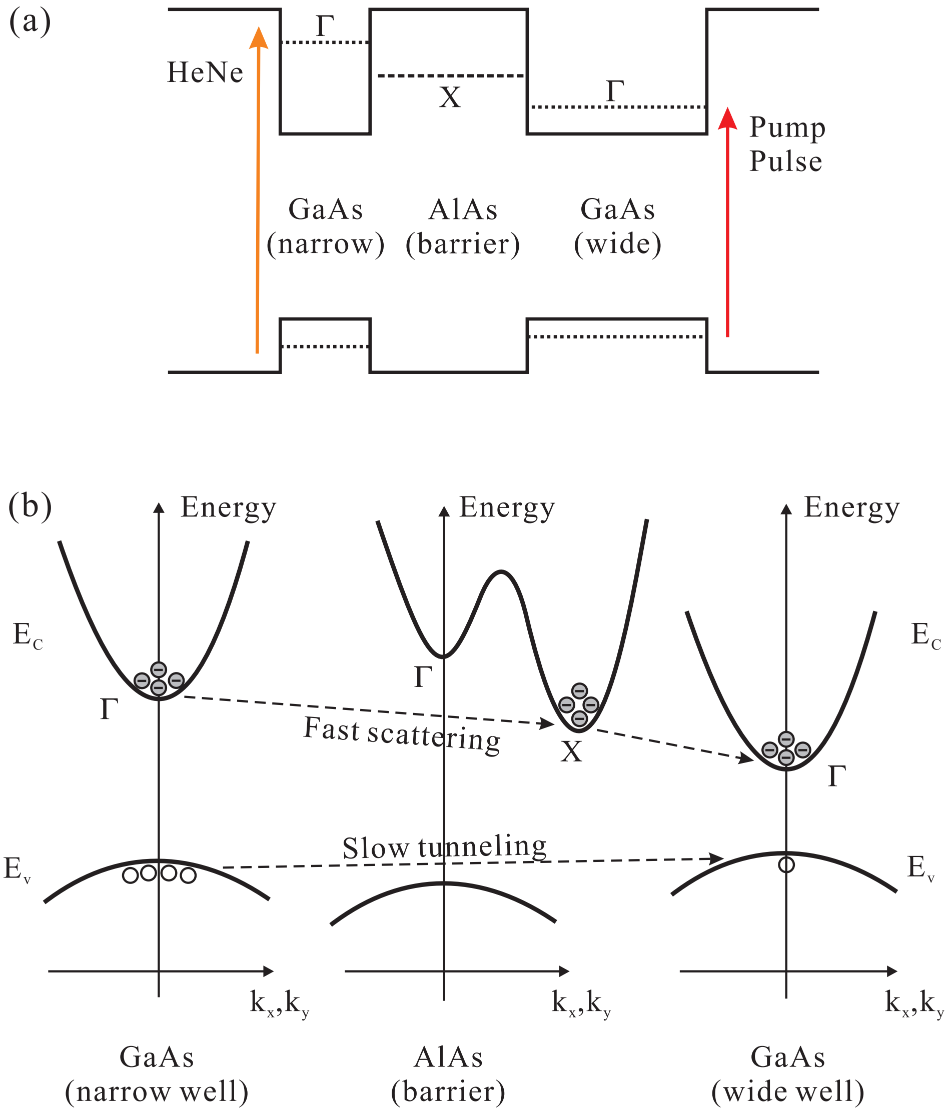

Figure 5.1: (a) Schematic diagram of the conduction and valence band edges showing the lowest confined X and Γ electron states and hole states in a mixed type I/type II quantum well. (b) Band diagram showing the conduction and valence bands (in the in-plane direction of layers, k_x and k_y) in the two quantum wells and the barrier. The limiting electron and hole relaxation mechanisms are indicated by arrows.

the wider well is type I, hence the nomenclature “mixed type I/type II” for the double quantum wells. Under photoexcitation with energy above the gap of the narrow well (HeNe excitation for our experiments), electron-hole pairs are generated in the narrow well. The electrons in the narrow well can scatter into the wide GaAs well via the AlAs X states on a picosecond time scale. On the other hand, the lowest hole states in the two quantum wells are essentially uncoupled, and holes in the narrow well can only tunnel through the AlAs barrier into the wide well (in tenth of microsecond for the sample we use) at low temperatures. We therefore have spatially separated electrons and holes in the wide and narrow quantum wells, respectively. The drastic difference between the electron scattering time and hole tunneling time means that the density of the carriers can be very large ($\sim 10^{12}$ cm^{-2}) for optical excitation intensity of only a few mW/cm^2 [73]. By varying the optical excitation intensity, we are able to continuously vary the electron density in the wide quantum well, in which we will study the spin dynamics through transient Kerr rotation technique.

The sample is grown by molecular beam epitaxy on n^+ GaAs substrate. It consists of nominally a 6800 Å GaAs buffer layer, a 6000 Å $\mathrm{Al_{0.6}Ga_{0.4}As}$ etch stop layer, a multiple quantum well consisting of 20 periods of 25- and 68-Å GaAs double quantum wells separated by AlAs barriers with a width of 80 Å, a 6000 Å $\mathrm{Al_{0.6}Ga_{0.4}As}$ etch stop layer, and a 1000 Å GaAs capping layer. The quantum wells are nominally undoped.

5.2.2 Experimental setup

We perform transient Kerr rotation measurements in a magneto-optical cryostat, in which a magnetic field of 6 T is applied normal to the quantum well growth direction (Voigt geometry) [30, 33]. Pump and probe pulses are produced by a mode-locked Ti:sapphire laser, and are circularly and linearly polarized, respectively. Both pulses are spectrally filtered to enable independent tuning of their energies. The energies of the pump and probe pulses are tuned to the trion resonance of the wide quantum well for low energy excitation, except for spectral study. The spectral width of the pulses is adjusted to be 0.2 nm (resulting in ∼5 ps pulses) for spectrally resolved measurements. Average powers are 100 μW in the pump (except as specified in the text) and 20 μW in the probe beam. The carrier density upon pump pulse excitation is estimated to be 3×10^8 cm^{-2}/well. For time resolved photoluminescence measurement, we modulate the HeNe laser beam with an acousto-optic modulator and detect the photoluminescence (from HeNe excitation) by a 1/4-m grating spectrometer followed by a photomultiplier and lock-in amplifier. The photoluminescence signal is processed with a digital oscilloscope. All experiments were performed at 4 K except for the temperature dependence measurements.

5.2.3 Photoluminescence

Photoluminescence (PL) spectra at low temperature as a function of HeNe excitation intensity reveal electron accumulation in the wide quantum wells. We measure the PL spectra of the sample at a temperature of 4 K as a function of the HeNe excitation intensity, as shown in Figure 5.2. For this measurement, the sample is excited by both a CW Ti:sapphire laser at 1.676 eV (below the effective gap of the narrow quantum wells) and a HeNe laser (above the gap of the narrow wells). The PL spectrum due to HeNe excitation alone is removed from the total measured spectrum by subtraction. The resulting PL spectra shown in Figure 5.2 therefore originate from photoexcitation into the wide quantum wells only, with the electron density in the wide wells varied by varying the HeNe intensity. Under no HeNe excitation, the spectrum is dominated by the heavy hole exciton emission (1.6072 eV) in the wide quantum wells. As the HeNe excitation intensity

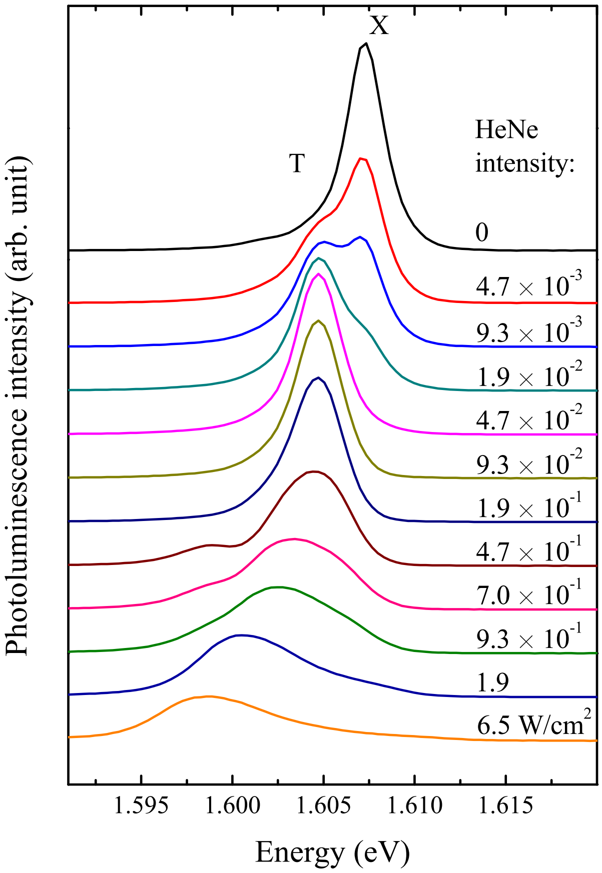

Figure 5.2: Low temperature ($T = 4$ K) PL spectra under photoexcitation into the wide wells only for various HeNe excitation intensities. The spectra are offset for clarity. X and T stand for exciton and trion, respectively.

is increased, a low energy shoulder emerges at 1.6047 eV, which is ascribed to recombination involving negatively charged excitons, or trions. We measure the spin dynamics in the wide quantum wells with a HeNe excitation intensity up to 1.9×10^{-1} W/cm^2. Above this intensity, the trion PL line gradually evolves into a broader peak, associated with the PL of a two-dimensional electron gas. The red shift of the peaks with increasing intensity is a result of the bandgap renormalization [74].

As the HeNe beam passes through the sample, it is attenuated due to the absorption by the quantum wells. This attenuation could result in a decrease in the electron density as a function of depth. This electron density inhomogeneity in the wide wells, if any, will result in different PL spectra originating from the front and back wide quantum wells (the PL spectrum is very sensitive to the electron density by the relative strength between exciton and trion emissions, as shown in Figure 5.2). We check the electron density inhomogeneity in the 20 wide quantum wells by measuring the PL spectrum with co-propagating and counter-propagating CW Ti:sapphire beam and HeNe beam. For this study, the sample is mounted on a sapphire plate with the opaque GaAs substrate removed by etching, to enable optical measurements from both sides of the sample. We measure the PL spectra from photoexcitation into the wide wells only, with the CW Ti:sapphire excitation at 1.624 eV (light hole exciton resonance in the wide wells, at which the absorption strength is comparable to that at HeNe energy). The luminescence is detected at the same side of the sample as the CW Ti:sapphire excitation enters. Assuming a significant attenuation of the CW Ti:sapphire beam by the quantum wells, the PL spectrum detected will have more contributions from the beam entrance side (if there is no significant attenuation of the Ti:sapphire beam, the HeNe beam intensity should also be fairly uniform in different wells). By directing HeNe excitation to the sample from either side, we are able to monitor the electron density inhomogeneity. We adjust the HeNe excitation intensity to obtain a PL spectrum with equal peak amplitudes of the exciton and trion lines (similar to the PL spectrum for 9.3 mW/cm^2 in Figure 5.2), and record the HeNe intensity for excitation from either side. We obtain almost identical intensities for excitation from both sides (10.6 mW/cm^2 for co- and 10.8 mW/cm^2 for counter-propagating), and therefore conclude that there is negligible difference of electron densities in the front and back quantum wells. We also measure the absorption

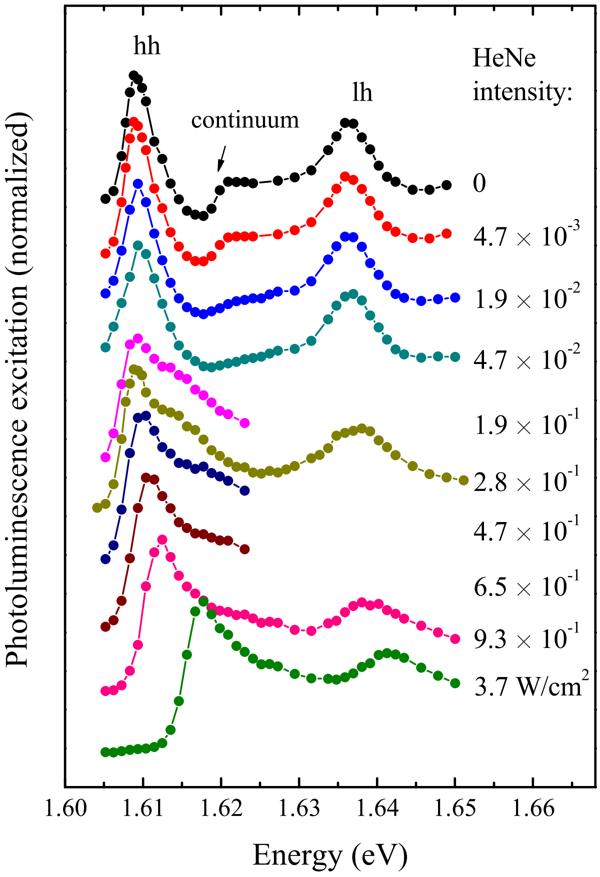

Figure 5.3: Low temperature ($T = 4$ K) PLE spectra of the wide wells for various HeNe excitation intensities. The spectra are normalized and offset for clarity. hh and lh stand for heavy hole and light hole exciton, respectively.

of HeNe by the sample and observe no saturation for the whole HeNe intensity range used.

5.2.4 Photoluminescence excitation and absorption spectra

The PL spectra shown in Figure 5.2 provide information on interband transitions near the wide quantum well bandgap. The energy position and strength of the electronic transition obtained from the PL spectrum are, in general, different from those obtained from the absorption spectrum. With the existence of localized states in quantum wells (especially in narrow wells), there is a shift in energy between positions of the band maxima of the absorption and luminescence spectra of the same electronic transition (Stokes shift). It is therefore desirable to measure the absorption spectrum of the sample. The mixed type I/type II quantum wells is grown on thick GaAs substrate and a direct absorption measurement of the sample is not possible. We measure the photoluminescence excitation spectrum (PLE) instead. Figure 5.3 shows the low temperature PLE spectra of the wide quantum wells for various HeNe excitation intensities. The PLE spectrum is measured by scanning the excitation photon energy (from a CW Ti:sapphire laser) and monitoring the PL signal strength at an energy of 1.6025 eV (below the trion resonance, as shown in Figure 5.2).[2] At low HeNe intensity, the PLE spectrum shows the heavy hole and light hole excitonic peaks, as well as the absorption of the continuum states, which are labeled in the figure. At high HeNe intensity, the excitonic peaks are replaced by a broad, asymmetric peak called the "Fermi edge singularity" [60], with the absorption enhanced near the Fermi level. The intensity of the absorption spectrum rises relatively quickly on the low energy side but falls off slowly on the high energy side, to merge into the continuum absorption. The shift of resonance to higher energy with increasing HeNe intensity is a direct evidence of electron accumulation in the wide wells, due to the band-filling of electrons. By comparing the PLE spectrum with the PL spectrum shown in Figure 5.2, we observe a Stokes shift of $\sim$1.5 meV between the exciton PLE peak and the corresponding PL peak at low HeNe excitation intensity, indicating carrier localization in the quantum wells.

---

[2] The low energy PL signal monitored originates from CW Ti:sapphire excitation only. This is achieved by modulating the Ti:sapphire beam with an optical chopper and detecting the PL signal with phase-sensitive lock-in detection. The HeNe excitation does not contribute to the PL signal monitored, and is only used to vary electron density in the wide wells.

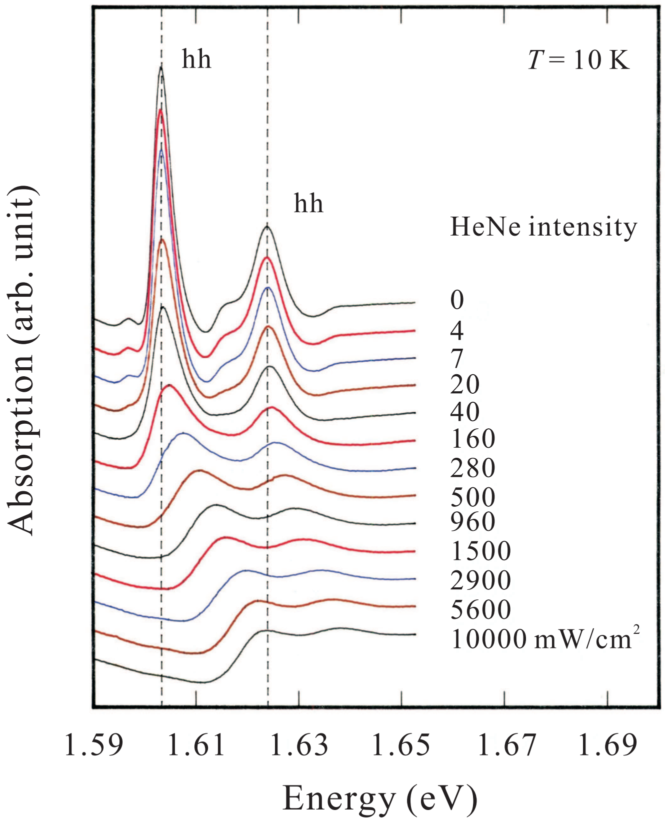

Figure 5.4: Low temperature ($T = 10$ K) absorption spectra near the wide quantum well bandgap for various HeNe excitation intensities. The spectra are taken with a sample with its substrate etched away. The spectra are offset for clarity. hh and lh stand for heavy hole and light hole exciton, respectively. Data provided by P. Dawson.

We measure the absorption spectrum by mounting the sample on a sapphire plate with the opaque GaAs substrate removed by etching. The process of mounting and etching, however, strains the sample, which shifts and broadens the resonances as compared to the unetched sample used in our study. Therefore, the absorption spectra are only measured as a reference. The absorption spectra near the wide quantum well bandgap are plotted in Figure 5.4 at different HeNe intensity. They are very similar to the corresponding PLE spectra. We again observe the heavy and light hole exciton peaks, and observe a blue-shift of the resonances with increasing HeNe intensity. The resonances are also somewhat broadened by an underlying Fabry-Pérot fringe (resulting from the interference effect of the thin sample) which can be clearly seen on a wider range spectrum.

5.2.5 Electron density estimation

The optically excited 2DEG density (through HeNe excitation) in the wide quantum well can be calibrated through time-resolved PL (from HeNe excitation only) [73]. The basic idea behind this work is that if the decay of the PL from the wide quantum well is monitored following pulsed HeNe excitation, not only will we observe the fast (<ns) recombination of carriers excited directly in the wide well but also we should observe a much slower transient. This slow decay should arise from the sequential process of hole tunneling and subsequent recombination of holes with electrons in the wide well. The time constant associated with this sequential process will be governed by the hole tunneling rate, which is expected to be much less than the rates associated with scattering and recombination. In Figure 5.5 we show the photoluminescence transient after pulsed HeNe excitation for several HeNe intensities. The PL is measured by sampling all the light emitted by the sample. The slow decays, corresponding to the hole tunneling process from the narrow well to the wide well, can be clearly seen after the fast decay of the directly excited electron hole pairs. The measured decay of the initial fast transient is limited by the system response. In the inset of Figure 5.5, the hole tunneling time is plotted as a function of HeNe excitation intensity. The time constants are obtained from exponential fit of the photoluminescence transients. The hole tunneling time remains fairly constant (~ 50 μs) over the whole HeNe intensity range, expect at low intensities, where the measured PL signals becomes noisy to provide reliable time constants.

As discussed in Reference [73], this method can only give estimated values of

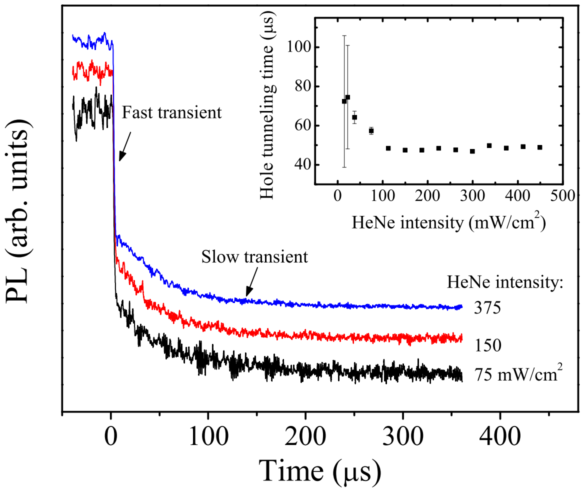

Figure 5.5: Time-resolved photoluminescence from pulsed HeNe excitation (T = 4 K). The transients are normalized and offset for clarity. Inset: Hole tunneling time (from narrow well to wide well) as a function of HeNe excitation intensity. The time constants are obtained from exponential fit of the photoluminescence transients.

the 2DEG density due to multiple processes in the PL decay. Therefore, the values of the excitation intensity instead of the equivalent excited electron densities are quoted in the text. However, given that our measured hole tunneling time remains fairly constant over the whole HeNe intensity range used in our measurements, the 2DEG density should be proportional to the HeNe intensity. At the relatively low HeNe intensities used in this experiment, saturation of electron accumulation due to the space-charge field set up by the spatially-separated electrons and holes is negligible. The electron density in the wide quantum well is estimated to be $\sim 1 \times 10^9$ cm^{-2} per mW/cm^2 per well.

5.3 Electron spin dynamics

5.3.1 Data analysis

The transient Kerr rotation signal oscillates under the transverse magnetic field due to Larmor precession of the electron spin. The oscillatory dynamics reveal the electron spin dephasing time and the precession frequency (which gives g^*). CW HeNe excitation is used to continuously vary the electron density in the wide quantum well, with the electron density proportional to the HeNe intensity over the intensity range used in our measurements, as detailed in Section 5.2.5. Only the data after 400 ps are analyzed, so that our results are not affected by short time delay properties such as exciton spin dephasing [transient grating measurements yield a carrier lifetime of ~100 ps (not shown)]. With the optically-created electrons and holes recombined already, only the spin precession of excess electrons is measured, and the resulting spin dephasing time and g factor should be that of the electrons without exchange interaction with the holes [47].

The transient signal measured normally consists of oscillations with two different frequencies, and their relative strengths depend on where the pump and probe photon energies are set. Figure 5.6 shows the transient signals with one or two frequency components at different pump and probe energies, with a HeNe intensity of 4.7mW/cm^2. As will be discussed in Section 5.3.2, the low frequency component originates from the main quantum well width, while the high frequency component is believed to correspond to several quantum wells with slightly narrower well width, which will not be considered in this study. To retrieve information only related to the main quantum well width, we perform least-squares fitting on the data using a formula with two oscillation frequencies and decay times, $\theta_K(t) = A_1 e^{-t/\tau_1}\cos(\omega_{L1}t) + A_2 e^{-t/\tau_2}\cos(\omega_{L2}t)$, which give the electron spin dephasing times. The precession frequency (g^*) is obtained from fast Fourier

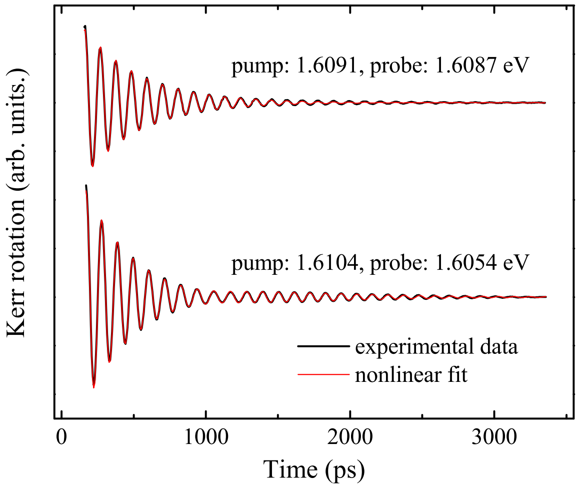

Figure 5.6: Transient Kerr rotation signals measured at two different pump and probe photon energies, with a HeNe intensity of 4.7mW/cm^2. The transient signal for pump energy of 1.6091 eV is fit with a single-frequency oscillation decay, while the signal for pump energy of 1.6104 eV is fit with a formula with two oscillation frequencies and decay times.

analysis, with the value being the peak position of the Fourier spectra.

5.3.2 Spectral study

In general, the transient Kerr rotation signal measured consists of beating signals from two different precession frequencies under magnetic fields. We check the origin of the two frequencies by a spectral study of the pump excitation energy. We plot the spectrum of Kerr rotation amplitude for the two frequency components in Figure 5.7(a), with the amplitude obtained from least-square fit of the transient signal. The probe photon energy is set at 1.6108 eV for this measurement. The amplitude of the low frequency component peaks at the heavy hole exciton resonance, while that of the high frequency component peaks at a higher energy (~3 meV above). The PLE spectrum of the wide quantum well

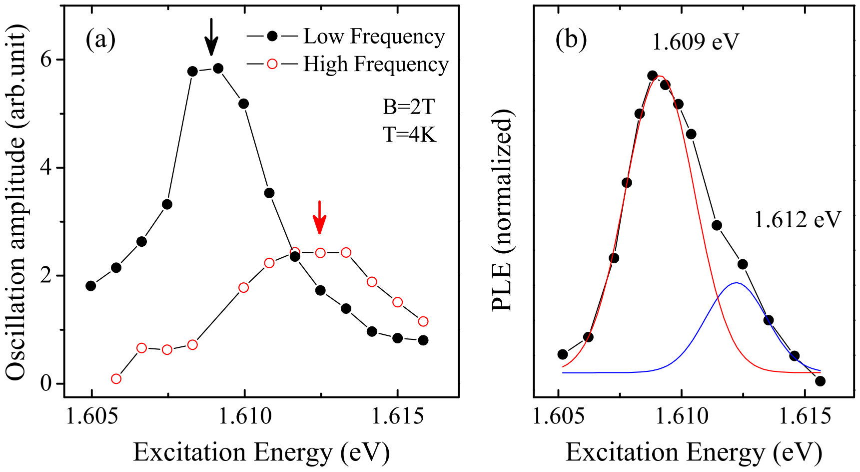

Figure 5.7: (a) Kerr rotation amplitude for the two frequency components as a function of pump excitation energy, with the probe photon energy set at 1.6108 eV. (b) Circles: PLE spectrum of the wide quantum well under no HeNe excitation; full lines: Fit of the spectrum with two Gaussian lines centered at different photon energies.

under no HeNe excitation is plotted in Figure 5.7(b), which can be well fit with two Gaussian lines centered at 1.609 eV and 1.612 eV, respectively. The similarity between the spectra in Figure 5.7(a) and (b) suggests that the two frequency components correspond to the electron spin precession in quantum wells with two different well widths (supported by the dependence of the electron g factor on quantum well width). While the low frequency components originates from the main quantum well width, the high frequency component is assigned to electron spin precession in several quantum wells with slightly narrower width, which exciton peak is also visible in the PLE spectrum (centered at 1.612 eV). In the following experiments, we will be using low energy pump and probe excitation (near trion resonance), so that the narrower quantum well contribution to the Kerr rotation signal is minimized.

5.3.3 Electron localization

In quantum wells, especially narrow wells in our sample, fluctuations of the well width may result in the formation of localized electronic tail states. This is due to the dependence of the quantization energy on the well width. As shown by the diagram in Figure 5.8(a), the conduction band electrons tend to localize at areas with slightly wider well width. Electrons in the quantum well will first occupy these localized states, since they have a lower energy. As the electron density in the quantum well is increased, electrons become more delocalized and can finally move freely in the quantum well plane after the localized states are completely filled. We therefore have a transition from localized to delocalized electrons with increasing electron density. The electrons can also be localized by random potential fluctuations produced by the laterally localized holes in the narrow quantum in a mixed type I/type II structure [75]. For simplicity, we model the electron localization by only considering the effects from well width fluctuations.

The unperturbed DOS (per unite area) of a two-dimensional system, i.e. without considering electron localization, is expressed as

$$D(E) = \frac{m^*}{\pi\hbar^2}\Theta(E - E_c), \tag{5.3}$$

with m^* the effective mass of the conduction band electron, $\Theta(E)$ the Heaviside step function, and E_c the cutoff energy. This steplike DOS is plotted in Figure 5.8(b) as dashed line. Now consider a quantum well with a distribution of the well widths. The DOS for each well width still follows Equation 5.3, with E_c for each width differs due to quantum confinement. The overall DOS of the perturbed two-dimensional system is then obtained by integrating the DOS for each width over the well width distribution $[P(E)]$, which follows,

$$\bar{D}(E) = \int_{-\infty}^{\infty} D(E - E^{'})P(E^{'})dE^{'}. \tag{5.4}$$

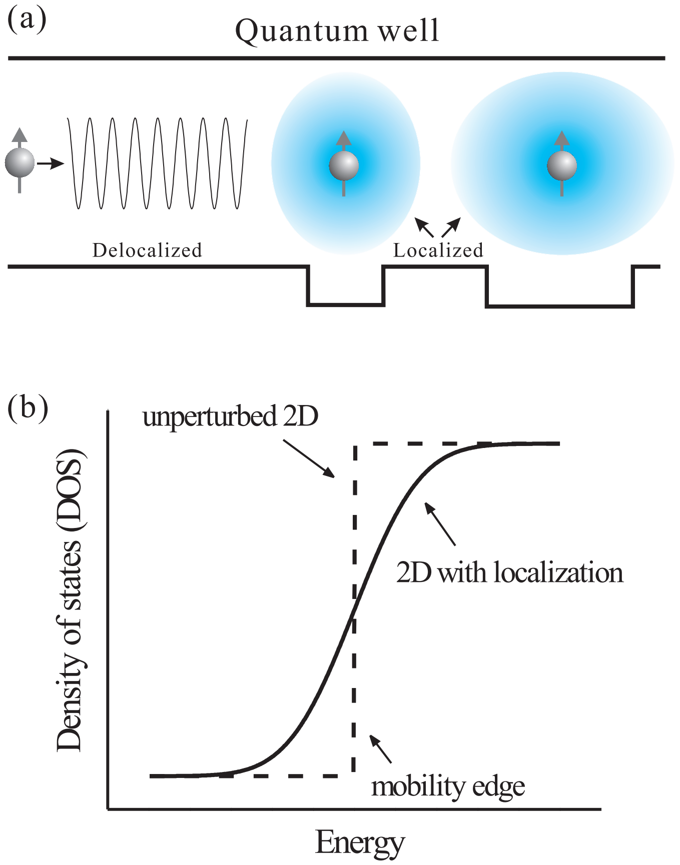

Figure 5.8: (a) Schematic diagram of electron localization in a quantum well with well width fluctuation. (b) DOS of a two-dimensional system with a localization tail (full line) and that of the unperturbed two-dimensional system (dashed line).

We model the DOS with well width fluctuations by assuming a Gaussian distribution of the well width

$$P(E) = (\sqrt{2\pi}\Delta E)^{-1} \exp\left(-\frac{1}{2}(E/\Delta E)^2\right), \tag{5.5}$$

with ΔE the fluctuation width. The DOS of the perturbed two-dimensional system is then carried out by inserting Equation 5.5 in Equation 5.4:

$$\bar{D}(E) = \frac{m^*}{2\pi\hbar^2}\left(1 + \mathrm{erf}(\frac{E - E_c}{\sqrt{2}\Delta E})\right). \tag{5.6}$$

The calculated DOS is plotted in Figure 5.8(b) as a full line. The electron localization is represented by the tail states at low energies, which have smaller DOS

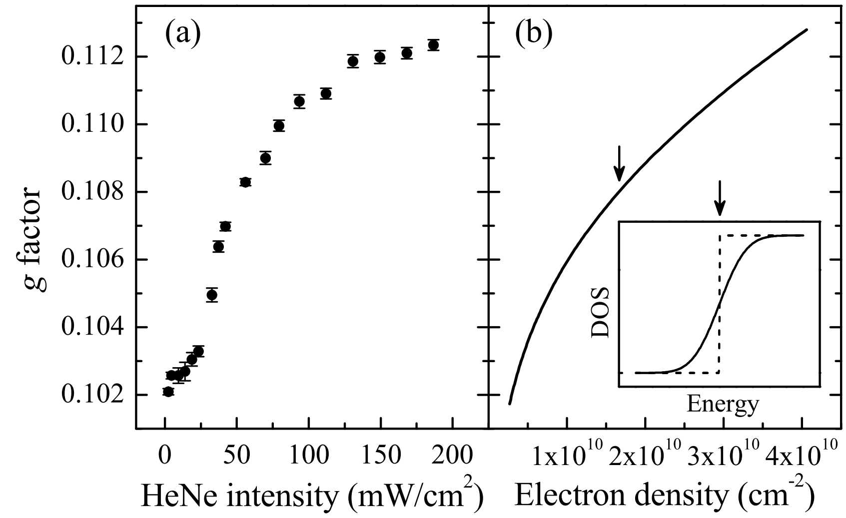

Figure 5.9: (a) Measured g^* dependence on the HeNe excitation intensity. (b) Calculated g^* dependence on electron density, as described in the text. The arrows indicate the electron density and energy of the mobility edge. Inset: DOS of a two-dimensional system with a localization tail (full line) and that of the unperturbed two-dimensional system (dashed line).

than the unperturbed two-dimensional system. The mobility edge, the critical point at which a transition from localized to extended electronic states, is at E_c.

5.3.4 Electron g factor nonlinearity

The g factor dependence on HeNe excitation intensity is plotted in Figure 5.9(a). The sign of the g factor is determined to be positive for our sample.[3] The value of g^* increases nonlinearly with increasing HeNe excitation intensity, in contrast with a linear dependence expected for an unperturbed two-dimensional system (see Section 5.1). The g^* data in Figure 5.9(a) have a bigger increase

---

[3] The sign of the g factor is not available from transient Kerr rotation measurements. We measure the anisotropy of the g factor and obtain a larger absolute value of g for field perpendicular to the growth axis than that for field parallel. According to Reference [76], this indicates a positive sign of g factor for our sample.

at low HeNe intensity (electron density) than at high HeNe intensity, indicating smaller densities of states for low electron densities (refer to Equation 5.2). We therefore propose that the nonlinearity of the electron g factor is associated with a transition from localized to delocalized electrons. We model the g^* dependence on electron density by using a DOS following Equation 5.6, which is for a disordered quantum well system resulting from a Gaussian distribution of the well width fluctuation. We also assume a linear dependence of g^* on electron energy, $g^* = g_0 + \beta E$. The linear coefficient β in the energy dependence of g^* has been calculated using five-band $k \cdot p$ perturbation theory [14]. Based on the calculated DOS and the energy dependence of g factor, we calculate the electron g factor dependence on electron density, which is shown in Figure 5.9(b). The calculation assumes zero temperature and equal spin-up and spin-down electron populations, with the width of the Gaussian distribution set at 1.5 meV to account for the Stokes shift and g_0 as the only free parameter. The calculation represents the form of the experimental data well except at low HeNe intensity. The deviation is probably due to increased electron temperature resulting from pump excitation, which has a bigger effect on g^* at low carrier density (discussed in detail later). We therefore confirm the presence of localized states, which have a smaller DOS, and thus produce a more rapid change in the g factor with electron density (Equation 5.2).

5.3.5 Spin dephasing time vs. electron density

Figure 5.10 shows the electron spin dephasing time as a function of the HeNe intensity. The electron spin dephasing time shows a nonmonotonic dependence on carrier concentration, with a maximum time constant at an intensity of 25 mW/cm^2 (see Section 5.2.5 for electron density). The presence of localized and delocalized states accounts for the opposite trends in the spin dephasing time

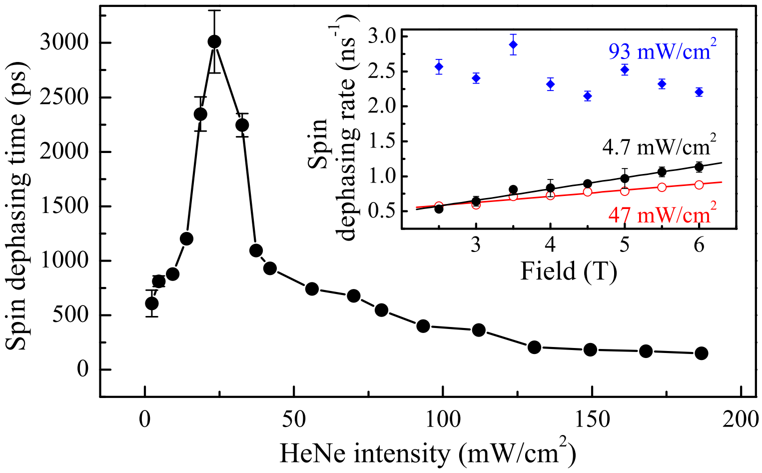

Figure 5.10: Electron spin dephasing time vs. HeNe excitation intensity. The inset shows the measured spin dephasing rate dependence on magnetic field for several HeNe intensities, with solid lines the linear fits to the data. Error bars are plotted except where they are smaller than the symbol size.

at low and high electron densities, as displayed in Figure 5.10. At high electron concentrations, the decrease of spin dephasing time with increasing density suggests a D'yakonov-Perel' (DP) mechanism [64], in which the spin dephasing rate is inversely related to the momentum scattering rate. The 2DEG efficiently screens the potential fluctuations, and suppresses the momentum scattering rate, resulting in a decrease of the spin dephasing time with carrier density. Below the critical electron density, the electrons become localized in the potential fluctuations, and the electron spins dephase from the inhomogeneous environment, which is often attributed to strong hyperfine interactions with the nuclear magnetic moments. The critical density should correspond to the crossover between the localized and delocalized states, where different spin dephasing mechanisms dominate.

An additional contribution to the spin dephasing may arise from a spread in the electron g factor (due to distribution of electron energies over localized states), which results in an inhomogeneous dephasing of the electron spin under magnetic field. This is shown as a linear dependence of the spin dephasing rate on the magnetic field, $1/T_2^*(B) \approx 1/T_2^*(0) + \Delta g \mu_B B/2\hbar$, with Δg a Gaussian variance of the g factor [24]. In the inset of Figure 5.10, spin dephasing rate is measured as a function of the magnetic field for several HeNe intensities. For the two lower HeNe intensities, the spin dephasing rate increases linearly with field. A Δg of 0.0026 (0.0014) for 4.7 (47) mW/cm^2 is retrieved from a linear fit, which supports an inhomogeneous spin dephasing for the localized electrons. The decrease of Δg with increasing electron density suggests a decrease of the g factor inhomogeneity as the electrons become less localized, which is evidenced by the measured g factor dependence on electron density, as shown in Figure 5.9. At a HeNe intensity of 93 mW/cm^2, where electrons become delocalized, we observe a small decrease of the dephasing rate with field, which suggests a DP mechanism under magnetic field [24]. Thus, as the electron density is increased, the electron spin relaxation undergoes a transition from being limited by inhomogeneous dephasing to homogeneous decoherence.

5.3.6 Electron g factor vs. temperature and excitation intensity

The temperature dependence of the electron g factor provides further insight into the electron localization. Figure 5.11(a) shows the measured g^* as a function of temperature for a series of HeNe intensities. Drastic temperature dependence differences are observed for different intensities. Two aspects need to be considered to account for the variation of g factor on temperature: the variation due to lattice temperature changes, and the ensemble average of the electron g factor due to thermal distribution of electrons. The former comes mainly from the temperature dependence of the fundamental energy gap, but predictions from

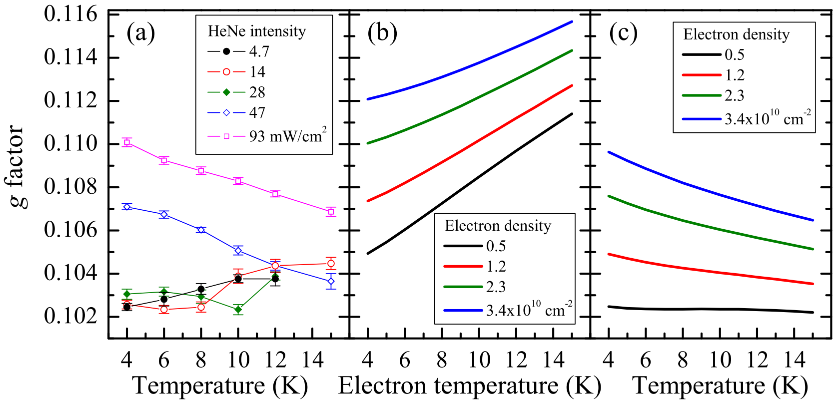

Figure 5.11: (a) Measured g^* dependence on temperature for a series of HeNe intensities. (b) Calculated carrier temperature dependence of electron $\langle g^* \rangle$ for several 2DEG densities (lattice temperature effect not included). (c) Calculated temperature dependence of $\langle g^* \rangle$ with contributions from both the lattice and carrier temperature.

$k \cdot p$ perturbation theory fail to describe the experimental results [23]. The latter contribution can be accounted for by calculating the average g factor from its dependence on the energy, weighted by the DOS, along with a Fermi-Dirac distribution of the electrons:

$$\langle g^* \rangle = \frac{\int_0^\infty g(E)D(E)(f^+(E) - f^-(E))dE}{\int_0^\infty D(E)(f^+(E) - f^-(E))dE}, \tag{5.7}$$

with $D(E)$ the modified DOS of the 2DEG [Figure 5.8(b)] and f^+ (f^-) the Fermi-Dirac distribution for the spin-up (spin-down) electrons. The calculated results for the carrier temperature dependence are shown in Figure 5.11(b) (lattice temperature effect not included). Increasing carrier temperature will transfer electrons from below to above the Fermi energy. For a degenerate electron gas which has a constant DOS with energy, $\langle g^* \rangle$ should be that at the Fermi energy since g factor increases linearly with energy. This is however not the case for localized electrons,

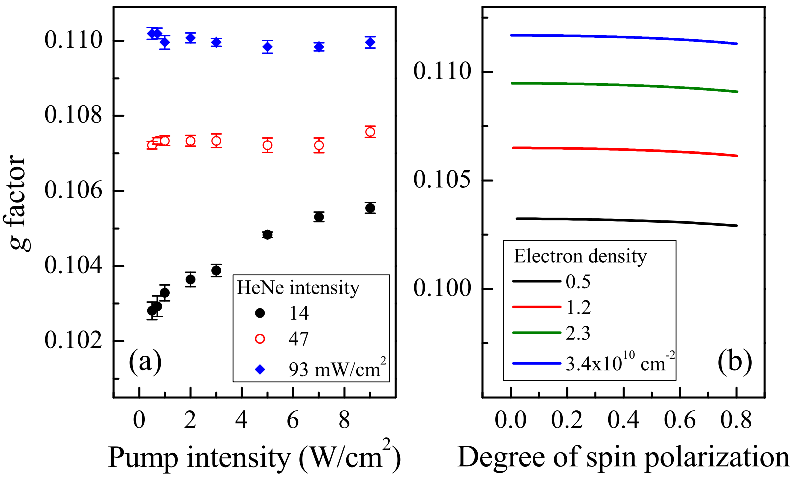

Figure 5.12: (a) Measured $\langle g^* \rangle$ vs. the pump excitation intensity for different HeNe intensities. (b) Calculated $\langle g^* \rangle$ as a function of degree of the electron spin polarization.

which have a rapid change of the DOS. The average g factor will increase with carrier temperature due to the greater DOS above the Fermi energy. This effect is well represented in Figure 5.11(b) for localized and delocalized electrons. In Figure 5.11(c) we calculate $\langle g^* \rangle$ by including contributions from both the lattice and carrier temperature. Given the lack of theoretical results that match experimental lattice temperature dependence [23], we empirically represent the lattice temperature contribution by adding a linear term to the carrier temperature dependence, so that the combined dependence at high density matches the measured results at the highest HeNe intensity. The calculation represents the trend of the experimental data.

Increasing the pump excitation intensity has previously been shown to primarily increase the temperature of the electron gas rather than the crystal lattice [77]. The excitation intensity dependence should be a good check to our theory on the electron g factor, since the carrier and lattice temperature have different effects on the $\langle g^* \rangle$ [as seen in Figure 5.11(a) and (b)]. In Figure 5.12(a), the measured $\langle g^* \rangle$ is plotted against the pump excitation intensity for several HeNe intensities. The carrier density due to pump excitation is estimated to be 3×10^8 cm^{-2} per 1 W/cm^2. The $\langle g^* \rangle$ shows strong variation with excitation intensity at low 2DEG density, but has little variation at high density. The figure also shows a similar trend as the calculated carrier temperature dependence [Figure 5.11(b)]. The lattice temperature dependence of the $\langle g^* \rangle$ [Figure 5.11(a)], however, behaves quite differently. This further establishes that increasing the excitation intensity does heat up the carriers rather than the lattice. By increasing the excitation intensity, we also increase the degree of spin polarization of the electron gas, which alone should also affect the g factor. We calculate the electron $\langle g^* \rangle$ dependence on the degree of spin polarization of the 2DEG, as shown in Figure 5.12(b). The degree of spin polarization is defined as $(n^+ - n^-)/(n^+ + n^-)$, with n^+ (n^-) the density of the spin-up (spin-down) electrons. The calculation is based on Equation 5.7, with the degree of spin polarization represented by a difference between the Fermi energy for the spin-up electrons (f^+) and that for the spin-down electrons (f^-). The results show that spin polarization of the 2DEG does not affect the $\langle g^* \rangle$ as much as increasing the carrier temperature, and g factor variation with excitation intensity is mainly related to the change of the electron temperature.

Transient Kerr rotation measurements provide reliable values of the g factor of bare electrons, as opposed to those obtained from magnetoquantum oscillations, which can be strongly enhanced by many-body exchange interactions [78]. We therefore ignore the exchange interactions between carriers in our model. The variation of electron g factors in quantum wells arises mainly from the change in electron energy, where the assumption of a linear dependence on energy should be precise for the energy range (several meV) present in the measurements. Other contributions, such as anisotropy of the quantum well potential, strain and electron wavefunction penetrating into barriers, should have minimal effects, because of the use of the same sample, and the small change of 2DEG density in the measurements. The non-parabolicity of the conduction band has negligible effect on the variation of the g factor over the change in Fermi energy studied.

In summary, we systematically study the spin dynamics of the electron gas in a GaAs quantum well sample, where the electron density in the quantum well can be varied through optical excitation. We show that the electron spin coherence is limited by the interplay between localization by disorder and dynamical scattering processes. For localized electrons, disorder limits the spin dephasing time due to inhomogeneous g factor distributions. The measured electron g factor dependence on electron density directly characterizes the disorder potential. Using our knowledge of the DOS, a simple model estimates the temperature and excitation intensity dependence of the g factor, in agreement with our experimental results. This work confirms the importance of disorder in spin coherence in semiconductors, which provides predictive power for designing spin-based electronics devices.

Chapter 6

Conclusion

In this thesis we focus on the optical manipulation of spin coherence in semiconductors. We use transient Faraday/Kerr rotation and other optical spectroscopy techniques (such as absorption, reflection, PL and PLE) to study spin dynamics in various semiconductor quantum well systems. In Chapter 3, we experimentally study the spectra of the transient Faraday/Kerr rotations near the exciton resonances of an undoped GaAs multiple quantum well. While the transient Faraday/Kerr techniques have been widely used for spin study, spectral studies can reveal the underlying spin dependent nonlinearities. They are also useful in selectively generating and detecting spin polarizations of different species. A spectrum calculation with a multilayer characteristic matrix model is performed, with the results quantitatively agree with the measured linear spectra and Faraday/Kerr spectra. We show that the Kerr spectra depend not only on the optical nonlinearities but also on linear optical effects such as interference from layer structures. In Chapter 4, we study the interplay of spin dynamics between excitons, negatively-charged excitons (trions) and the two-dimensional electron gas with lightly modulation-doped CdTe quantum wells. In these systems, the interband properties are dominated by excitons and trions at low temperatures, but the electron spin can persist after recombination of optically excited carriers. Coherent optical generation and manipulation of the electron spins require an understanding of the connection between electron spin and optical transitions through which the spin polarization is initiated and controlled. By a spectral study of Kerr rotation, spin relaxation of individual species is resolved. The spin dynamics is quantitatively described by solving rate equations involving the spin populations of excitons, trions and the electron gas. Under resonant excitation of excitons, spin polarization of the electron gas is generated through trion formation process, with the spin coherence partially lost through exciton spin relaxation. In Chapter 6, we study the effects of disorder on electron spin dynamics in a GaAs quantum well. A mixed type I/type II GaAs/AlAs quantum well is used, where the carrier density in the quantum wells can be continuously varied with CW optical excitation. We vary the electron density in a two-dimensional electron gas, and show that the electron spin coherence is lost due to the interplay between localization by disorder and dynamical scattering processes. By measuring the electron Landé g factor dependence on electron density, we are able to determine the density of states, which characterizes the disorder potential. Using our knowledge of the density of states, a simple model estimates the temperature and excitation intensity dependence of the g factor, in agreement with our experimental measurements. Our results show that the longest spin coherence is obtained for weakly localized spins, which may dictate a compromise in the design of spintronic devices between increasing the spin coherence time and improving transport properties.

Bibliography

[1] D. D. Awschalom, D. Loss, and N. Samarth, editors, Semiconductor Spintronics and Quantum Computation (Springer, Berlin, 2002).

[2] I. Žutić, J. Fabian, and S. Das Sarma, "Spintronics: Fundamentals and applications," Rev. Mod. Phys. **76**, 323 (2004).

[3] D. D. Awschalom, R. A. Buhrman, J. M. Daughton, S. von Molnar, and M. L. Roukes, editors, Spin Electronics (Kluwer, Dordrecht, 2004).

[4] S. A. Wolf, D. D. Awschalom, R. A. Buhrman, J. M. Daughton, S. von Molnar, M. L. Roukes, A. Y. Chtchelkanova, and D. M. Treger, "Spintronics: a spin-based electronics vision for the future," Science **294**, 1488 (2001).

[5] G. A. Prinz, "Magnetoelectronics," Science **282**, 1660 (1998).

[6] S. Datta and B. Das, "Electronic analog of the electro-optic modulator," Appl. Phys. Lett. **56**, 665 (1990).

[7] C. F. Klingshirn, Semiconductor Optics (Springer, Berlin, 2005).

[8] R. I. Dzhioev, K. V. Kavokin, V. L. Korenev, M. V. Lazarev, B. Y. Meltser, M. N. Stepanova, B. P. Zakharchenya, D. Gammon, and D. S. Katzer, "Low-temperature spin relaxation in n-type GaAs," Phys. Rev. B **66**, 245204 (2002).

[9] J. M. Kikkawa, I. P. Smorchkova, N. Samarth, and D. D. Awschalom, "Room-temperature spin memory in two-dimensional electron gases," Science **277**, 1284 (1997).

[10] J. M. Kikkawa and D. D. Awschalom, "Lateral drag of spin coherence in gallium arsenide," Nature **397**, 139 (1999).

[11] D. Loss and D. P. DiVincenzo, "Quantum computation with quantum dots," Phys. Rev. A **57**, 120 (1998).

[12] A. P. Heberle, W. W. Rühle, and K. Ploog, "Quantum beats of electron Larmor precession in GaAs wells," Phys. Rev. Lett. **72**, 3887 (1994).

[13] J. J. Baumberg, S. A. Crooker, D. D. Awschalom, N. Samarth, H. Luo, and J. K. Furdyna, "Ultrafast Faraday spectroscopy in magnetic semiconductor quantum structures," Phys. Rev. B **50**, 7689 (1994).

[14] C. Hermann and C. Weisbuch, "$\vec{k}\cdot\vec{p}$ perturbation theory in III-V compounds and alloys: a reexamination," Phys. Rev. B **15**, 823 (1977).

[15] J. Shah, Ultrafast Spectroscopy of Semiconductors and Semiconductor Nanostructures (Springer, New York, 1996).

[16] F. Meier and B. P. Zakharchenya, editors, Optical Orientation (North-Holland, Amsterdam, 1984).

[17] B. E. A. Saleh and M. Teich, Fundamentals of Photonics (Wiley, New York, 1991).

[18] A. M. Weiner, "Femtosecond pulse shaping using spatial light modulators," Rev. Sci. Instrum. **71**, 1929 (2000).

[19] D. D. Awschalom, "Manipulating and storing spin coherence in semiconductors," Physica E **10**, 1 (2001).

[20] M. Oestreich, S. Hallstein, A. P. Heberle, K. Eberl, E. Bauser, and W. W. Rühle, "Temperature and density dependence of the electron Landé g factor in semiconductors," Phys. Rev. B **53**, 7911 (1996).

[21] D. J. Oliver, "Electrical Properties of n-Type Gallium Arsenide," Phys. Rev. **127**, 1045 (1962).

[22] M. Furis, D. L. Smith, S. A. Crooker, and J. L. Reno, "Bias-dependent electron spin lifetimes in n-GaAs and the role of donor impact ionization," Appl. Phys. Lett. **89**, 102102 (2006).

[23] M. Oestreich and W. W. Rühle, "Temperature Dependence of the Electron Landé g Factor in GaAs," Phys. Rev. Lett. **74**, 2315 (1995).

[24] J. M. Kikkawa and D. D. Awschalom, "Resonant Spin Amplification in n-Type GaAs," Phys. Rev. Lett. **80**, 4313 (1998).

[25] R. Bratschitsch, Z. Chen, and S. T. Cundiff, "Ultrafast spin phenomena in highly excited n-doped GaAs," Phys. Status Solidi C **0**, 1506 (2003).

[26] M. J. Yang, R. J. Wagner, B. V. Shanabrook, J. R. Waterman, and W. J. Moore, "Spin-resolved cyclotron resonance in InAs quantum wells: A study of the energy-dependent g factor," Phys. Rev. B **47**, 6807 (1993).

[27] A. A. Sirenko, T. Ruf, M. Cardona, D. R. Yakovlev, W. Ossau, A. Waag, and G. Landwehr, "Electron and hole g factors measured by spin-flip Raman scattering in CdTe/$\mathrm{Cd}_{1-x}\mathrm{Mg}_x$Te single quantum wells," Phys. Rev. B **56**, 2114 (1997).

[28] W. Maślana, W. Mac, J. A. Gaj, P. Kossacki, A. Golnik, J. Cibert, S. Tatarenko, T. Wojtowicz, G. Karczewski, and J. Kossut, “Faraday rotation in a study of charged excitons in $Cd_{1-x}Mn_xTe$,” Phys. Rev. B **63**, 165318 (2001).

[29] C. Testelin, C. Rigaux, and J. Cibert, “Resonant magneto-optic Kerr effect in $CdTe/Cd_{1-x}Mn_xTe$ quantum-well structures,” Phys. Rev. B **55**, 2360 (1997).

[30] S. A. Crooker, D. D. Awschalom, J. J. Baumberg, F. Flack, and N. Samarth, “Optical spin resonance and transverse spin relaxation in magnetic semiconductor quantum wells,” Phys. Rev. B **56**, 7574 (1997).

[31] A. V. Kimel, F. Bentivegna, V. N. Gridnev, V. V. Pavlov, R. V. Pisarev, and T. Rasing, “Room-temperature ultrafast carrier and spin dynamics in GaAs probed by the photoinduced magneto-optical Kerr effect,” Phys. Rev. B **63**, 235201 (2001).

[32] T. Kuroda, Y. Hashimoto, and F. Minami, “Photo-induced Faraday rotation in GaAs/AlGaAs multiple quantum wells,” J. Lumin. **94–95**, 551 (2001).

[33] Z. Chen, R. Bratschitsch, and S. T. Cundiff, “Interference effects in transient Kerr spectra of a semiconductor multilayer structure,” Opt. Lett. **30**, 2320 (2005).

[34] J. D. Jackson, Classical Electrodynamics (Wiley, New York, 1999).

[35] M. Born and E. Wolf, Principles of Optics (Cambridge University Press, Cambridge, 1999).

[36] C. L. Mitsas and D. I. Siapkas, “Generalized matrix method for analysis of coherent and incoherent reflectance and transmittance of multilayer structures with rough surfaces, interfaces, and finite substrates,” Appl. Opt. **34**, 1678 (1995).

[37] W. W. Chow, S. W. Koch, and M. Sargent III., Semiconductor-Laser Physics (Springer, Berlin, 1994).

[38] E. D. Palik, editor, Handbook of Optical Constants of Solids (Academic, Orlando, 1998).

[39] A. V. Kimel, V. V. Pavlov, R. V. Pisarev, V. N. Gridnev, F. Bentivegna, and T. Rasing, “Ultrafast dynamics of the photo-induced magneto-optical Kerr effect in CdTe at room temperature,” Phys. Rev. B **62**, R10610 (2000).

[40] H. Hoffmann, G. V. Astakhov, T. Kiessling, W. Ossau, G. Karczewski, T. Wojtowicz, J. Kossut, and L. W. Molenkamp, “Optical spin pumping of modulation-doped electrons probed by a two-color Kerr rotation technique,” Phys. Rev. B **74**, 073407 (2006).

[41] Z. Chen, R. Bratschitsch, S. G. Carter, S. T. Cundiff, D. R. Yakovlev, G. Karczewski, T. Wojtowicz, and J. Kossut, "Electron spin polarization through interactions between excitons, trions and the two-dimensional electron gas," Phys. Rev. B (submitted).

[42] R. Bratschitsch, Z. Chen, S. T. Cundiff, D. R. Yakovlev, G. Karczewski, T. Wojtowicz, and J. Kossut, "Electron spin dephasing in n-doped CdTe/(Cd,Mg)Te quantum wells," Phys. Status Solidi B **243**, 2290 (2006).

[43] R. Bratschitsch, Z. Chen, S. T. Cundiff, E. A. Zhukov, D. R. Yakovlev, M. Bayer, G. Karczewski, T. Wojtowicz, and J. Kossut, "Electron spin coherence in n-doped CdTe/CdMgTe quantum wells," Appl. Phys. Lett. **89**, 221113 (2006).

[44] T. C. Damen, L. Via, J. E. Cunningham, J. Shah, and L. J. Sham, "Subpicosecond spin relaxation dynamics of excitons and free carriers in GaAs quantum wells," Phys. Rev. Lett. **67**, 3432 (1991).

[45] M. Z. Maialle, E. A. de Andrada e Silva, and L. J. Sham, "Exciton spin dynamics in quantum wells," Phys. Rev. B **47**, 15776 (1993).

[46] E. Vanelle, M. Paillard, X. Marie, T. Amand, P. Gilliot, D. Brinkmann, R. Lévy, J. Cibert, and S. Tatarenko, "Spin coherence and formation dynamics of charged excitons in CdTe/Cd$_{1-x-y}$Mg$_x$Zn$_y$Te quantum wells," Phys. Rev. B **62**, 2696 (2000).

[47] T. Amand, X. Marie, P. Le Jeune, M. Brousseau, D. Robart, J. Barrau, and R. Planel, "Spin Quantum Beats of 2D Excitons," Phys. Rev. Lett. **78**, 1355 (1997).

[48] M. Dyakonov, X. Marie, T. Amand, P. Le Jeune, D. Robart, M. Brousseau, and J. Barrau, "Coherent spin dynamics of excitons in quantum wells," Phys. Rev. B **56**, 10412 (1997).

[49] R. I. Dzhioev, V. L. Korenev, B. P. Zakharchenya, D. Gammon, A. S. Bracker, J. G. Tischler, and D. S. Katzer, "Optical orientation and the Hanle effect of neutral and negatively charged excitons in GaAs/Al$_x$Ga$_{1-x}$As quantum wells," Phys. Rev. B **66**, 153409 (2002).

[50] K. Kheng, R. T. Cox, M. Y. d' Aubigné, F. Bassani, K. Saminadayar, and S. Tatarenko, "Observation of negatively charged excitons X^- in semiconductor quantum wells," Phys. Rev. Lett. **71**, 1752 (1993).

[51] G. Finkelstein, V. Umansky, I. Bar-Joseph, V. Ciulin, S. Haacke, J.-D. Ganière, and B. Deveaud, "Charged exciton dynamics in GaAs quantum wells," Phys. Rev. B **58**, 12637 (1998).

[52] V. Ciulin, P. Kossacki, S. Haacke, J.-D. Ganière, B. Deveaud, A. Esser, M. Kutrowski, and T. Wojtowicz, “Radiative behavior of negatively charged excitons in CdTe-based quantum wells: A spectral and temporal analysis,” Phys. Rev. B **62**, R16310 (2000).

[53] T. A. Kennedy, A. Shabaev, M. Scheibner, A. L. Efros, A. S. Bracker, and D. Gammon, “Optical initialization and dynamics of spin in a remotely doped quantum well,” Phys. Rev. B **73**, 045307 (2006).

[54] E. A. Zhukov, D. R. Yakovlev, M. Bayer, G. Karczewski, T. Wojtowicz, and J. Kossut, “Spin coherence of two-dimensional electron gas in CdTe/(Cd,Mg)Te quantum wells,” Phys. Status Solidi B **243**, 878 (2006).

[55] M. V. G. Dutt, J. Cheng, B. Li, X. Xu, X. Li, P. R. Berman, D. G. Steel, A. S. Bracker, D. Gammon, S. E. Economou, R.-B. Liu, and L. J. Sham, “Stimulated and Spontaneous Optical Generation of Electron Spin Coherence in Charged GaAs Quantum Dots,” Phys. Rev. Lett. **94**, 227403 (2005).

[56] T. Wojtowicz, M. Kutrowski, G. Karczewski, and J. Kossut, “Modulation-doped $Cd_{1-x}Mn_xTe/Cd_{1-y}Mg_yTe$ quantum well structures with spatial in-plane profiling of the well width and the doping intensity,” Appl. Phys. Lett. **73**, 1379 (1998).

[57] P. Płochocka, P. Kossacki, W. Maślana, J. Cibert, S. Tatarenko, C. Radzewicz, and J. A. Gaj, “Femtosecond Study of the Interplay between Excitons, Trions, and Carriers in (Cd,Mn)Te Quantum Wells,” Phys. Rev. Lett. **92**, 177402 (2004).

[58] G. Eytan, Y. Yayon, M. Rappaport, H. Shtrikman, and I. Bar-Joseph, “Near-Field Spectroscopy of a Gated Electron Gas: A Direct Evidence for Electron Localization,” Phys. Rev. Lett. **81**, 1666 (1998).

[59] Y. Ohno, R. Terauchi, T. Adachi, F. Matsukura, and H. Ohno, “Spin Relaxation in GaAs(110) Quantum Wells,” Phys. Rev. Lett. **83**, 4196 (1999).

[60] V. Huard, R. T. Cox, K. Saminadayar, A. Arnoult, and S. Tatarenko, “Bound States in Optical Absorption of Semiconductor Quantum Wells Containing a Two-Dimensional Electron Gas,” Phys. Rev. Lett. **84**, 187 (2000).

[61] I. A. Merkulov, A. L. Efros, and M. Rosen, “Electron spin relaxation by nuclei in semiconductor quantum dots,” Phys. Rev. B **65**, 205309 (2002).

[62] K. V. Kavokin, “Anisotropic exchange interaction of localized conduction-band electrons in semiconductors,” Phys. Rev. B **64**, 075305 (2001).

[63] J. S. Sandhu, A. P. Heberle, J. J. Baumberg, and J. R. A. Cleaver, “Gateable Suppression of Spin Relaxation in Semiconductors,” Phys. Rev. Lett. **86**, 2150 (2001).

[64] M. I. D'yakonov and V. I. Perel', "Spin orientation of electrons associated with the interband absorption of light in semiconductors," Zh. Eksp. Teor. Fiz. **60**, 1954 (1971).

[65] Z. Chen, S. G. Carter, R. Bratschitsch, P. Dawson, and S. T. Cundiff, "Effects of disorder on electron spin dynamics in a semiconductor quantum well," Nature Physics (submitted).

[66] D. K. Maude, M. Potemski, J. C. Portal, M. Henini, L. Eaves, G. Hill, and M. A. Pate, "Spin Excitations of a Two-Dimensional Electron Gas in the Limit of Vanishing Landé g Factor," Phys. Rev. Lett. **77**, 4604 (1996).

[67] E. L. Ivchenko, A. A. Kiselev, and M. Willander, "Electronic g factor in biased quantum wells," Solid State Commun. **102**, 375 (1997).

[68] G. Salis, Y. Kato, K. Ensslin, D. C. Driscoll, A. C. Gossard, and D. D. Awschalom, "Electrical control of spin coherence in semiconductor nanostructures," Nature **414**, 619 (2001).

[69] M. J. Snelling, G. P. Flinn, A. S. Plaut, R. T. Harley, A. C. Tropper, R. Eccleston, and C. C. Phillips, "Magnetic g factor of electrons in GaAs/Al$_x$Ga$_{1-x}$As quantum wells," Phys. Rev. B **44**, 11345 (1991).

[70] D. Stein, K. v. Klitzing, and G. Weimann, "Electron Spin Resonance on GaAs-Al$_x$Ga$_{1-x}$As Heterostructures," Phys. Rev. Lett. **51**, 130 (1983).

[71] P. Dawson, I. Galbraith, A. I. Kucharska, and C. T. Foxon, "Low-power, all-optical nonlinear absorption in asymmetric double quantum wells," Appl. Phys. Lett. **58**, 2889 (1991).

[72] I. Galbraith, P. Dawson, and C. T. Foxon, "Optical nonlinearities in mixed type I˘type II GaAs/AlAs multiple quantum wells," Phys. Rev. B **45**, 13499 (1992).

[73] P. Dawson and M. J. Godfrey, "Recombination dynamics of spatially separated electron-hole plasmas in GaAs/AlAs mixed type-I/type-II quantum well structures," Phys. Rev. B **68**, 115326 (2003).

[74] C. Delalande, J. Orgonasi, J. A. Brum, G. Bastard, M. Voos, G. Weimann, and W. Schlapp, "Optical studies of GaAs quantum well based field-effect transistor," Appl. Phys. Lett. **51**, 1346 (1987).

[75] T. Yeo, B. D. McCombe, B. M. Ashkinadze, and L. Pfeiffer, "Metal-insulator transition of spatially separated electrons and holes in mixed type I-type II GaAs/AlAs quantum wells," Physica E **12**, 620 (2002).

[76] A. Malinowski and R. T. Harley, "Anisotropy of the electron g factor in lattice-matched and strained-layer III-V quantum wells," Phys. Rev. B **62**, 2051 (2000).

[77] S. G. Carter, Z. Chen, and S. T. Cundiff, “Optical Measurement and Control of Spin Diffusion in n-Doped GaAs Quantum Wells,” Phys. Rev. Lett. **97**, 136602 (2006).

[78] M. Dobers, K. v. Klitzing, and G. Weimann, “Electron-spin resonance in the two-dimensional electron gas of GaAs-Al$_x$Ga$_{1-x}$As heterostructures,” Phys. Rev. B **38**, 5453 (1988).

[79] A. Yariv, Optical Electronics in Modern Communications (Oxford, New York, 1997).

Appendix A

Birefringence of cryostat windows

The windows in our magneto-optical cryostat could carry strain-induced birefringence, which could be largely enhanced at low temperatures. In a transient Faraday/Kerr rotation measurement, a circularly polarized pump beam is needed to optically create spin polarized carriers in the samples, while a linearly polarized probe beam is required to measure the photo-induced Faraday/Kerr rotation. The birefringence in the cryostat windows, if any, will vary the polarization states of the otherwise circularly polarized pump and linearly polarized probe beams. This in turn affects both the degree of spin polarization in the samples after pump excitation [due to optical selection rules (Chapter 2)], and the detection sensitivity due to the ellipticity in the linear probe. It is therefore necessary to check any birefringence in the cryostat windows, and if any, compensate the birefringence.

A.1 Birefringence detected by Kerr rotation measurements

Circular polarization of the pump pulse is generated by inserting a quarter-wave plate in the pump beam path, with the azimuth angle of the quarter-wave plate at 45° with respect to the initial linear polarization of the laser output. If the pump polarization is not pure circular, there is a reduction of the observed Faraday/Kerr rotation amplitude as a result of optical selection rules. We measure the transient Kerr rotation in an undoped GaAs multiple quantum well sample

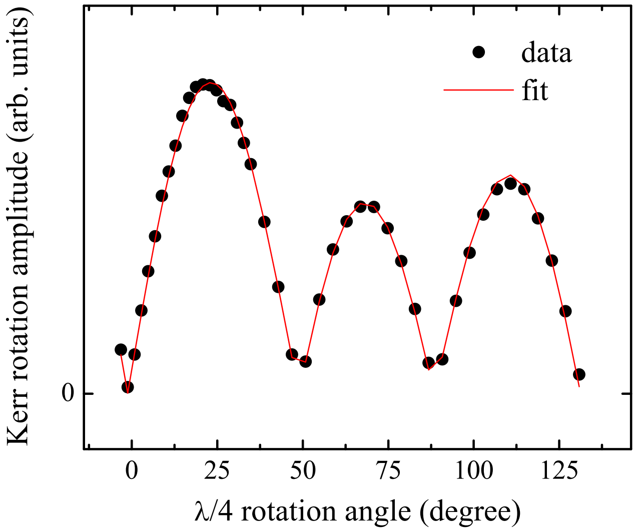

Figure A.1: Kerr rotation amplitude (absolute value) as a function of the azimuth angle of the quarter-wave plate ($\lambda/4$). Data are taken with an undoped GaAs multiple quantum well. Data are fitted with a Jones matrices calculation, which gives a window birefringence with a phase retardation of $\sim 90°$ (close to a quarter-wave plate).

(Section 3.2). To check the birefringence in the cryostat windows, we vary the polarization state of the pump pulse by rotating the azimuth angle of the quarter-wave plate in the pump beam path, and record the absolute value of the Kerr rotation amplitude. The Kerr rotation amplitude as a function of azimuth angle of the quarter-wave plate is plotted in Figure A.1. Without any birefringence in the cryostat windows, the Kerr rotation amplitude should have a 4-fold rotation symmetry, because the pump polarization varies from linear to circular to linear polarization as the quarter-wave plate is rotated from 0° to 45° to 90°. As shown in Figure A.1, the measured Kerr rotation amplitude does not show a 4-fold symmetry. This is due to the additional birefringence in the cryostat windows (front windows through which the pump beam passes before it hits the sample).

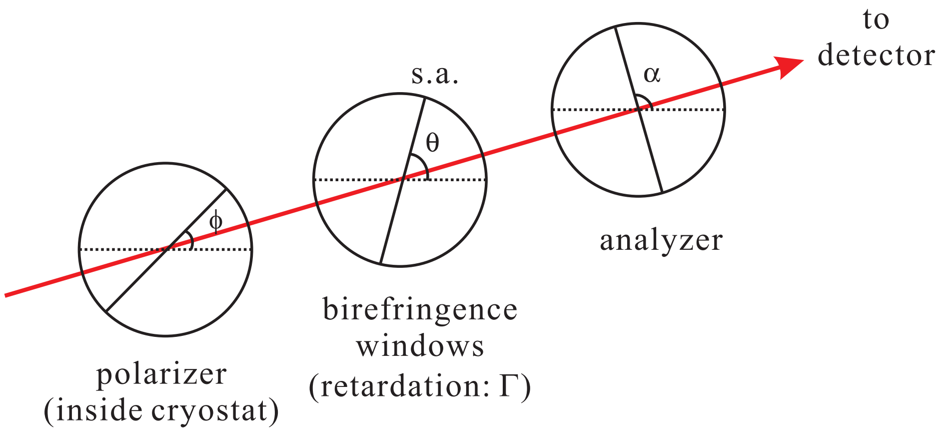

Figure A.2: Schematic setup for calibrating birefringence in the cryostat windows. The polarization state after the polarizer and birefringence windows is detected by measuring the output power as a function of the analyzer angle α. s.a., slow axis.

The dependence of Kerr rotation amplitude on the quarter-wave plate angle can be calculated by Jones matrices calculation [79], with the birefringence in the windows represented by an arbitrary phase retardation. We fit the data with Jones matrices calculation (discussed in detail below). This is shown as a solid line in Figure A.1, which corresponds to a phase retardation of $\sim 90°$ for the windows. The front cryostat windows work almost as a quarter-wave plate.

A.2 Calibration of birefringence

The birefringence in the cryostat windows is checked above through the measurements of Kerr rotation amplitude. This method is however not an ideal way for calibration of the window birefringence, because it requires accurate knowledge of optical selection rules in the sample used. A general method for birefringence calibration would be through the use of linear optical components such as polarizers and waveplates. Specifically, a polarizer (Newport Polarcor linear polarizer) is inserted into the sample chamber in the cryostat (where the samples normally sit). The laser beam after the polarizer is then directed through the back birefringence windows and another polarizer (analyzer). The polarization state after the birefringence windows can be detected by measuring the output power (through a photodiode) as a function of the analyzer rotation angle (Figure A.2).

In order to calibrate the window birefringence, we first go through Jones calculus for the system shown in Figure A.2. The Jones matrix for a polarizer at a rotation angle ϕ is

$$\mathbf{M_p} = \begin{pmatrix} \cos\phi & -\sin\phi \\ \sin\phi & \cos\phi \end{pmatrix} \begin{pmatrix} 1 & 0 \\ 0 & 0 \end{pmatrix} \begin{pmatrix} \cos\phi & \sin\phi \\ -\sin\phi & \cos\phi \end{pmatrix} = \begin{pmatrix} \cos^2\phi & \cos\phi\sin\phi \\ \cos\phi\sin\phi & \sin^2\phi \end{pmatrix}. \tag{A.1}$$

An initial arbitrary beam polarization is converted into a pure linear polarization after the polarizer, in the state of $\begin{pmatrix} \cos\phi \\ \sin\phi \end{pmatrix}$. Similarly the Jones matrix for the analyzer at an angle α is

$$\mathbf{M_a} = \begin{pmatrix} \cos^2\alpha & \cos\alpha\sin\alpha \\ \cos\alpha\sin\alpha & \sin^2\alpha \end{pmatrix}. \tag{A.2}$$

The window birefringence is represented by a Jones matrix for a birefringence medium with a phase retardation Γ and a slow axis at an angle θ,

$$\begin{aligned} \mathbf{M_w} &= \begin{pmatrix} \cos\theta & -\sin\theta \\ \sin\theta & \cos\theta \end{pmatrix} \begin{pmatrix} \mathrm{e}^{i\Gamma} & 0 \\ 0 & 1 \end{pmatrix} \begin{pmatrix} \cos\theta & \sin\theta \\ -\sin\theta & \cos\theta \end{pmatrix} \\ &= \begin{pmatrix} \mathrm{e}^{i\Gamma}\cos^2\theta + \sin^2\theta & (\mathrm{e}^{i\Gamma}-1)\cos\theta\sin\theta \\ (\mathrm{e}^{i\Gamma}-1)\cos\theta\sin\theta & \cos^2\theta + \mathrm{e}^{i\Gamma}\sin^2\theta \end{pmatrix}. \end{aligned} \tag{A.3}$$

The polarization state of the output field is then in the form of

$$\begin{pmatrix} E_x \\ E_y \end{pmatrix} = \mathbf{M_a}\mathbf{M_w} \begin{pmatrix} \cos\phi \\ \sin\phi \end{pmatrix}. \tag{A.4}$$

The output power at the detector can be expressed as

$$P \propto |E_x|^2 + |E_y|^2 = \frac{1}{2} + A\cos(2\alpha - 2\Psi), \tag{A.5}$$

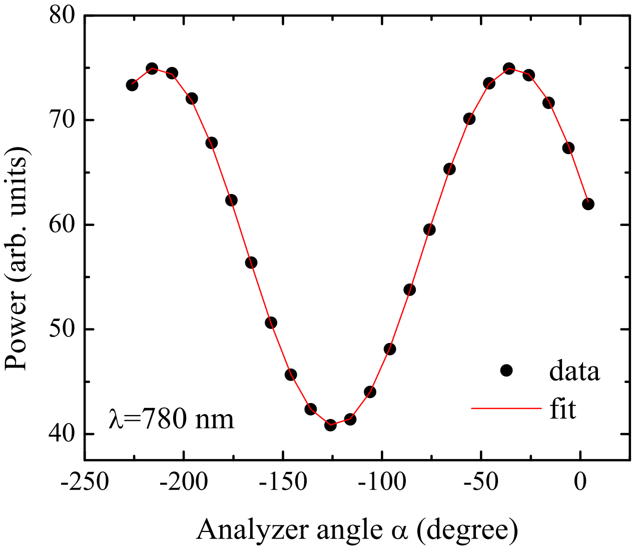

Figure A.3: Output power as a function of the analyzer rotation angle α for measuring front window birefringence. The data are fitted by using Equation A.5.

with

$$\begin{aligned} A\cos 2\Psi &= -\frac{1}{4}(\cos\Gamma - 1)\cos 4\theta + \frac{1}{4}(\cos\Gamma + 1), \\ A\sin 2\Psi &= -\frac{1}{4}(\cos\Gamma - 1)\sin 4\theta. \end{aligned} \tag{A.6}$$

For simplicity, α, θ and Ψ in Equation A.5 and A.6 are expressed with respect to ϕ (which is known experimentally), so that ϕ can be omitted in the equations.

Experimentally, we set the polarizer at $\phi = -36°$ from the horizontal direction. The output power is recorded as a function of the analyzer rotation angle α, for the back and front windows (by measuring in the reverse direction), and for several laser wavelengths. Figure A.3 shows the result for a measurement of the front window birefringence at a wavelength of $\lambda = 780$ nm. A nonlinear fit to the data using Equation A.5 gives $A = 0.148$ and $\Psi = -33.7°$ (solid line in Figure A.3). The parameters A and Ψ are then used to solve Equations A.6,

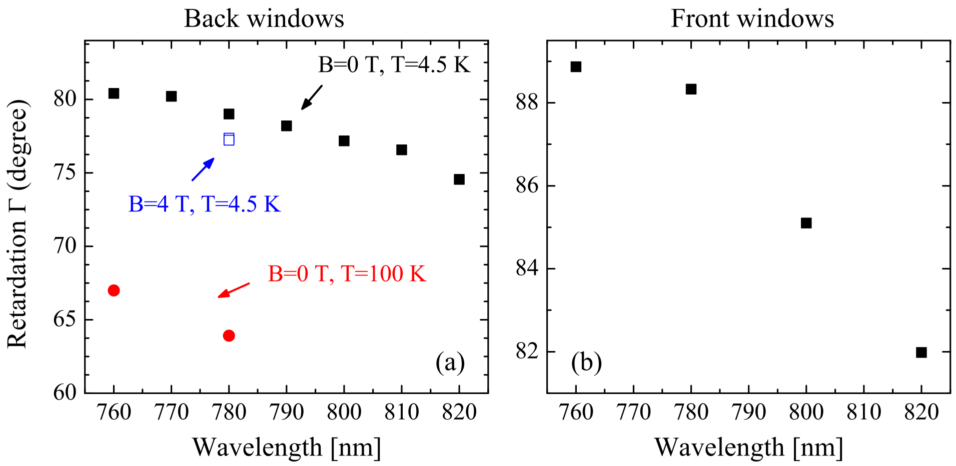

Figure A.4: Birefringence retardation as a function of wavelength for the (a) back and (b) front cryostat windows. Retardation for the back windows at a different temperature and magnetic field is also shown in (a).

which gives a phase retardation of $\Gamma = 88.3°$ and $\theta = 0.45°$ (from horizontal direction). The results indicate that at $\lambda = 780$ nm the front windows in the cryostat have a birefringence similar to a quarter-wave plate ($\Gamma = 90°$), and have the fast or slow axis almost in the horizontal direction. The above method does not distinguish the fast and slow birefringence axis, because both Γ and $-\Gamma$ are solutions to Equations A.6. To identify whether the fast or slow axis is associated with θ, an additional quarter-wave plate is inserted between the windows and the analyzer [if the fast axis of the quarter-wave plate is parallel to the fast (slow) axis of the windows, the polarization before the analyzer is almost linear, and is parallel (perpendicular) to the linear polarization immediately after the polarizer]. We find that it is the fast axis that is close to the horizontal direction.

The birefringence retardation for the back and front cryostat windows are shown in Figure A.4 for different wavelength. The fast axis is found to be at horizontal directions for all wavelengths. We also check the effect of temperature and magnetic field on the birefringence [shown in Figure A.4(a)]. The retardation reduces drastically at a higher temperature ($T = 100$ K) in the sample chamber. This confirms a strain-induced birefringence in the cryostat windows, which becomes significant at low temperatures. The magnetic field is shown to have little effect on the window birefringence.

A.3 Birefringence compensation

In order to get pure circular polarization for the pump beam and linear polarization for the probe beam (before they hit the samples), the birefringence in the cryostat windows needs to be compensated. By using a pair of half-wave plate and quarter-wave plate and adjusting their rotation angles, any polarization state can be generated. In the special case of a wavelength around $\lambda = 760 - 780$ nm, the front windows work roughly as a quarter-wave plate with its fast axis in the horizontal direction (as shown above). A circularly polarized pump beam can be easily generated by first rotating the linear polarization 45° away from the horizontal direction through a half-wave plate. The birefringence windows will then convert the linear polarization to an almost pure circular polarization. For birefringence other than $\Gamma = 90°$ (for example, at other wavelengths or for the back windows), a careful birefringence compensation using both the quarter- and half-wave plates is needed. The rotation angles for the waveplates can be decided through Jones matrix calculus, or by analysis using the Poincaré sphere, which provides a convenient way of predicting how a series of waveplates and retarders will change the polarization form. The probe beam will remain linear as long as its polarization axis is parallel to the fast or slow axis of the birefringence windows.